η Photoproduction off ^{3}He : Search for η mesic nuclei

Inauguraldissertation
Zur
Erlangung der Würde eines Doktors der Philosophie
vorgelegt der
Philosophisch-Naturwissenschaftlichen Fakultät
der Universität Basel

von
Francis Pheron
aus Guadeloupe, F.W.I.

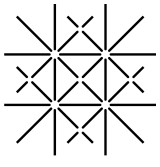

Basel
2012

Genehmigt von der Philosophisch-Naturwissenschaftlichen Fakultät auf Antrag von Prof. Dr. Bernd Krusche und Prof. Dr. Volker Metag.
Basel, den 16. November 2010

Prof. Dr. Martin Spiess, Dekan

Contents

Chapter 1

Introduction

1.1 Topic of this thesis

In 2008 the Physics and Astronomy classification schemes which are used since 1975 to identify fields and sub-fields of physics have introduced a new item: **Mesic nuclei, 21.85.+d.**. Mesic nuclei are a state of matter where a meson and a nucleus form a (quasi-)bound system for a certain time. If a meson, in particular an η-meson, binds to a nucleus, a new form of nuclear matter is created, the so called η mesic nuclei with an excitation energy of 550 MeV above the ground state.
The experimental confirmation of the existence of such states is very exciting on its own. But furthermore these systems would be ideal tools to study the not well-known η -nucleus interaction. Then one could even speculate for example whether the attractive potential is strong enough to form a bound η-mesic tri-neutron, although the tri-neutron itself is not bound.
Photoproduction of η-meson off ^{3}He was studied via the $\eta \rightarrow 2\gamma$ and $\eta \rightarrow 3\pi^0$ decay modes at the tagged photon beam of the Mainz MAMI accelerator using the combined 4π Crystal Ball/TAPS calorimeter. In a previous experiment, Pfeiffer et al. [30] had reported evidence (although at low statistical significance) for the formation of a quasi-bound η-nucleus state. The present experiment aimed at an improved statistical quality.

1.2 Structure of this thesis

This thesis is divided into 6 parts:

1. Chapter 1: This chapter starts with introductory remarks to the properties of nuclear matter followed by a discussion of the properties and systematics of pseudoscalars and vector mesons. Finally, it explains the reasons why ^{3}He was chosen as a promising candidate for η -mesic nuclei.
2. Chapter 2: This chapter will explicitly discuss η mesic nuclei. Introducing basic concepts like the scattering length approximation. It will also summarize the results of previous experiments.
3. Chapter 3: This chapter describes the different components of the experimental set-up of the present experiment.
4. Chapter 4: Discussion of the calibration procedure for the different subdetectors in view of particle energies, coincidence times , etc ...
5. Chapter 5: Summarize the identification of the different reaction channels
6. Chapter 6: Presentation of results and discussion

1.3 The origin of nuclear matter

The study of interactions between short-lived mesons and nucleons is the main topic of this thesis. First of all one has to discuss the environment where all these interaction will occur: the nuclear matter. Since all matter from its formation in the early universe to present day biological systems consists of atoms, understanding their structure and properties plays a vital role in physics, chemistry, and medicine. In fact, knowledge of atoms is essential to the modern scientific understanding of the complex systems that govern the physical and biological worlds. Atoms and the compounds they form play a part in almost all processes that occur on Earth and in space. All organisms rely on a set of chemical compounds and chemical reactions to digest food, transport energy, and reproduce. Stars such as the Sun rely on reactions of atomic nuclei to produce energy. Scientists duplicate these reactions in laboratories on Earth and study them to learn about processes that occur throughout the universe.

Throughout history, people have sought to explain the world in terms of its most basic parts. Ancient Greek philosophers conceived the idea of the atom, which they defined as the smallest possible piece of a substance. The word atom comes from the Greek word meaning not divisible. The ancient Greeks also believed this fundamental particle was indestructible. Scientists have since learned that atoms are not indivisible but made of smaller particles, and atoms of different elements contain different numbers of each type of these smaller particles.
These smaller particles are called electrons, protons, and neutrons. An atom consists of a cloud of electrons surrounding a small, dense nucleus of protons and neutrons. Protons and neutrons in the nuclei of atoms are held together by the strong force. This force must overcome the electromagnetic force of repulsion the protons in a nucleus exert on one another. The strong force that occurs between protons alone, however, is not enough to hold them together. Other particles that add to the strong force, but not to the electromagnetic force, must be present to make a nucleus stable. The particles that provide this additional force are neutrons. Neutrons add to the strong force of attraction but have no electric charge and so do not increase the electromagnetic repulsion.
To study in detail how the proton and the neutron are interacting with each other researcher have made particle accelerators. Theses devices increase the speed of a beam of particles such as protons and electrons. Scientists use the accelerated beam to study collisions between particles. The beam can collide with a target of stationary particles, or it can collide with another accelerated beam of particles moving in the opposite direction. If physicists use the nucleus of an atom as the target, the particles and radiation produced in the collision can help them learn about the nucleus. The use of particle accelerators opened the door for a new research field: subatomic physics.

1.4 The standard model

The theories and discoveries of thousands of physicists over the past century have resulted in a remarkable insight into the fundamental structure of matter: everything in the Universe is found to be made from twelve basic building blocks called fundamental particles, governed by four fundamental forces. Our best understanding of how these twelve particles and three of the forces are related to each other is integrated in the Standard Model of particles and forces. Developed in the early 1970s, it has successfully explained a host of experimental results and precisely predicted a wide variety of phenomena. Over time and through many

experiments by many physicists, the Standard Model has become established as a well-tested physics theory.

1.4.1 Elementary particles

Everything around us is made of matter particles. These occur in two basic types called quarks and leptons. Each group consists of six particles, which are ordered in pairs, or generations. The lightest and most stable particles make up the first generation, whereas the heavier and less stable particles belong to the second and third generations. All stable matter in the Universe is made from particles that belong to the first generation; any heavier particles quickly decay to the next most stable level.
The six quarks are paired in the three generations: the 'up quark' and the 'down quark' form the first generation, followed by the 'charm quark' and 'strange quark', then the 'top quark' and 'bottom quark'. The six leptons are similarly arranged in three generations: the 'electron' and the 'electron-neutrino', the 'muon' and the 'muon-neutrino', and the 'tau' and the 'tau-neutrino'. The electron, the muon and the tau all have an electric charge and a mass, whereas the neutrinos are electrically neutral with very little mass.

1.4.2 Forces and carrier particles

There are four fundamental forces at work in the Universe: the strong force, the weak force, the electromagnetic force, and the gravitational force. They work over different ranges and have different strengths. Gravity is the weakest but it has an infinite range. The electromagnetic force also has infinite range but it is many times stronger than gravity. The weak and strong forces are effective only over a very short range and dominate only at the level of subatomic particles. Despite its name, the weak force is much stronger than gravity but it is indeed the weakest of the other three. The strong force is, as the name says, the strongest among all the four fundamental interactions.

We know that three of the fundamental forces result from the exchange of force carrier particles, which belong to a broader group called 'bosons'. Matter particles transfer discrete amounts of energy by exchanging bosons with each other. Each

fundamental force has its own corresponding boson particles. The strong force is carried by 'gluons', the electromagnetic force is carried by the 'photon', and the 'W and Z boson' are responsible for the weak force. Although not yet found, the 'graviton' should be the corresponding force carrying particle of gravity.

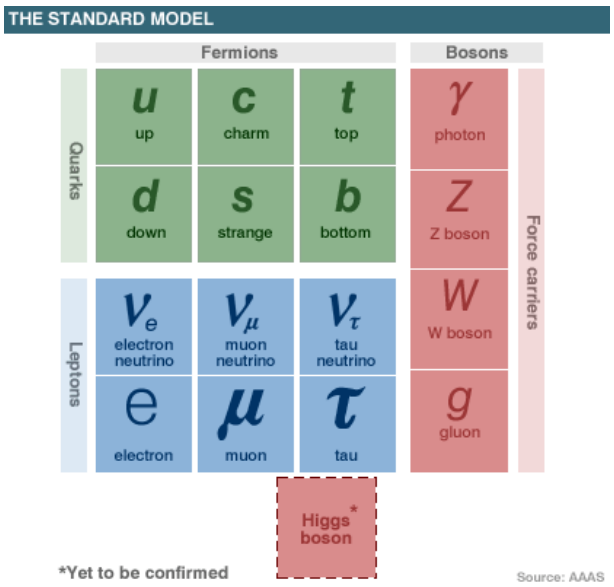

Figure 1.1: *The particles of the standard model*

The Standard Model includes the electromagnetic, strong and weak forces and all their carrier particles, and explains extremely well how these forces act on all the matter particles. However, the most familiar force in our everyday lives, gravity, is not part of the Standard Model. In fact, fitting gravity comfortably into the framework has proven to be a difficult challenge. The quantum theory used to describe the micro world, and the theory of general relativity used to describe the macro world, are like two children who refuse to play nicely together. No one has managed to make the two mathematically compatible in the context of the Standard Model. But luckily for particle physics, when it comes to the minuscule scale of particles, the effect of gravity is so weak as to be negligible. Only when we have matter in bulk, such as in ourselves or in planets, does the effect of gravity dominate. So the Standard Model still works well despite its reluctant exclusion of one of the fundamental forces. Fig 1.1 shows an overview of the standard model particles.

1.5 Origin of mesons

In the standard model, mesons are composed of quark and anti quark pairs. Before the discovery of quarks, the meson was considered as a strong interaction carrier. Theoretical work by Hideki Yukawa in 1935 had predicted the existence of mesons as the carrier particles of the strong nuclear force. From the range of the strong nuclear force (inferred from the radius of the atomic nucleus), Yukawa predicted the existence of a particle having a mass of about 100 MeV. Initially after its discovery in 1936, the muon (initially called the "mu meson") was thought to be this particle, since it has a mass of 106 MeV. However, later particle physics experiments showed that the muon did not participate in the strong nuclear interaction. The first “true” meson, the charged pion, was discovered by Cesar Lattes et al. [9] in 1947 at the university of Bristol. Since the advent of particle accelerators had not yet come, high-energy subatomic particles were only obtainable from atmospheric cosmic rays. Photographic emulsions, which used the gelatin-silver process, were placed for long periods of time in sites located at high altitude mountains, first at Pic du Midi de Bigorre in the Pyrenees, and later at Chacaltaya in the Andes Mountains, where they were impacted by cosmic rays. Since the neutral pion is not electrically charged, it is more difficult to detect and observe it than the charged pions. Neutral pions do not leave tracks in photographic emulsions, and neither do they in Wilson cloud chambers. The existence of the neutral pion was inferred from observing its decay products in cosmic rays, a so-called "soft component" of slow electrons with photons. The $\pi^0$was identified definitively at the University of California’s cyclotron in 1950 by observing its decay into two photons, and the same year, in cosmic-ray observing balloon experiments at the above-mentioned Bristol University. The fact that the $\pi^{\pm}$masses are identical comes from the CP symmetry role in the electroweak model. They belong to the special unitary group of degree 2 (SU(2)) but with the opposite z-component of isospin , +1 for π^+ and -1 for π^-. As noted in Table 1.1, the pion is spinless, and has a odd intrinsic parity ($J^p = 0^-$). Mesons of this type are named *pseudoscalar mesons.*

The earliest η and $\eta^{'}$ predictions were established by Sakata [33] where the nucleons and the Σ particle were used as the building block (so called Sakatons). In this theory, the neutral mesons with isospin 0 were needed to accompany pions and kaons which was the only pseudoscalars known at that time. In 1961, evidence for a three-pion resonance near 550 MeV was found by A. Pevsner et al. [29] in pion-nucleons collisions at the Bevatron. This was the experimental

Meson	Antiparticle	Quarks	Spin	Mass [MeV]	Lifetime [s]
π^0	Itself	$\frac{u\bar{u}-d\bar{d}}{\sqrt{2}}$	0	135	$0{,}83{\cdot}10^{-16}$
π^+	π^-	$u\bar{d}$	0	139.6	$2{,}60{\cdot}10^{-8}$
π^-	π^+	$\bar{u}d$	0	139.6	$2{,}60{\cdot}10^{-8}$

Table 1.1: *Properties of the π mesons*

$M_\eta = 547.51 \pm 0.18$ MeV	$M'_\eta = 957.8 \pm 0.14$ MeV
$\Gamma_\eta = 1.30 \pm 0.07$ keV	$\Gamma_\eta = 0.203 \pm 0.016$ keV
$\eta \to \gamma\gamma$ 39%	$\eta' \to \pi^+\pi^-\eta$ 44%
$\eta \to \pi^0\pi^0\pi^0$ 32%	$\eta' \to \rho\gamma$ 29%
$\eta \to \pi^+\pi^-\pi^0$ 23%	$\eta' \to \pi^0\pi^0\eta$ 21%
$\eta \to \pi^-\pi^-\gamma$ 5%	$\eta' \to \omega\gamma$ 3%
	$\eta' \to \gamma\gamma$ 2%

Table 1.2: *Properties of the η and η' mesons*

discovery of the η -meson. The $\eta^{'}$ was discovered independently by two groups in 1964, Kalbfleish et al [20] (paper submitted on 9th April) and Goldbergg et al. (paper submitted on 15th April) . The basic properties of η and $\eta^{'}$ mesons from the most recent issue from the PDG review are summarized in [31].

During this period no systematic representation of the mesons which would have allowed to classify them according to their properties and to predict further states was known. Such a scheme based on the SU(3) group was finally introduced in 1964 by Murray Gell-Mann and Richard Feynmann.

1.6 Meson and Baryon classification

This classification is based on group theory and classifies hadrons with identical parity and spin as a function of the third component of their isospin and strangeness.
The particles are classified in multiplets following the group theory:

- the baryons with $J^P = \frac{1}{2}^+$ in an octet (figure 1.3)
- the baryons with $J^P = \frac{3}{2}^+$ in a decuplet (figure 1.3)

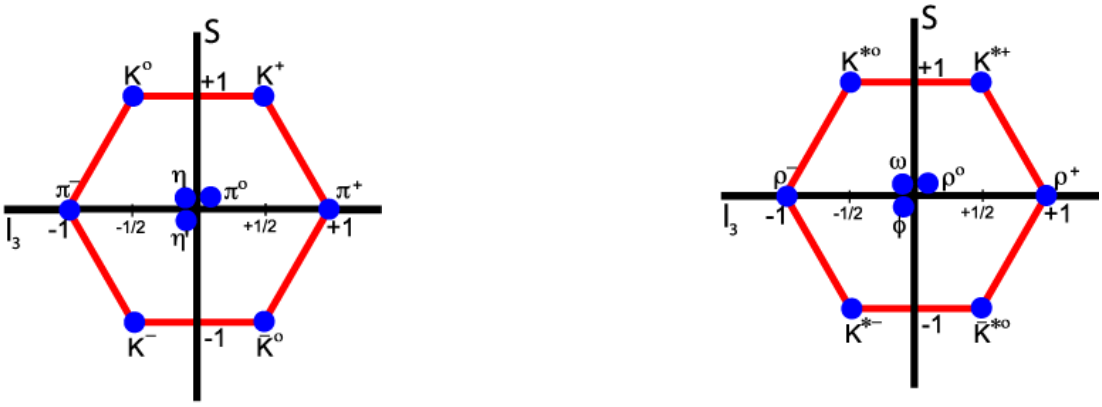

Figure 1.2: Left:*Pseudoscalars mesons octet + singulet* Right:*Vector mesons nonet*

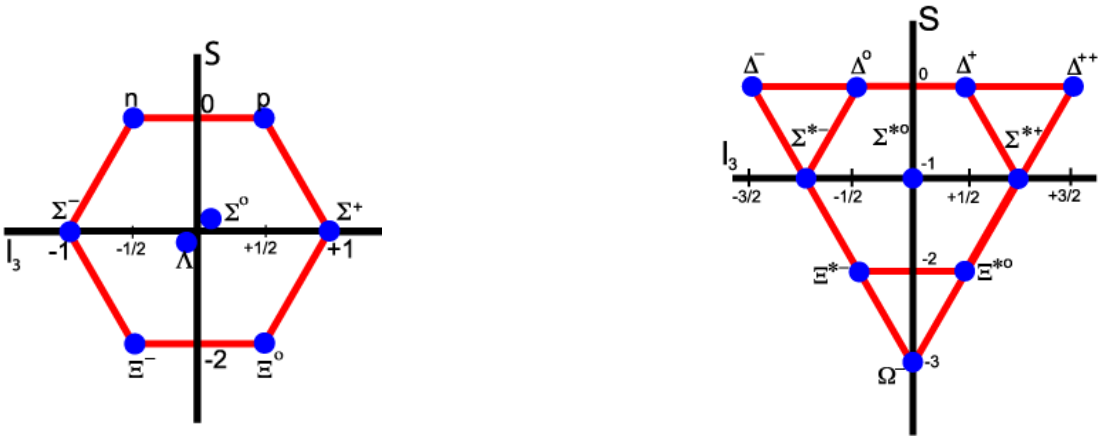

Figure 1.3: Left:*Baryons in an octet* Right:*Baryons in a decuplet*

- the pseudoscalar mesons ($J^P = 0^-$) and the vector mesons ($J^P = 1^{1^-}$) in nonets (figure 1.2))

The strength of this model is the prediction of new particles which have been detected many years after its construction. By itself, the hadron classification shows a certain logic which reveals an internal structure of the hadrons. This can be explained when hadrons are considered as particles composed of three quarks. The properties of these three light quarks up(u), strange(s) and down(d) are summarized in table 1.6. Mesons are made of a quark/antiquark pair and baryons of three quarks. With the rules of SU(3), a nonet scheme can be reproduced. All possible combinations of a quark and an antiquark are represented according to SU(3) ($3 \bigotimes 3 = 1 \bigoplus 8$). The η and η' mesons play a special role in this work. They are isoscalar members of the nonet of the lightest pseudoscalar mesons. In

	charge	mass [MeV]	Isospin I_3	strangeness
u	2/3 e	1-5	-1/2	0
d	-1/3 e	3-9	-1/2	0
c	2/3	1150-1350	0	0
s	-1/3 e	75-170	0	-1
t	2/3	174300	0	0
b	-1/3	4000-4400	0	0

Table 1.3: The properties of quarks up(u), strange(s) and down(d)

the SU(3) scheme there are two states with I = 0, S = 0:

$$\eta_1 = \frac{|u\bar{u} + d\bar{d} + s\bar{s} >}{\sqrt{6}} \tag{1.1}$$

and

$$\eta_8 = \frac{|u\bar{u} + d\bar{d} - 2s\bar{s} >}{\sqrt{3}} \tag{1.2}$$

Where η_8 is SU(2) (isospin) singlet but SU(3) octet and η_1 is SU(2) and SU(3) singlet. The quantum numbers of $|\eta_1\rangle$ and $|\eta_8\rangle$ are identical so that these two states can mix (this is described by a mixing angle) in order to make the physical observable states η and $\eta^{'}$:

$$|\eta\rangle = -\sin\theta|\eta_1\rangle + \cos\theta|\eta_8\rangle \tag{1.3}$$

$$|\eta^{'}\rangle = \cos\theta|\eta_1\rangle + \sin\theta|\eta_8\rangle \tag{1.4}$$

The topic of this thesis in the interaction of η -mesons with nucleons. As we will discuss below, this interaction is shaped by the existence of an excited state of the nucleon, the so-called $S_{11}(1535)$ resonance. Therefore in the next section we will introduce the systematics of nucleon resonances.

1.7 Nucleon resonances

In classical physics a resonance is the tendency of a system to oscillate at maximum amplitude for certain frequencies. Resonant phenomena occur for all types of vibrations: mechanical, electromagnetic, and quantum wave functions. In nuclear physics, these excitations can be studied in order to understand the complex internal structure of nucleons.

The excitation energy of nucleons is higher compared to the energy needed for the whole nucleus (keV range for the nucleus GeV range for the nucleons). Indeed, the physics of solids, molecules and atoms is governed by the electromagnetic interaction which is completely understood in principle, although the application to complicated many body systems yields a rich variety of fascinating phenomena. At deeper layers the strong interaction is mainly responsible for the structure of matter at two different levels: the formation of atomic nuclei from nucleons (protons and neutrons) and the formation of nucleons and other hadrons from the elementary quarks. At this scale the gauge field theory of the strong interaction is different from the electromagnetic interaction. Due to the small coupling constant α=1/137 of the electromagnetic interaction Quantum Electrodynamics (QED) allows the perturbative treatment of electromagnetic processes at low energies. With sufficient effort, quantities like for example binding energies of electrons in an atom, can be computed to any precision.
At higher energies one has to consider the quantum chromodynamics (QCD). This theory describes the strong interactions between quarks. In a similar way to the electromagnetic interaction, which is described by the exchange of photons between two charged particles, QCD describes the strong interaction with the exchange of particles called gluons between the quarks. In QCD however, the force between two quarks has different properties than the electromagnetic force, leading to a dramatically different behavior of the strong force. First, the force between two quarks doesn't diminish with distance as does the electromagnetic force. On the contrary, with an increase in the distance, the force tends to a constance value. In order to separate two quarks one needs an infinite energy. For this reason, the quarks will never be observed as free particles: this is called the confinement. At the other side, the force between two quarks diminishes with the distance, so that it is approximatively possible to treat the quarks inside the hadrons as free, non-interacting particles. This is called asymptotic freedom.
The study of nucleon resonances plays an important role for our understanding of the nucleon structure. Fig 1.4 shows that two types of nucleon resonances exist: the Δ resonances and the N^* resonances. Their properties are encoded in the following way in the notation scheme $X_{2I2J}(W)$: X specifies the relative orbital angular momentum for the decay to a nucleon-pseudoscalar meson final state. It is denoted with capital letters S,P,D,F,..... corresponding to L = 0,1,2,3,..... The two indices 2I and 2J specify the total isospin I and total spin J and W corresponds to the mass of the excited state. For example S_{11} resonances have L =0 , I =$\frac{1}{2}$, and J =$\frac{1}{2}$. When a nucleon is excited, this state (which can be N^* or Δ) decays dominantly by strong interaction (it can decay electromagnetically

via emission of photons). These decays are described by arrows in figure 1.4 and follow certain rules:

- They can decay directly back to the nucleon ground state by emission of a meson.
- They can decay sequentially via intermediate Δ or N* resonances to the ground state emitting multiple mesons.

In the total cross-section of photo absorption on nucleons, two regions are clearly visible:

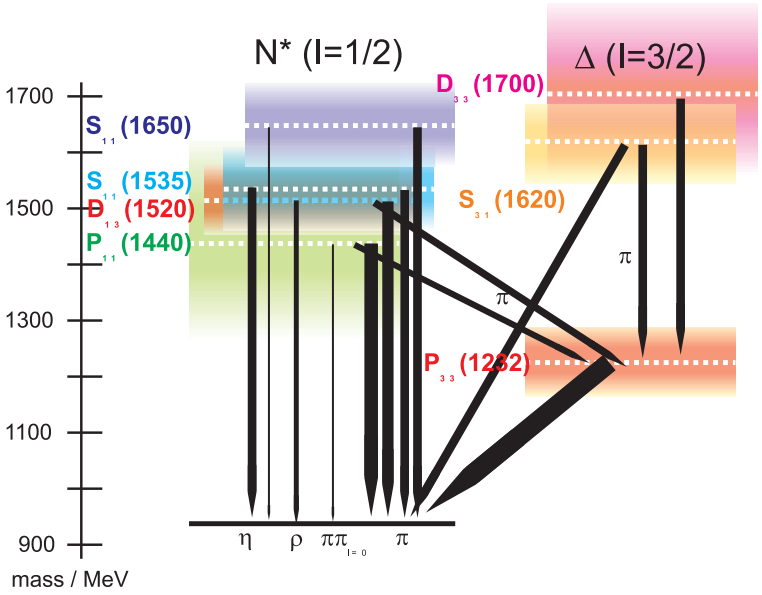

Figure 1.4: *Excitation spectrum of the nucleon and dominant decay modes of excited states, the widths of arrows corresponds to the strength of the transition*

- The $\Delta(1232)$ resonance is relatively light, 1232 MeV/c^2 and quickly decays via the strong force into a proton or a neutron and a pion. In the simple minded quark model this excitation corresponds to the spin-flip of one quark. Many properties of the Δ are well known, but nowadays lattice calculations can even calculate properties like the Δ magnetic moment and therefore more detailed experiments are done (refer to B.Boillat [5], S.Schumann [34] or E.Downie's theses [12] and S.Schumann et al. [35] article).

- Right above the $\Delta(1232)$ resonance, the second resonance region appears. In the second resonance region, all resonances (S_{11}, D_{13}, P_{11}) have a large branching ratio into N-π, but only the $S_{11}(1535)$ has a significant branching ratio (50%) into N-η . This behavior is not yet understood and gave rise to many discussion about the structure of this state. The basic configurations of these states in the framework of the simple constituent quark model are schematically depicted in figure 1.5 (the appropriate symmetries must be chosen for the flavor and color parts of the wave function).

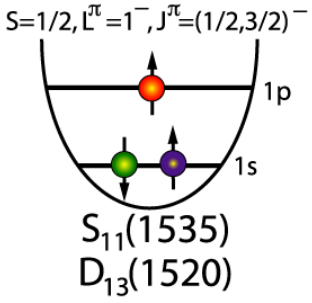

Figure 1.5: *The S_{11} has $L = 0$ for the decay into N_π, N_η total spin $J = \frac{1}{2}$ total isopin $I = \frac{1}{2}$, quark spins coupled to $S = \frac{1}{2}$, two quarks in 1s, one quark in 1p. Orbital angular momentum L=1 of quark in 1p coupled with total spin $S = \frac{1}{2}$ to total angular momentum $J = \frac{1}{2}$. Difference for D_{13}: Spin $\frac{1}{2}$ and L= 1 coupled to $J = \frac{3}{2}$*

The P_{11} ("Roper ") resonance has the same quantum numbers as the ground state nucleon and appears in all simple constituent quark models at much higher excitation energies than S_{11} and D_{13}. However, in experiment it lies even below those two states. It's structure is therefore much disputed.
Most nucleon resonances have been identified in pion scattering reactions which profit from the large hadronic cross sections. However, investigating nucleon resonances only in the π-channel has two obvious disadvantages: no use is made of the rich information connected to electromagnetic transition amplitudes and experimental bias may arise for nucleon resonances that couple only weakly to the Nπ-channel which might explain part of the so called 'missing resonance' problem. Moreover, from the experimental side, the main difference between nuclear and nucleon structure studies results from the large, overlapping widths of the nucleon resonances which makes it difficult to study individual resonances.

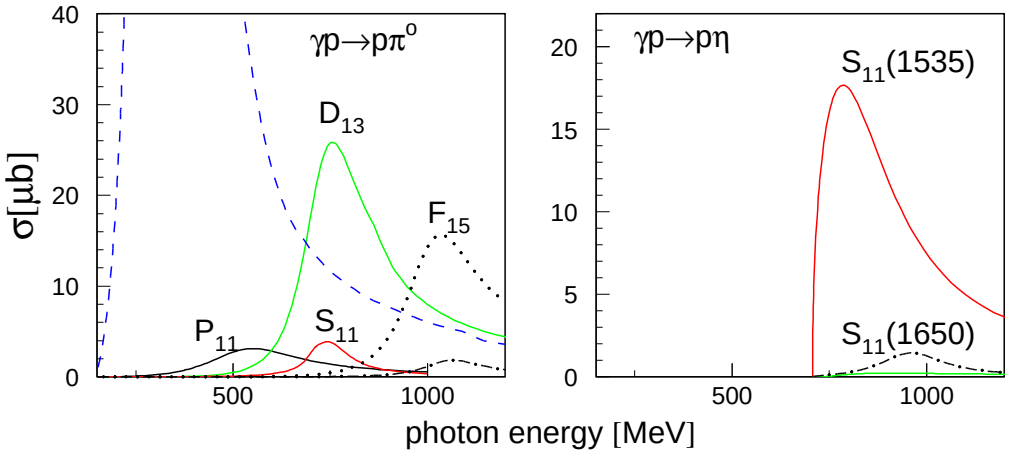

Figure 1.6: Contribution of resonances to π^o and η photoproduction (not quantitative). Full curves labeled P_{11}, D_{13} and S_{11} correspond to the $P_{11}(1440)$, the $D_{13}(1520)$, and the $S_{11}(1535)$ resonances. The dashed curve corresponds to the Δ, the dash-dotted curves to the $S_{11}(1650)$, and the dotted curve to the $F_{15}(1680)$.

As the isospin of the η is I =0, only the N* resonances with I = $\frac{1}{2}$ can contribute to the η photoproduction. Fig 1.6 shows the contribution of resonances to π^0 (left) and η (right) photoproduction. One can clearly see that η's tagg a smaller number of resonances. Therefore the η allows the study of resonances individually, for this reason the η is called *isospin filter*.

1.8 Formalism of Photoproduction

Fig 1.7 is a scheme for the process of η photoproduction via the electromagnetic excitation of an N* resonance:

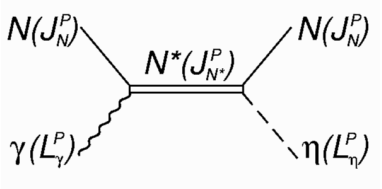

Figure 1.7: *η meson photoproduction via the excitation of N^* resonances.*

The information about the transition from the initial state γN to the final state

$\eta N^{'}$ is given by T, the transition matrix element with:

$$T_{fi} = \langle q m_{S'} | T | k m_S \lambda \rangle \tag{1.5}$$

If we consider all elements of T_{fi}, we have 8 components corresponding to:

- $\lambda = \pm 1$: two polarization states for the photon
- $m_S = \pm 1$: two spin states for the initial state nucleon
- $m_{S'} = \pm 1$: two spin states for the final state recoil nucleon

8 complex matrix elements, reduced by parity conservation to 4 independent complex matrix elements corresponding to 8 real numbers. Since the overall phase is not needed 7 independent real quantities are needed so 1.5 becomes:

$$T_{fi} = \sum_{j=1}^{4} \langle q m_{S'} | T | k m_S \lambda \rangle \tag{1.6}$$

A more explicit representation of the transition matrix T_{fi} can be given by using the Chew-Goldberger-Nambu-Low (CGNL) parameterization. If we consider $U_i(p_i)$ and $U_f(p_f)$ the Dirac spinors for initial and final nucleons, the solutions of the free Dirac equations:

$$(\gamma_\mu p^\mu - m_N) \cdots U(p^\mu) = 0 \tag{1.7}$$

are

$$U_i(p_i^\mu) = \sqrt{\frac{E_i + m_N}{2m_N}} \begin{pmatrix} \chi_i \\ \frac{\vec{p_i}\vec{\sigma}}{E_i + m_N} \quad \chi_i \end{pmatrix} \tag{1.8}$$

$$U_f(p_f^\mu) = \sqrt{\frac{E_f + m_N}{2m_N}} \begin{pmatrix} \chi_f \\ \frac{\vec{p_f}\vec{\sigma}}{E_f + m_N} \quad \chi_f \end{pmatrix} \tag{1.9}$$

With σ the Pauli matrices and χ_i, χ_f the spinors of the nucleons. So, for [7], T_{fi} is:

$$T_{fi} = \frac{4\pi W}{m_N} \langle \chi_f | F | \chi_i \rangle \tag{1.10}$$

Where W is the energy in the center of momentum. F is a 2x2 matrix , and $\hat{q} = \frac{\vec{q}}{q}$ and $\hat{k} = \frac{\vec{k}}{k}$ representing respectively the c.m momenta of the photon and η

mesons. So F becomes:

$$F = i\vec{\sigma}\cdot\vec{\varepsilon}F_1 + (\vec{q})\cdot\hat{q})(\vec{\sigma}\cdot(\vec{k}x\vec{\varepsilon})F_2 + iF_3\vec{\sigma}\cdot\hat{k}\hat{q}\cdot\vec{\varepsilon} + iF_4\cdot\hat{q}\hat{q}\cdot\vec{\varepsilon} \tag{1.11}$$

An expansion of the F_i into electric $E_l\pm$ and magnetic $M_{l\pm}$ multipoles corresponding to defined initial and final state momenta and parities can be constructed with Legendre polynomials $p_l(X)$, $X = \cos\theta$ (and their derivatives):

$$\begin{aligned}
F_1 &= \sum_{\ell=0}^{\infty}[\ell M_{\ell+} + E_{\ell+}]P'_{\ell+1}(x) + [(\ell+1)M_{\ell-} + E_{\ell-}]P'_{\ell+1}(x) \\
F_2 &= \sum_{\ell=0}^{\infty}[(\ell+1)M_{\ell+} + \ell M_{\ell-}\ell]P' \\
F_3 &= \sum_{\ell=0}^{\infty}[E_{\ell+} - M_{\ell+}]P''_{\ell+1}(x) + [E_{\ell-} - M_{\ell-}]P''_{\ell-1}(x) \\
F_4 &= \sum_{\ell=0}^{\infty}[M_{\ell+} - E_{\ell+} - E_{\ell-} - M_{\ell-}]P''_{\ell-1}(x)
\end{aligned} \tag{1.12}$$

Here, l is the orbital momentum of the outgoing meson and l_+/l_- indicate if the nucleon spin has to be added or subtracted to give the angular momentum of the intermediate resonance. With these CGNL amplitudes, the differential cross section of the reaction :

$$\gamma(k) + N(p_i) \rightarrow \eta(q) + N'(p_f) \tag{1.13}$$

can be written in term of amplitudes as follows [1]:

$$\begin{aligned}
\frac{k^*}{q^*}\frac{d\sigma}{d\omega} &= [\mid F_1 \mid^2 + \mid F_2 \mid^2 + \frac{1}{2} \mid F_3 \mid^2 + \frac{1}{2} \mid F_4 \mid^2 + Re(F_1F_3^*)] \\
&\quad + [Re(F_3F_4^*) - 2Re(F_1F_2^*)\cos\theta_{cm}] \\
&\quad - [\frac{1}{2} \mid F_3 \mid^2 + \frac{1}{2} \mid F_4 \mid^2 + Re(F_1F_4^*) + Re(F_2F_3^*)]\cos^2\theta_{cm} \\
&\quad - [Re(F_3F_4^*)]\cos^3\theta_{cm}
\end{aligned} \tag{1.14}$$

The table 1.8 shows the different solutions of states and quantum numbers for the η meson production.
In order to simplify equation 1.14, we can keep only the lowest order of multipoles

Final State	Initial State	Amplitude
η N	γN	J_γ=L_γ Magnetic J_γ=$L_\gamma \pm 1$ Electric
$J = L_\eta + \frac{1}{2}$	$J_\gamma = J - \frac{1}{2} = L_\eta$	Magnetic M_{L+}
$J = L_\eta + \frac{1}{2}$	$J_\gamma = J + \frac{1}{2} = L_\eta + 1$	Electric E_{L+}
$J = L_\eta - \frac{1}{2}$	$J_\gamma = J - \frac{1}{2} = L_\eta - 1$	Electric E_{L-}
$J = L_\eta - \frac{1}{2}$	$J_\gamma = J + \frac{1}{2} = L_\eta$	Magnetic M_{L-}

Table 1.4: *States and quantum numbers for the pseudo scalar mesons of photoproduction*

(l=0,1,2) and we have :

$$\frac{k^*}{q^*}\frac{d\sigma}{d\omega} = A + B\cos(\theta_{cm}) + C\cos^2(\theta_{cm})) \tag{1.15}$$

Where A,B,C are given in terms of the multipole amplitudes.

If we take the example of the $S_{11}(1535)$ resonance, we can deduce its electromagnetic multipoles with the table 1.4 or with the expression [1.14]. So we have in the η -p system the angular momentum J_γ given by:

$$J_\gamma = J + \tfrac{1}{2} \text{ (with } J = \tfrac{1}{2}) \text{ and } L_\gamma = L_\eta$$

The conservation laws for the angular momentum and the parity are fulfilled. So there is an electric multipole of the order L with

$$L = L_\eta = 0. \tag{1.16}$$

According to the formula [1.14], we calculate the F_i amplitudes, for S_{11} only the $\ell = 0$ terms contribute, so we have:

$$F_1(\theta^*) = E_{0^+}, F_2(\theta^*) = F_3(\theta^*) = F_4(\theta^*) = 0 \tag{1.17}$$

with: $P_0(\cos(\theta^*)) = 1$ and $P_1(\cos(\theta^*)) = \cos(\theta^*)$ and the differential cross section becomes:

$$\frac{k^*}{q^*}\frac{d\sigma}{d\omega} = \mid E_{0^+} \mid^2 \tag{1.18}$$

Experimental data show that only the coefficient A dominates in η photoproduction, in particular in the threshold region where B and C have negligible effects. This means that η photoproduction at low incident photon energies is dominated by the S_{11} resonance. However, a small contribution can come from interferences between the S_{11} and D_{13} resonances. The elementary process of meson production from the excitation of nucleons has been discussed, we will now discuss meson photoproduction from nuclei.

1.8.1 Mechanism for the photoproduction of mesons off nuclei

Three different mechanisms are existing to produce mesons from nuclei, they are discussed for the case of a ^{3}He nucleus but apply to any nucleus.

1. Quasi free/Break-up production $\gamma + N_{ucleus} \rightarrow \eta + N + (N_{ucleus} - 1)$:
   The meson is produced off one particular nucleon (the participant) which is removed from the nucleus. This means that the remaining nucleons do not participate in the reaction, they are spectators. This means that in general the final state is at least a three body-body final state consisting of:

   - the meson
   - the participating nucleon N (recoil nucleons)
   - The spectators nucleus A -1

   The energy threshold of quasi free production is for ^{3}He at $E_{qf} = E_{coh} + E_B$ = 600.6 MeV + 6.6 MeV = 607.2 MeV for the proton. Where E_{coh} is the η coherent energy threshold and E_B the binding energy. The case where the neutron (E_{th}= 609.9 MeV) is the participating nucleon gives an unstable remaining nucleus (2 proton system) and one will end up with even 4 particles in the final state.

2. Coherent production : $\gamma + N \rightarrow \eta + N$:
   For this reaction, the nucleus in the final state remains in its ground state and the amplitudes from all nucleons add up coherently. The center of momentum total energy $\sqrt{s}$ has to be high enough to produce at least the masses of the outgoing particles. The energy at threshold is:

$$\sqrt{s} = \sqrt{2 \cdot E_\gamma \cdot m_A + m_A^2} = m_\eta + m_A \tag{1.19}$$

And E_{coh} is given by :

$$E_{coh} = m_\eta + \frac{m_\eta^2}{2m_A} \tag{1.20}$$

The energy threshold for η photoproduction in the case of ^{3}He is E_{coh}= 600.6 MeV, which is less than for hydrogen (E_{coh}= 706.9 MeV). This difference comes from the fact that the recoil energy is bigger for a free proton, so less energy is available in the center of momentum compared to ^{3}He ($m_{^3He}$= 2808.9 MeV). If the energy of the impinging photon and the mesons polar angle are known, the energy of the produced meson can be calculated and compared to the measured value, this is the so called missing energy (discussed in part 6.3.3).

3. Incoherent production: $\gamma + N_{ucleus} \rightarrow \eta + N_{ucleus^*}$:
This process was observed for $\gamma + A \rightarrow A^* + \pi^0 \rightarrow A + \pi^0 + \gamma$. Incoherent production leaves the nucleus in an excited state and photons are emitted via the desexcitation process. However this is irrelevant for ^{3}He which does not have excited states

The coherent production is very interesting to investigate because close to threshold only a few number of resonances are contributing. Moreover, to search for η mesic nuclei, one needs a nucleus with non negligible coherent production cross section. The coherent cross section can be written as follows:

$$\frac{d\sigma}{d\Omega} \propto \boxed{\mid \Sigma A \mid^2} \times F^2(q^2) \times ..... \tag{1.21}$$

According to formula 1.21,the strength of the coherent cross section is depending on **the isospin amplitude, the spin structure and the form factor ($\mathbf{F(q^2)}$) of the nuclei, where q is the momentum transfer to the nucleus.**

Isospin amplitudes in η photoproduction

We know that at the hadronic vertex the isospin must be conserved. On the other hand, the electromagnetic vertex for the resonance excitation ($\gamma + N \rightarrow N^*$) does not necessarily conserve isospin. The electromagnetic current splits into an isovector component and an isoscalar component. The isospin amplitude A_j is

the sum of the isovector and the isoscalar amplitude respectively A_j^{IV} and A_j^{IS}. The η-photoproduction off the proton and off the neutron can be written as:

$$\begin{aligned} A_j(\gamma p \to \eta p) &= A_j^{IS} + A_j^{IV} \\ A_j(\gamma n \to \eta n) &= A_j^{IS} - A_j^{IV} \end{aligned} \tag{1.22}$$

In terms of cross sections we can add as well the deuteron nucleus :

$$\begin{aligned} \sigma(\gamma p \to \eta p) &\sim \mid A_j^{IS} + A_j^{IV} \mid^2 = \mid A^p_{\frac{1}{2}} \mid^2 \\ \sigma(\gamma n \to \eta n) &\sim \mid A_j^{IS} - A_j^{IV} \mid^2 = \mid A^n_{\frac{1}{2}} \mid^2 \\ \sigma_d &\sim \mid A_j^{IS} \mid^2 \end{aligned} \tag{1.23}$$

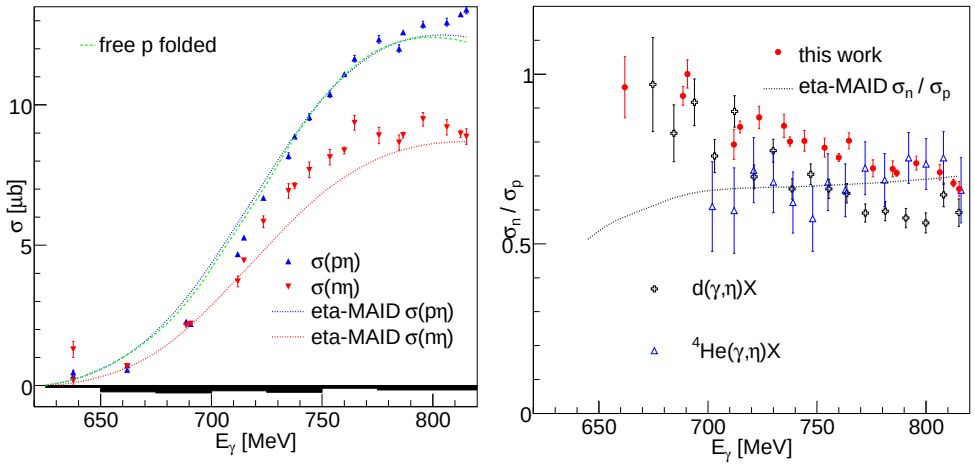

Figure 1.8: *Left: Quasi-free proton and neutron total cross section as function of the incident photon beam energy compared to the eta-MAID calculation folded*[2]*. Right: Neutron-proton cross section ratio as function of the incident photon beam energy compared to Eta-MAID calculation folded [18]*

Fig 1.8 show the quasi-free proton and neutron total cross section (left) and the neutron-proton cross section ratio (right). Weiss et al. [42] and later Jaegle et al. [18] showed that the ratio of the neutron-proton helicity amplitude for the $S_{11}(1535)$ resonance can be approximated at threshold as:

$$\mid A^n_{\frac{1}{2}}/A^p_{\frac{1}{2}} \mid = \sqrt{\sigma_n/\sigma_p} \tag{1.24}$$

$$\mid A^n_{\frac{1}{2}}/A^p_{\frac{1}{2}} \mid = 0.845 \pm 0.078 \tag{1.25}$$

The isoscalar/isovector part can be also extracted from:

$$\left(\frac{A_j^{IV}}{A_j^{IS}}\right)^{\pm 1} = \frac{1+\sqrt{\sigma_n/\sigma_p}}{1-\sqrt{\sigma_n/\sigma_p}} = 11.9 \pm 1.55 \tag{1.26}$$

Either the isoscalar or the isovector part of the S_{11} resonance is dominant. Only the study of coherent η photoproduction can clarify what is the dominant part. The η coherent cross section σ_d on the deuteron shows a very small value , thus, according to 1.23 the isovector part A_j^{IV} is dominant and $A^n_{\frac{1}{2}}$ and $A^p_{\frac{1}{2}}$ have opposite sign.
So, it is clear that the electromagnetic excitation amplitude of the $S_{11}(1535)$ resonance has a isospin structure which is dominantly isovector, this is the reason why coherent η photoproduction on the deuteron (which is an isoscalar nucleus) is weak. To produce coherently η -mesons via the $S_{11}(1535)$ resonance, one needs a nucleus with I $\neq$0.

Spin structure of the nuclei

The excitation of the S_{11} resonance proceeds via a spin-flip transition due to the E_{0+} multipole. For η photoproduction we have:

$$\gamma(E1) + N \rightarrow S_{11} \rightarrow \eta + N \tag{1.27}$$

$$J_z : -1 + \frac{1}{2} \rightarrow -\frac{1}{2} \rightarrow 0 - \frac{1}{2} \tag{1.28}$$

This means that one needs a nucleus capable to flip one spin during the excitation transition.

Form factor of the nuclei

According to 1.21, the strength of the coherent production is directly proportional to the form factor of the nuclei squared $F^2(q^2)$.

1.8.2 Target choice

The previous section showed that to have a strong coherent signal for η photoproduction the nuclei need to fulfill three conditions:

- The isospin should not be I = 0
- The spin should not be smaller than $\frac{1}{2}$
- The form factor should be as large as possible

For A < 4, three candidates are available for the coherent production :

- ^{2}H : J = 1, I = 0
- ^{3}He : J = $\frac{1}{2}$, I = $\frac{1}{2}$
- ^{4}H : J = 0, I = 0

^{3}He remains the best choice for a strong coherent signal because it allows the contribution of isovector, spin-flip amplitudes for the production of isoscalar mesons.

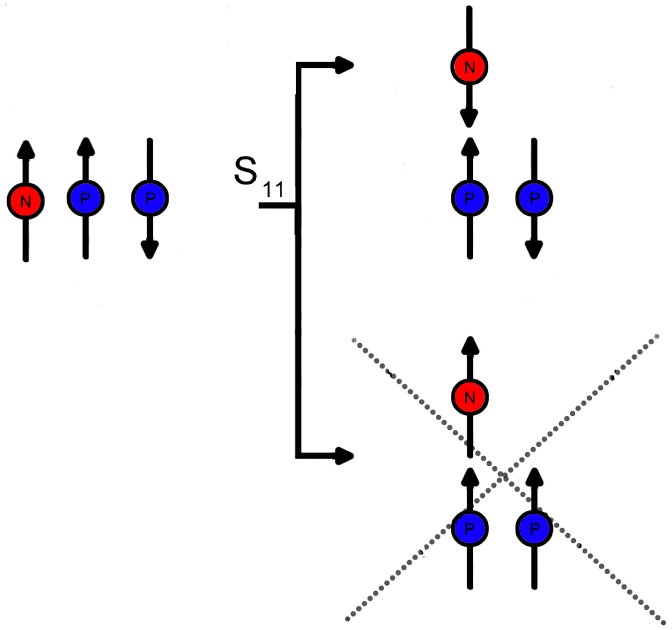

Figure 1.9: ^{3}*He spin structure. The contribution of the coherent production is only coming from the spin-flip of the neutron. A single proton spin flip would make the nucleus instable (the violation of Pauli's rules).*

Fig 1.9 shows the simplified spin structure of ^{3}He . The contribution for the coherent signal is coming from the spin-flip of the single neutron. The second

best candidate for a signal is ^{7}Li, however, due to it's small form factor compared to ^{3}He (fig 1.10) the η coherent photoproduction will be suppressed by approximatively one order of magnitude. Recent results for ^{7}Li are discussed in [26].

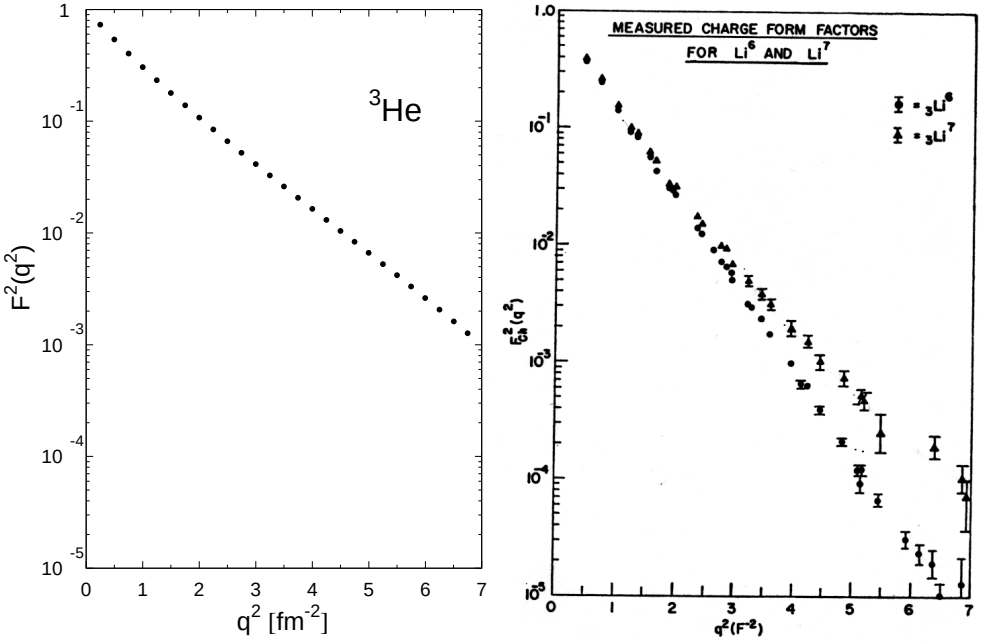

Figure 1.10: Form factors of ^{3}He [38] and ^{7}Li [39]

Chapter 2

η bound states

2.1 History of η mesic nuclei

In 1985 Bhalerao and Liu [6] were the first to model the interaction of η -mesons with A $\geq$ 12 nuclei . They used the pion-induced η production on a free nucleon to extract the η -nucleus scattering length. At this time few was known about η -production and η -nucleon interaction either experimentally or theoretically.
Before Bhalerao's and Liu's work, models for the $\pi N \rightarrow \eta N$ reaction were based either on the K-matrix approach or on a parameterization with Breit Wigner curves where the fit of experimental η production cross sections determined the masses and partial widths of resonances. However, this model didn't reproduce properly the interaction of (π, η) in nuclear matter.
Consequently, Bhalerao and Liu solved these issues by treating the η N channel in a coupled channel formalism. This method predicted an attractive S-wave η N interaction.
In 1986, Liu and Haider [25] were the first ones to suppose that the attraction between an η -meson and a nucleus is strong enough to make a bound system, what they called the η ***mesic nuclei***. According to them bound states can be formed only for nuclei of mass A $>$ 10. They studied how the signature for the existence of η mesic nuclei can be found. The models showed that η nucleus bound states can be formed in ^{15}O and heavier nuclei. The calculation also indicated that the case of ^{14}C is the border between the creation or not of a bound state. To validate this theory, experimental results were urgently needed.

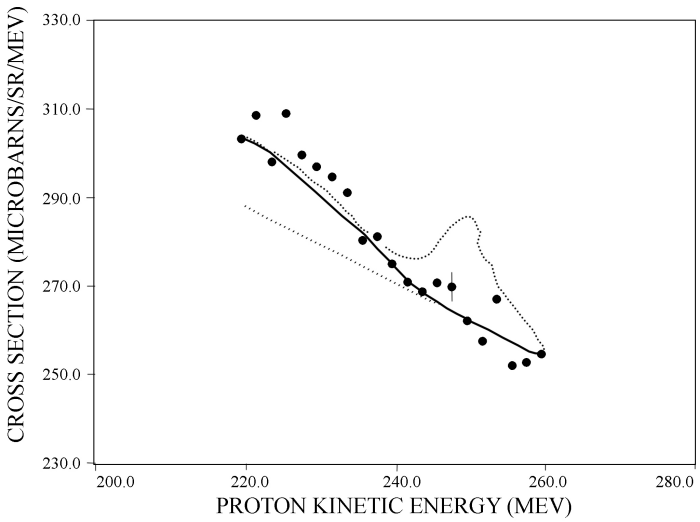

Figure 2.1: *The region of the oxygen spectrum in which the η bound state should appear [8].The experimental data points (black circles) are fitted by three curves: The long-dashed curve is the fit to the inclusive process (π^+, p), the solid curve shows an estimate of the quasifree η production added to the inclusive fit and the short-dashed curve shows the bound η state predicted by Liu and Haider.*

Chrien et al [8] performed in 1988 an experiment using different targets in a π^+ beam at 800 MeV/c. The reaction $\pi^+ + {}^{16}O \rightarrow p + {}^{15}_{\eta}O$ was supposed to be ideal for the observation of η bound states according to Liu et al [25], the one displaying the largest cross section. So, this experiment was designed to search for narrow states located near the onset of a quasifree process. The expanded region of the η cross section near the quasifree threshold is shown in fig 2.1 for the oxygen target. The experimental data points are fitted by three curves: The long-dashed curve is the fit to the inclusive process (π^+, p), the solid curve shows an estimate of the quasifree η production added to the inclusive fit and the short-dashed curve shows the bound η state predicted by Liu and Haider. The predicted peak is not seen experimentally.

In 1993 Johnson et al [19] tried to identify a bound state via a resonance like structure in the DCX [1] excitation function at fixed momentum transfer. They analyzed the channel: $\pi^+ + {}^{18}O \rightarrow \pi^- + {}^{18}Ne$. Figure 2.3 shows the missing energy histograms for ${}^{18}F$ for q = 0, 105, 210 MeV/c. Fig 2.2 shows the ratio of differential cross section for q = 0 to q = 210 MeV/c in the bound state region, where q is the momentum transfer of the reaction.This cross section ratio is used

[1] double charge exchange

to reduce the fluctuations. A cross check of this assumption is provided by the data in the energy region of ^{18}Ne where the η cannot be bound.
For these state there should be no structure. The solid circles in figure 2.2 show this ratio for a 23 MeV bin of the π^- missing energy (the cut can be seen in fig 2.3) above the ground state. A fit to the data with a straight line gives χ^2/N_{DF} = 1.45. This ratio is a constant function of beam energy. The ratio for the bound state is shown by solid squares in the same picture. The fit to the data with a straight line gives χ^2/N_{DF} = 3.44, indicating there may be structure in the η -meson threshold region. However, the statistical precision of the data was not sufficient to allow more than a qualitative characterization of this effect.

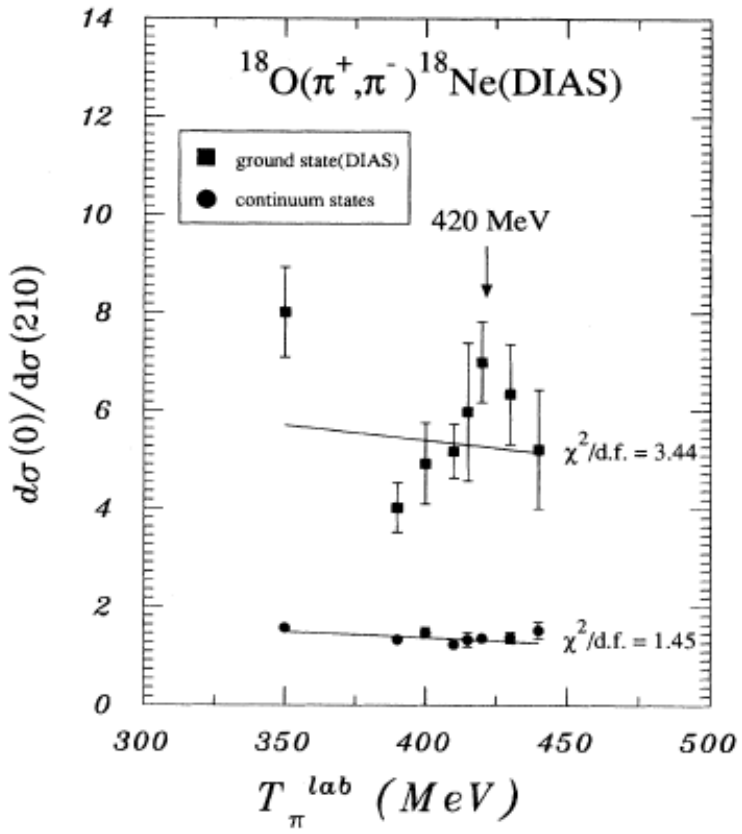

Figure 2.2: *Ratios of the q = 0 and q =210 MeV/c cross sections for bound (squares) and unbound region (circles) plotted with straight fits.*

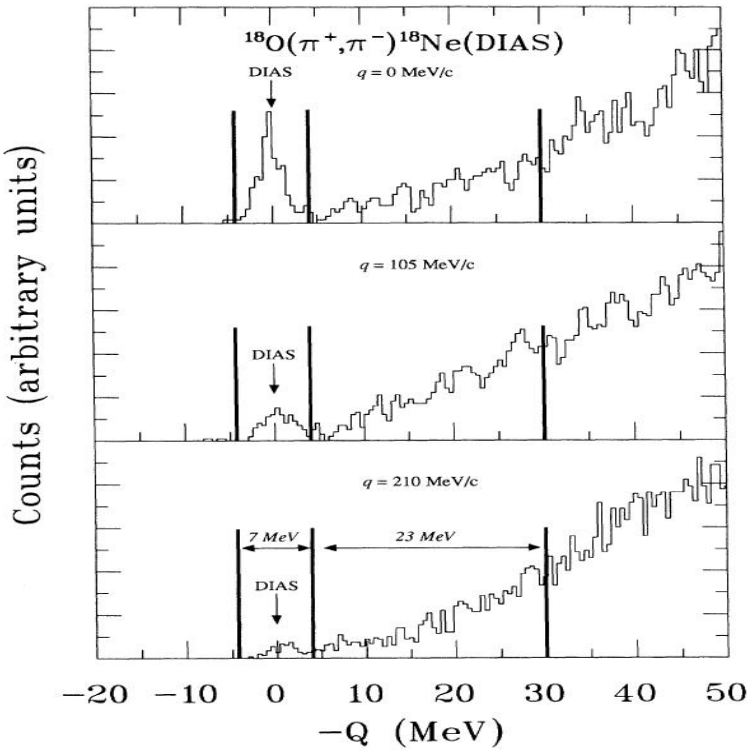

Figure 2.3: *Missing energy spectra in arbitrary units for the reaction* $\pi^+ + ^{18}O \rightarrow \pi^- + ^{18}Ne$. *A 7 MeV gate was set around Q =0 MeV/c. Another bin of 23 MeV was chosen outside the peak area.*

In 1991, the search for quasi-bound states with light nuclei was started when T.Ueda [41] predicted the existence of such a state for η NN with I = 0 and J = 1. According to Ueda, the bound state should be visible by a remarkable enhancement of the elastic cross section of η -d scattering near the η -d threshold.

Subsequently, the formation of light η -mesic nuclei including ^3H,^3He,^4He was discussed in the framework of different models ([32], [37]). Experimental search for such states was for example done via the study of the threshold behavior of η -production reactions in hadron and photon induced reactions.

2.2 Models for $\gamma^3He \rightarrow \eta^3He$

First we introduce the scattering length a which depends on the nature of the nuclear potential, and, therefore, the prediction of this value is an important test

for models of the nuclear potential.
a is a complex number :

- The imaginary part represents the loss of the initial current of particles after the interaction
- The real part signals if the potential is attractive or not. A large positive real part signals the presence of a bound state and negative means that there is no bound state.

The scattering length described above is an important parameter in theoretician's calculations to predict cross sections including or not the η bound state. In this part, the work of three theorist will be summarized: N. Shevchenko, S. Kamalov, A. Fix. Their work focused on the η coherent production in the threshold region.

Coherent photoproduction of η mesons on three nucleon systems:

A microscopic few-body description of near-threshold coherent photoproduction of the η meson off ^{3}He is given by N. Shevchenko [36]. The photoproduction cross section is calculated using the Finite Rank Approximation. This FRA approach means that the ^{3}He nucleus in the η -^{3}He elastic scattering remains in the intermediate state in its ground state. This approximation is used to calculate the T-matrix. The transition matrix describes the probabilities of moving from one state to another in a dynamic system.
The problem of constructing the T-matrix $t^{\eta\eta}$ corresponding to an η -N potential has no unique solution since the only experimental information consists of the S_{11} resonance pole position and the η -N scattering length $a_{\eta N}$. The work of Shevchenko et al [36] uses two different versions of $t^{\eta\eta}$.

- *Version I* : Without any scattering data it is practically impossible to construct a reliable η N potential. In the low-energy region the elastic scattering can be viewed as the process of formation and subsequent decay of the S_{11} resonance, i.e. :

$$\eta + N \rightarrow S_{11} \rightarrow \eta + N \tag{2.1}$$

  The intermediate state to the process 2.1, is assumed to have a simple Breit-Wigner form. The Breit-Wigner equation is depending on a strength parameter λ. This parameter is chosen to reproduce the η -nucleon scattering length $a_{\eta N}$. In most recent publications the value used for $\mathrm{Im}(a_{\eta N})$

is around 0.3 fm. However, for Re$a_{\eta N}$ the estimates are still very different. Shevchenko assumed that :

$$a_{\eta N} = (0.75 + \imath 0.27) fm \tag{2.2}$$

The T-matrix $t^{\eta\eta}$ constructed in this way reproduces the scattering length and the S_{11} pole.

- *Version II*: An alternative way of constructing the two-body T-matrix $t^{\eta\eta}$ is to solve the corresponding scattering equation with an appropriate separable potential having the same form factor. This version of $t^{\eta\eta}$ also reproduces the scattering length and the S_{11} pole. Moreover, it is consistent with the condition of two-body unitary.

Fig 2.4 shows the results of the calculation for the total cross section of the coherent process. The calculations were done for ^{3}He nuclear targets using the two versions of $t^{\eta\eta}$ described above. The curves corresponding to these two matrices are denoted by (I) and (II) respectively. They found that the coherent η -photoproduction is strongly enhanced in the near threshold region compared to higher photon energies ($E_\gamma > 610$ MeV). This can be attributed to strong final state interaction caused, for example, by a pole of the scattering S-matrix, situated in the complex-energy plane not far from the threshold energy, in other words to formation of an η -nucleus resonance.

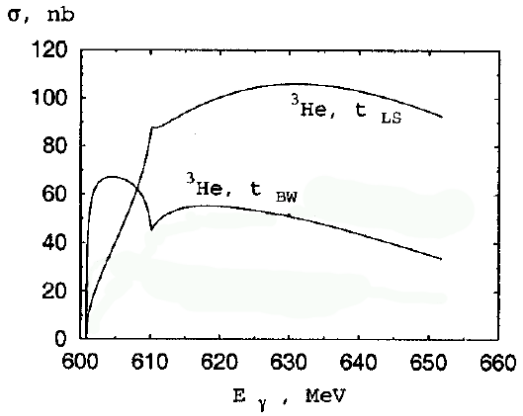

Figure 2.4: *Coherent photoproduction cross section with different elementary $t^{\eta\eta}$ matrices.*

Pion interaction with the trinucleon up to the eta production threshold:

The model proposed by S.Kamalov et al [21] is not based on the scattering process contrary to Shevchenko's. Indeed, this work is based on an optical model modified by the implementation of the Fermi motion, the Pauli blocking effect, real pion absorption etc ..., In the framework of this model, Kamalov has calculated the pion-induced η cross section. This cross section underestimates the experimental data in the threshold region but they found a better agreement at higher momentum transfer. Basically, this model doesn't introduce any scattering length.

Final state interaction effects in η photoproduction on three body nuclei

A prediction made by A.Fix and H.Arenhoevel [13] introduced a different approach. Fix et al supposed that the s-wave of the final η-3N system is treated in the frame of the three-body scattering theory ((η N) + (NN), η + 3N and N + (η NN)). They obtained values for the η -^{3}He scattering length that do not allow the existence of a bound state of η meson and nucleus ($a_{\eta N} = 0.5 + \imath 0.27$). However, the attraction in the η -3N system remains and influences the dynamical properties. According to the authors, a strong threshold cusp effect induces the creation of a virtual pole near threshold.

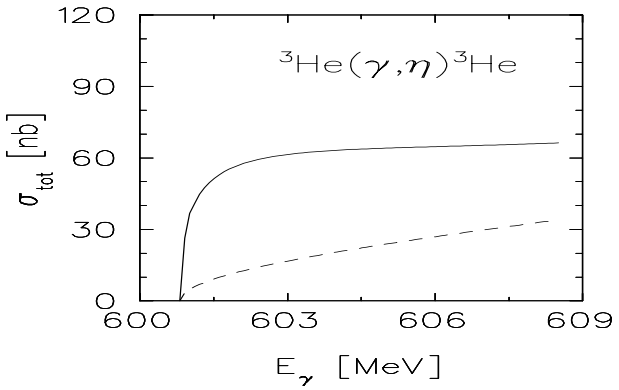

Figure 2.5: *Total cross section for the photoproduction of η on ^{3}He . Solid (dashed) curve presents the result with (without) FSI.*

This feature is demonstrated in fig 2.5, where one can see a very rapid rise of the

total cross section ^{3}He (γ, η)^{3}He, in contrast to a much flatter form predicted by the plane wave approximation (dashed line). Their analysis obtains values for the η -^{3}He scattering length that do not allow a bound state of η meson and nucleus.
In this model, all contributions from other intermediate hadronic channels are neglected, which means that the process where the photons induce first a pion which then rescatters into the η on another nucleon is not induced.

2.3 Search for η -mesic nuclei: positive results from experiment

2.3.1 Experiment for carbon

The first signal for an η -meson bound state was claimed for a photon induced reaction of the following type:

$$\gamma +^{12} C \rightarrow p(n) +^{11}_{\eta} B(^{11}_{\eta}C) \rightarrow p(n) + \pi^+ + n + X \tag{2.3}$$

This experiment was performed at the 1 GeV electron synchrotron of the Lebedev Institute. For the quasifree η production on ^{12}C the recoil nucleon is ejected. This kinematic means that the η is slow and forms a $^{11}_{\eta}B$ or $^{11}_{\eta}C$ and then the η is recaptured into a S_{11} resonance and then a $\pi^+ - N$ back-to-back pair is ejected (see fig 2.6).

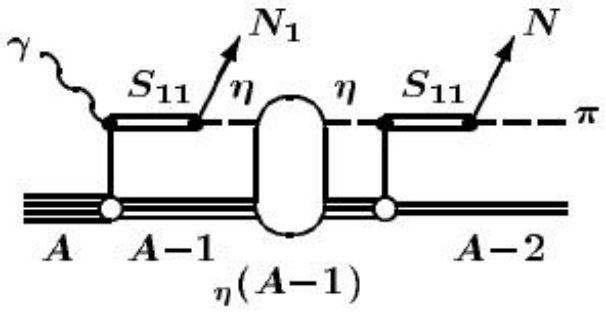

Figure 2.6: *Schematic process for the production of an η -mesic state via photoproduction off ^{12}C*

In the subthreshold region of the invariant mass $\sqrt{s_{\pi^+ n}} < m_\eta + m_N$, an intermediate η mesic nucleus is produced. A peak is expected in the invariant mass

distribution in the threshold region. Fig 2.7 shows clearly a peak when the photon beam energy exceeds the η production threshold off the free nucleon (707 MeV). The peak is not observed when the energy is below the threshold [4]. This picture was obtained by applying an unfolding procedure to raw experimental velocity-distributions found by the time of flight technique.

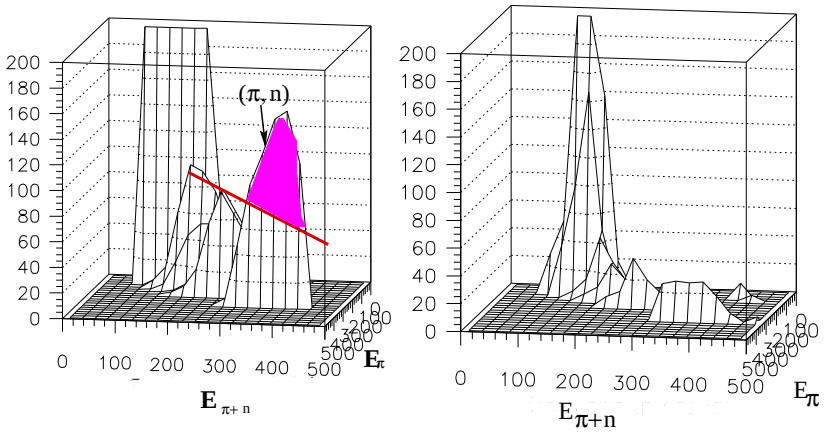

$E_{\gamma\max} = 850$ MeV $\qquad$ $E_{\gamma\max} = 650$ MeV

Figure 2.7: *2-D distributions over the kinetic energy of $\pi^+ n$ pair for two energies of the photon beam, $E_{\pi^+ n}$, and the kinetic energy of the π^+, E_π for two energies $E_{\gamma\max}$ of the bremsstrahlung photon beam.*

2.3.2 $dp \rightarrow {}^3$He η reaction near threshold

At the COSY reactor of the Forschungszentrum Julich data was taken for the $dp \rightarrow {}^3$He η reaction near threshold. In principle, the experiment measured the energy dependence of the total cross section. The measurement at lower excess energy Q, which is the amount of energy above the threshold, is investigated. Fig 2.8 shows an unexpected behavior of the cross section. Indeed, one can observe a rapid rise at threshold leading to the assumption that there is a virtual or nearby bound state of the η ^{3}He nucleus [37, 43].

In the plane of the complex momentum Q with $\mathrm{Im(Q)} < 0$, the bound state leads to a pole of the η ^{3}He $\rightarrow$ η ^{3}He scattering amplitude. If the η -nucleus force is not attractive enough, the signs of these imaginary parts are reversed and the state is called virtual.

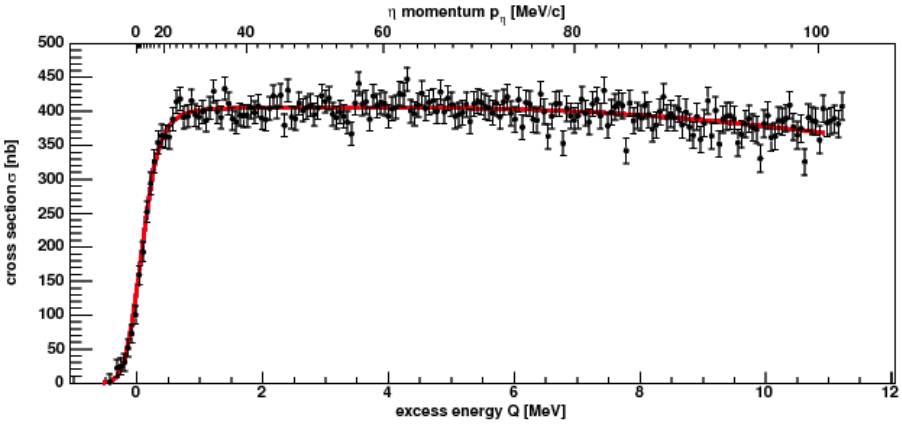

Figure 2.8: *Cross section of dp →^{3}He η measured at COSY-ANKE [28]*

When a pole is close to Q = 0 it distorts strongly the energy dependence of the *dp* →^{3}He η total cross section at low energies (C. Wilkin [44]). This distortion is exactly what is observed.

2.4 η photoproduction in the threshold region

This part is about the η photoproduction in the threshold region, in particular, what kind of signals could be related to η -mesic states. The mechanisms sketched in fig 2.9 are considered.

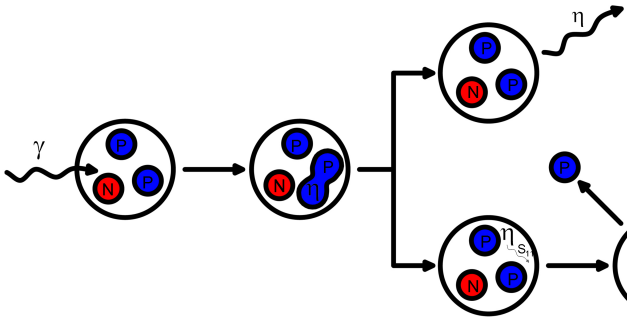

Figure 2.9: *The η is produced coherently and can be either ejected from the nucleus or reabsorbed by another nucleon.*

If a truly bound state is formed, the η cannot be emitted (it is bound). However, this state may be broad enough that it overlaps the threshold and the part above

threshold can contribute to coherent η -production. Then there are two possible decay modes for an η mesic state:

- **coherent η production**, the η comes out of the nucleus with or without absorption of the η into the S_{11}. Here only the part of the η mesic resonance above η threshold contributes.

- The S_{11} resonance can decay by emitting a π^0 meson. In this case as the η is produced in an intermediate step, this process is also possible for photon energies below the η threshold. In the final state, one has to detect a π^0 meson and a proton to identify the η bound state. However, the emission of π^0-proton pairs is strongly dominated by quasi free π^0 production off protons which causes a large background.
  To discriminate the interesting π^0-proton pairs coming from the decay of an S_{11} resonance from quasi free production, one has to use the kinematic difference between the two mechanisms. In η mesic production, the bound η has a small momentum. At higher momenta the η would leave the nucleus. This means that the S_{11} resonance is almost at rest in case of η mesic production. In the γ-^{3}He frame, the S_{11}-decay into a π^0-proton pair results in a relative angle close to 180° between π^0 and proton. The search for η mesic nuclei will use the detection of π^0-proton pairs emitted in back-to-back kinematics in the center of momentum frame of the photon and the ^{3}He nucleus at photons energies close to the η -production threshold.

2.4.1 η photoproduction off ^{3}He

The first experiment based on the signature discussed above was performed at the Mainz Microtron facility. The results for coherent η production off ^{3}He and the π^0pX decay channel were investigated for possible signs for the formation of an η -mesic state. In the η channel a resonance like behavior and a isotropic angular distribution in the threshold region was observed.

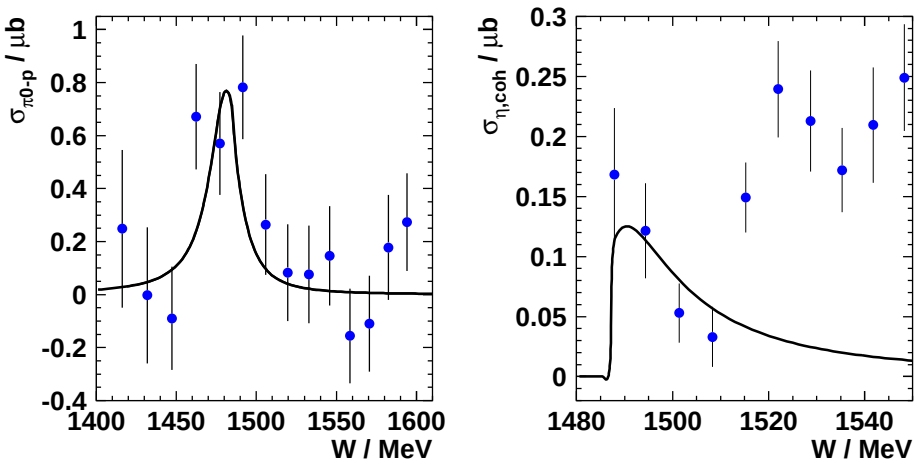

Figure 2.10: *Left: Excitation function of π^0-proton back-to-back emission after background subtraction. Solid line is a Breit-Wigner distribution fitted to the data. Right: Coherent η cross section, the solid line is the expected cross section for the decay of a possible η mesic nucleus into $\pi^0 pX$. .*

Moreover, π^0-proton back-to-back emission in the cm system was also detected around the coherent threshold region. 2.10 shows the results of Pfeiffer et al. Both studied channels seemed to indicate a possible signal but the statistical quality was low. For this reason, a new experiment has been performed, the next chapter deals with the experimental setup.

Chapter 3

Experimental Set-up

The purpose of the present experiment is to measure the angular distributions and the total cross section of the reaction $\gamma^3He \to \eta^3He$ with much better statistical quality than the previous experiment. This requires a more efficient experimental setup capable of collecting much more events from the reaction of interest in a given time. This may be achieved by the following improvements:

- A complete coverage of the solid angle to study the angular dependence of the reaction, reduce background contributions by a complete definition of the detected events, and enhance counting statistics via the large acceptance.
- a high performance electronics and data acquisition system allowing high data rates at small dead time to achieve high counting statistics.

3.1 The MAinz MIcrotron: MAMI

The experiment was performed at the Mainz MAMI accelerator which is a staged race-track microtron. At the end of the 70s, the first beam of 14 MeV was produced at the Mainz Microtron, then in the 80s a second stage provided a beam of 180 MeV: MAMI A. The third stage, MAMI B delivered an electron beam up to 882 MeV in the 90s. The last upgrade of this facility, MAMI C, can reach the energy of 1558 MeV. The MAMI current can provide the intensity of ~ 80 μA, this is used for e^--scattering. For tagged photons one cannot use more than 100

nA (most of the time even not more than $\sim$ 20 nA). Fig 3.1 illustrates schematically the facility:

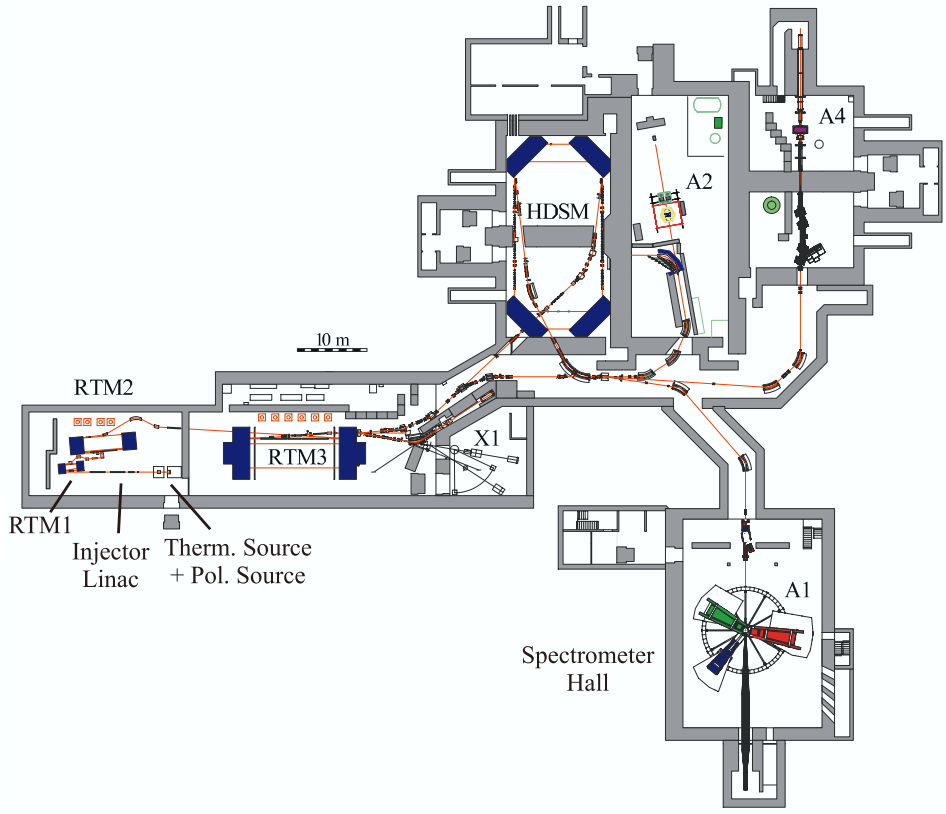

Figure 3.1: *MAMI, particle accelerator*

The electron beam can be delivered to three different experiment halls:

- A1 is equipped with large magnetic spectrometers for e^--scattering experiments
- A2 is the hall with the tagging spectrometer for quasi-monochromatic photon beams where this experiment was performed.

The electron accelerator MAMI consists of three cascaded racetrack Microtrons with a 3.5 MeV injector linac. The pre-accelerated electrons from the 3.5 MeV injection LINAC are sent to the first Race Track Microtron (RTM). The RTM consists of two powerful dipole magnets face-to-face. At each accelerating step, electrons gain in energy and the curvature of their path increases as well. The

General	
Input Energy	855.1 MeV
Output Energy	1508 MeV
Magnet System	
flux density[T]	1.53-095
Number of quadrupole and correctors	8-356
Weight par magnet[t]	250
Maximum intensity	100 μA

Table 3.1: *Basic features of the MAMI accelerator*

beam pipes are needed because the electron beam has to run in vacuum (see 3.2).

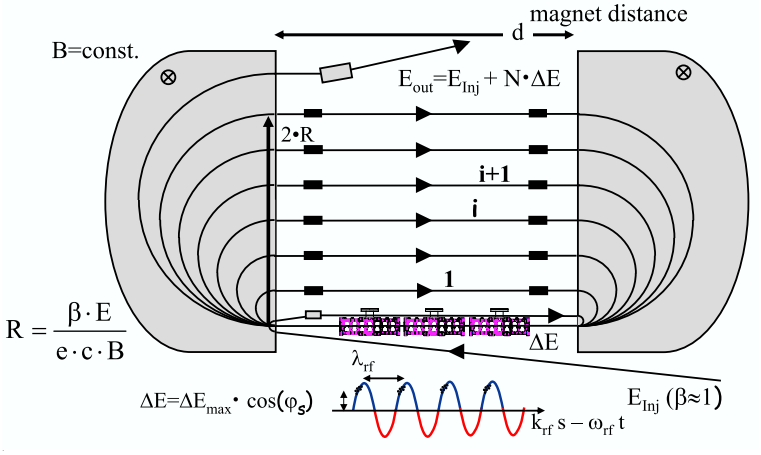

Figure 3.2: Race Track Microtron

The third stage (RTM3) delivers beams from 180 MeV to 855 MeV in 15 MeV steps. The Harmonic Double Sided Microtron (HDSM) is the last upgrade of MAMI, with an energy increase from 855 MeV to 1508 MeV. This accelerator is known for the high intensity (100μA), the stability and the quality of its beam. Table 3.1 summarizes all main parameters of the present MAMI-C.

3.2 Glasgow tagger

The electron beam is impinging on a thin copper foil ($600\mu m$ thickness) which serves as bremsstrahlung target. Some of the electrons lose energy by Coulomb interaction with the copper nuclei. They emit Bremsstrahlung photons which follow a $1/E_\gamma$ intensity distribution. In such an experiment, the knowledge of the photon energy impinging on the ^{3}He nucleus is crucial (see part 8). The main role of the Glasgow tagger is to collect these informations. The electrons pass through a magnetic field of 1.85 Tesla (see figure 3.3). The scattered electrons are detected in the focal plane detector, an arrangement of 352 overlapping plastic scintillators. Once the energy of the scattered electrons is known, it is trivial to deduce the energy of the emitted photon from the relation:

$$E_\gamma = E_0 - E_{e^-} \tag{3.1}$$

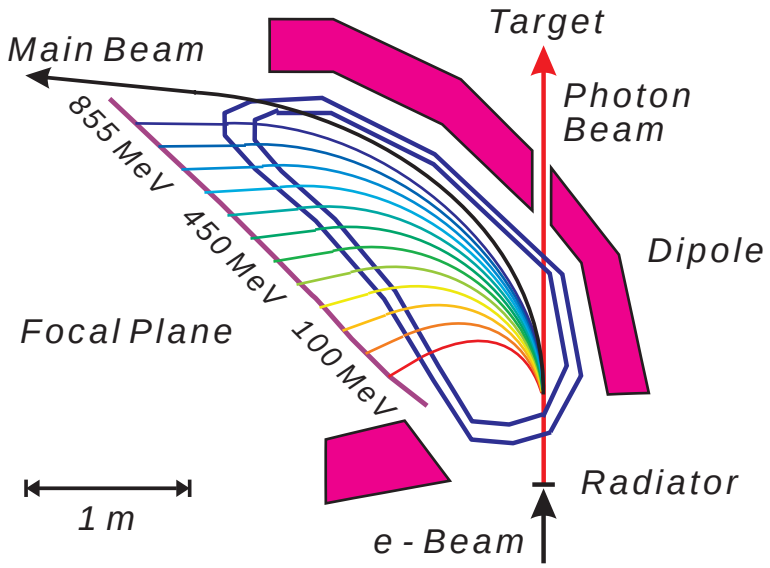

Figure 3.3: *Glasgow tagger*

where E_0 is the electron's energy coming from the accelerator, E_{e^-} is the energy on the scattered electron detected in the tagger focal plane and E_γ is the energy of the tagged photon. Since the tracks of the electrons have been simulated it is straight forward to determine the energy corresponding to the responding scintillator from a rough calibration. A more precise calibration was obtained by guiding directly the incident electron beam into the focal plane at reduced intensity and for different beam energies. The tagger covers an energy range from 250 MeV to

1.5 GeV at the MAMI-C configuration 3.1. The low energy section of the tagger easily saturates because of the high intensity of low energy photons, following the $1/E_\gamma$ distribution. Thus, for the last 153 plastic scintillator's the high voltage was switched off and the active energy range for the present experiment was 450 MeV $< E_{e^-} <$ 1500 GeV.
Even though the energy resolution of the magnet is very good ($\approx$ 100 keV), the effective resolution is limited by the geometrical width of the scintillators to 4 MeV.

3.3 The Cryogenic Target:

Under normal conditions (20°/C and 1 atm), ^{3}He is in the state of gas. Therefore its density is low. To be able to use an efficient ^{3}He target in photoproduction one has to increase the density. As the boiling point of ^{3}He is at 3.2 K, the challenge is to make a device capable to reach this temperature.
A new target system was constructed especially for the present experiment with the help of the target group of Mainz. Fig 3.4 is a technical drawing of the cryostat geometry :

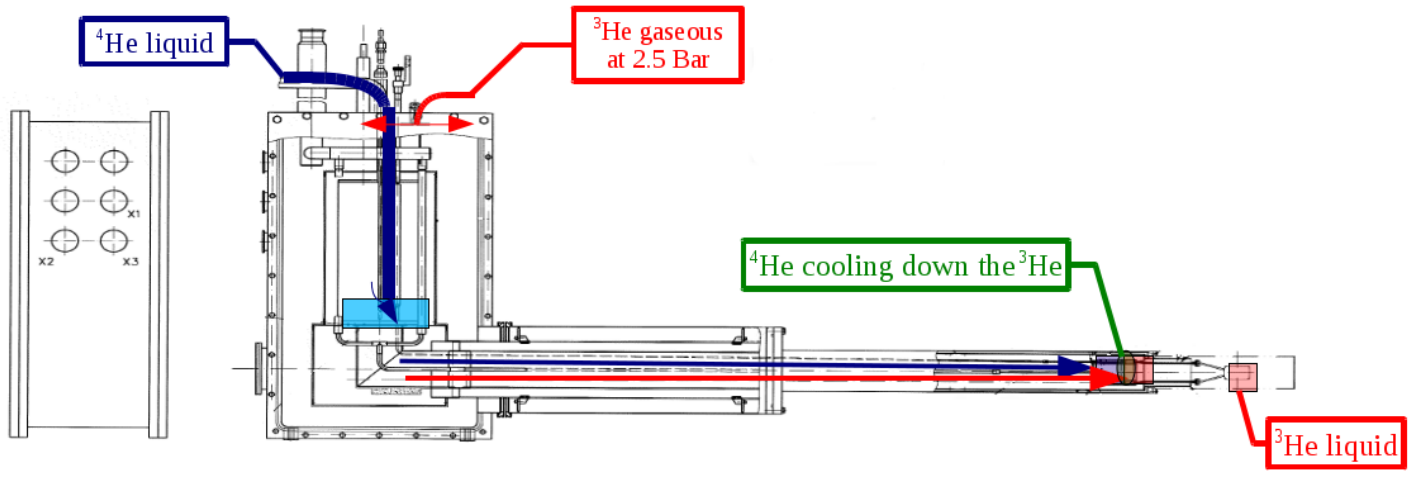

Figure 3.4: *Design of the cryostat*

The working principle of this target is simple and robust. Automatically, a container is filled with a certain amount of liquid ^{4}He provided by a Dewar via a transfer line. The liquid ^{4}He is pumped out in order to descrease the liquid's temperature in the condenser. The condenser is a copper cylinder consisting of two chambers, one for ^{3}He gas, the other for liquid ^{4}He. By heat exchange, the ^{3}He gas, which is in another compartment of the condenser will come to the liquid phase.
All the cryosystem is maintained in the cryostat at a vacuum of 10^{-4} mbar. During the liquefaction, the inner pressure decreases down to 10^{-8} mbar because of cryo-pumping. Such a procedure needs to be fully monitored by a control system.

We developed a control system based on the Labview program. This software has a direct connection with thermo-sensors placed at the strategic points of the system (along the gas and liquid ^{3}He /^{4}He lines). A precise RuO_2 resistor is mounted on the condenser in order to monitor when the liquefaction temperature is reached. This parameter is linked to the gas pressure inside the target cell. When the gas becomes liquid, this pressure drops from 1500 mbar to 1000 mbar.
Three hours are necessary to fill the target cell with liquid ^{3}He which is short compared to the hydrogen target (24 h). But, the consumption of liquid ^{4}He is high, the 400 L Dewar was changed daily during the experiment runs.
The target cell itself is a cylinder of 4.3 cm diameter and a length of 5.3 cm made of 170μm thick capton.
During the experiment, the control system recorded all cryostat parameters in a datafile for an offline analysis. So, we extracted the mean temperature given by the RuO_2, which is 2.6 K. With the formula below we can deduce the target surface density:

$$N_{^3He} = \frac{N_A}{A} \cdot \rho \cdot L_{eff} = \frac{6.022.10^{23} mol^{-1}}{3 g.mol^{-1}} \cdot 0.069 \frac{g}{cm^3} \cdot 5.3 cm = 0.73 \cdot 10^{23} cm^{-2} \quad (3.2)$$

We assumed an effective error of 1.5% resulting from the measurement L_{eff} (effective length) and the liquid temperature. Fig 3.5 shows the complete cryostat set-up standing in front of the crystal ball.

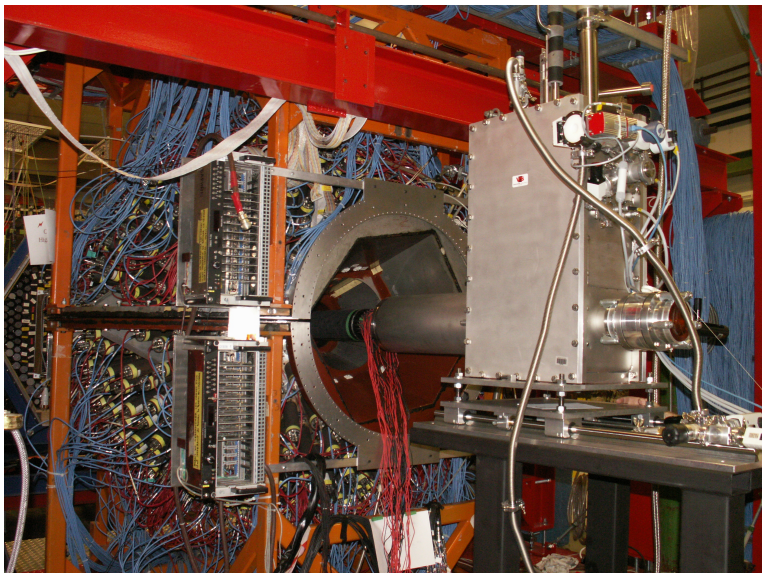

Figure 3.5: *L^3He target*

3.4 Overview of experimental setup

In 2002, the Crystal Ball detector was moved from its previous location at BNL[1] to the MAMI facility. The opportunity to use it coupled with TAPS as forward detector with the beam provided by MAMI allows the investigation of many different photoproduction reactions. The combined calorimeter made of the Crystal Ball, TAPS and their subsystems respectively the PID (particle identificator) and the Veto is an excellent tool. It provides a very good time and energy resolution, an accurate determination of the nature of the particles and covers a large solid angle (approx. 4π). This feature is required to measure reactions involving a large number of particles in the final states like: $\eta \to 3\pi^0 \to 6\gamma$ with a reasonable detection efficiency.

3.4.1 The Two Arms Photon Spectrometer, TAPS

The TAPS detector was arranged as a segmented wall of 364 BaF_2 scintillators. Each scintillator is 250 mm long and has a hexagonal cross section of inner radius 29.5 mm (see figure 3.6), its properties are summarized in table 4.2.

[1]Brookhaven National Laboratory

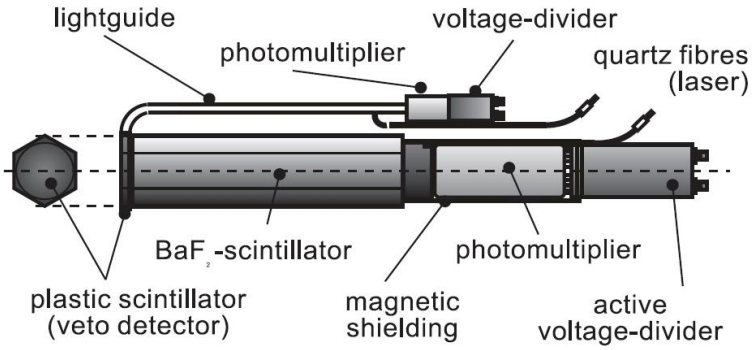

Figure 3.6: *TAPS crystal, a plastic veto is placed in front of each element in order to discriminate charged from neutral particles.*

BaF_2 has been chosen for its good time and energy resolution derived from its scintillation modes. Indeed, the scintillation light of this crystal consists of two components which differ by wavelength and especially decay time. This distinction allows the application of the so called Pulse Shape Analysis (3.7.). Moreover, due to the fast rise time of the scintillation pulse, the intrinsic time resolution of a single crystal is very good, about 200 ps. This is an essential feature for an accurate particle identification using the time of flight of the particle.

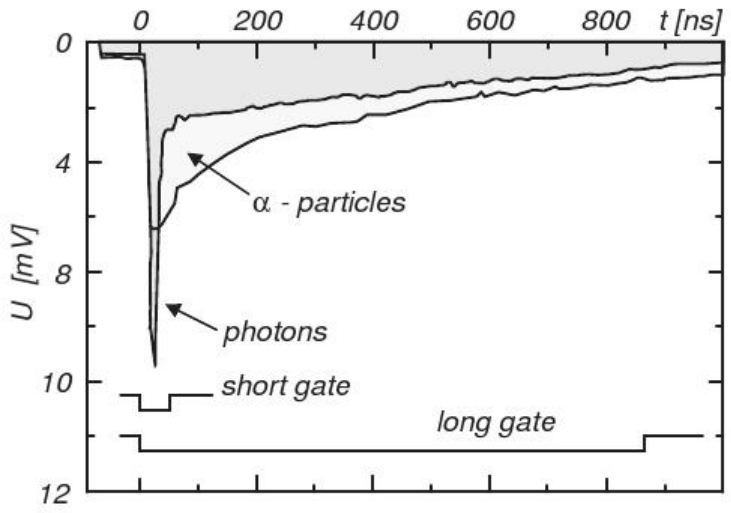

Figure 3.7: *Pulse shape of an α-particle and a photon. The type of the particle is determined by the measurement over a long and a short time gate*

Elements	BaF_2
Densityρ^3	4.89
Refraction index n	1.56
Radiation length X_0[cm]	2.05
Moliere Radius r_m cm	4.03
Relaxation time fast component [ns]	0.7
Relaxation time slow component [ns]	620

Table 3.2: *Properties of BaF_2 elements.*

3.4.2 TAPS Veto

As mentioned, each TAPS element is combined with a plastic scintillator; the so-called veto. In the previous experiment at MAMI, the Veto was 5 mm thick and hexagonal. As the light emission was low, only the hits were recorded as a binary digit in a pattern unit but not the particle energy loss. The signature of a proton and a photon is obvious. If a plastic veto and the corresponding TAPS element are hit, a charged particle is detected, if it is only the TAPS element, it is a photon or a neutral particle.

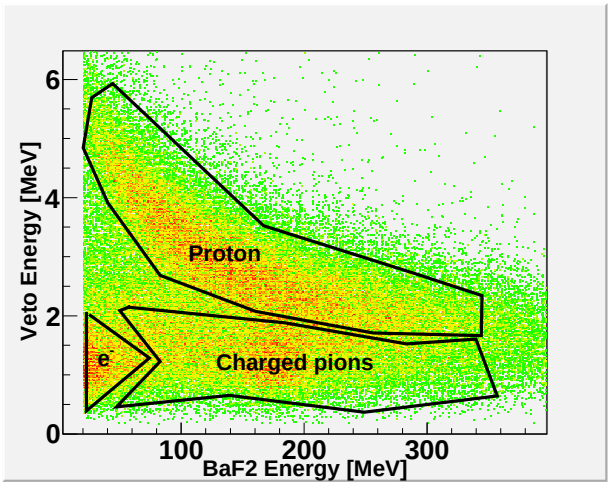

Figure 3.8: Energy loss in VETO versus deposited energy in TAPS

The whole plastic scintillator is read out via an optical fiber attached to a multichannel photomultiplier. In 2007, a new version has been developed by the detector group of Giessen University [14]. It consists of a 6 mm thick hexago-

nal elements, and each channel is connected to a photomultiplier (PMT) but, in addition, a CFD[2] is also connected to each channel. Thus an ΔE (from veto) versus E (from TAPS) analysis can be used for particle identification. A typical spectrum with the "banana" shape as the proton signature and some residual background from electrons is shown in fig 3.8.

The discrimination between charged and neutral particles is more efficient with this improvement, moreover it can even distinguish π^+, proton, deuteron.

3.4.3 TAPS Electronics

Figure 3.9 shows a schematic view of the the TAPS electronic set-up:

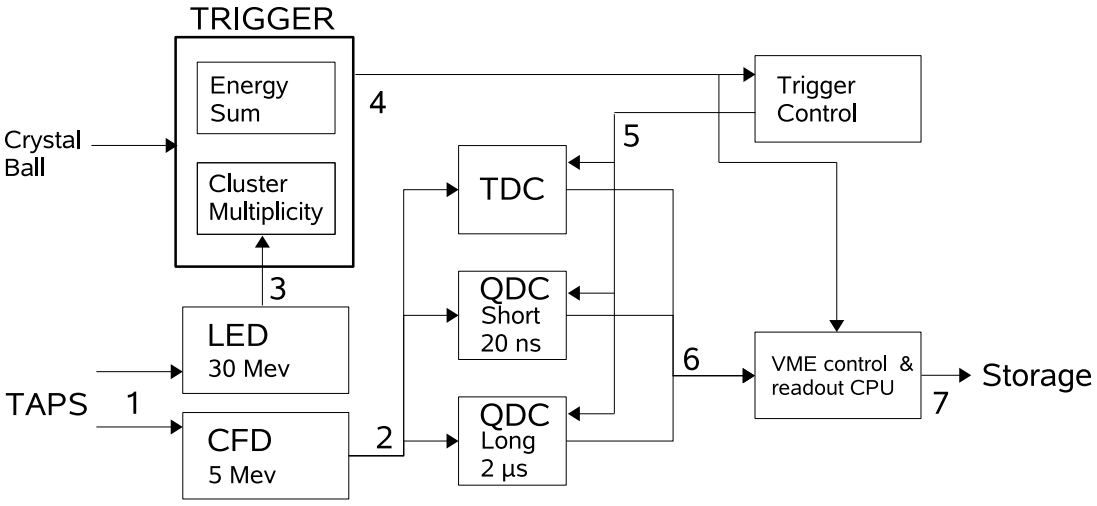

Figure 3.9: Schematic illustration of the Electronic set-up

Only one VME module is necessary for digitization of the analog channels coming from :

- LED1 [3] (Low) and LED2 (high) thresholds for the trigger decision (first level trigger)
- CFD used for the indexation of the responding crystals and time information.

[2]Constant Fraction Discriminator
[3]Leading Edge Discriminator

The signal from the BaF_2's photomultiplier is send to the TAPS readout board. In this board the signal is splitted to three discriminators : LED1 (low), LED2 (high), CFD. Specific values are set ① in these discriminators. If the signal is above the CFD threshold, a start command is sent to the QDC[4] for the energy integration (short and long gate) and to the TDC [5] for time measurement ②. At the same time, the signal will be sent to the trigger box if the deposited energy is higher than the LED threshold. ③.
The time measurement ends when a stop signal from the trigger is send to QDC and TDC. ④ this information is recorded in the mass storage on the data acquisition computer.

3.5 Crystal Ball (CB)

3.5.1 CB System

"CB" is a segmented, electromagnetic calorimeter. It was used in various experiments since its construction at SLAC. It was used at DESY in Hamburg, at AGS in Brookhaven, and was moved to the Mainz MAMI accelerator in 2002. It is divided into two movable hemispheres which allow access to the center target region and simplify transport of the system. Originally, the crystal ball was integrated to a cyclotron. For this reason two holes at the front and the rear of the sphere were made in order to leave space for beam entry and exit.
The 672 elements of the detectors are made of Sodium Iodide (NaI(Tl) crystals), with a radiation length of 15.7 cm. The crystal arrangement is based on the geometry of an icosahedron.

The spherical shape has twenty triangular shapes separated into 4 minor triangles which consist of nine individual crystals.

[4]Charge to Digital Converter
[5]Time to Digital Converter

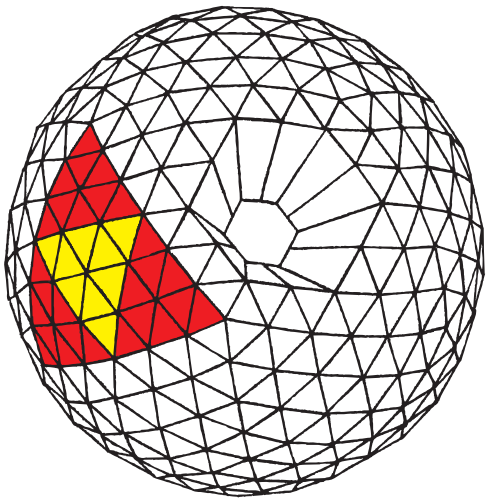

Figure 3.10: GEANT 4 simulation design for CB.

The Crystal Ball system consists of one outer detector, the Crystal Ball, with an inner detector the particle identificator (PID). The combination of these two detectors allows the identification of γ rays and charged particles, it covers 94% of the solid angle.

3.5.2 Crystal Ball electronics

The electronic system of the crystal ball and the PID were upgraded in 2004. The 30 years old device was only able to treat several counts per seconds. The improvement consists of a new set of electronic devices. This set-up can support the high rate from the electron beam ($\sim$ 1000 events per second) [12].
The CATCH TDC's [6] were designed for the COMPASS experiments (CERN) and the trigger electronic was previously made for WASA [12]. In the following, fig 3.11 represents a simple view of the signal path from the photo multiplier to the hard disk storage:

[6] Compass Accumulation Transfer and Control Maintenance

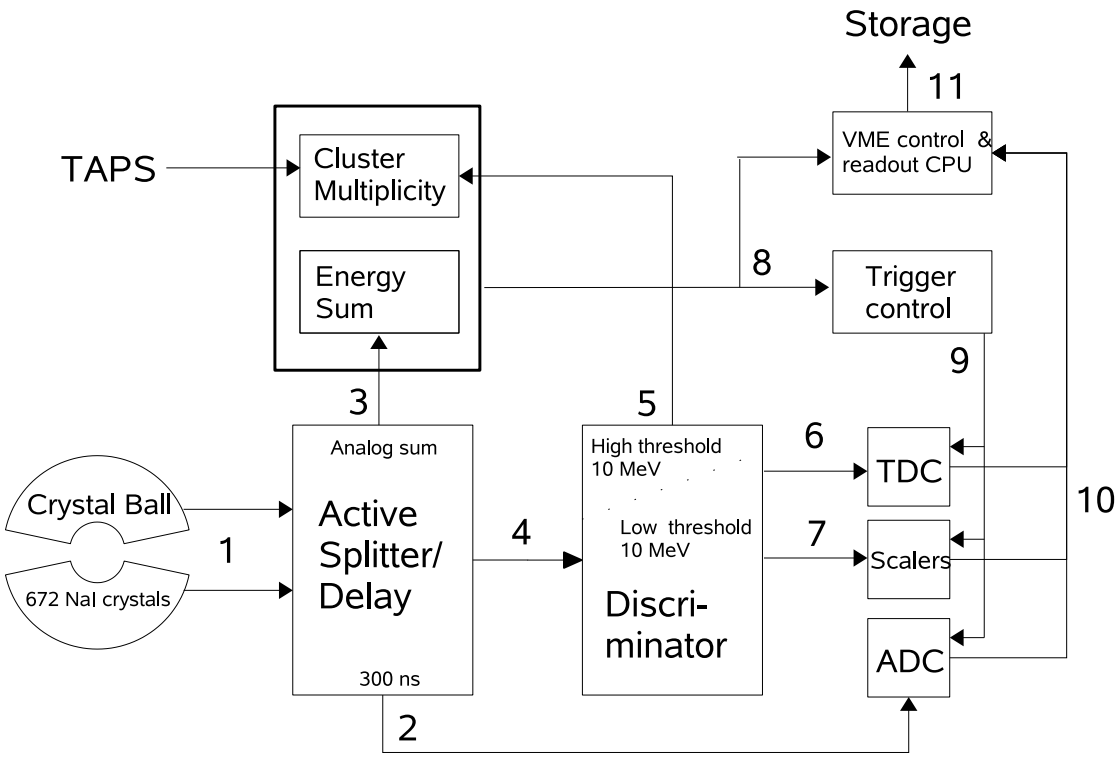

Figure 3.11: CB Electronics

1. Signals from the 672 crystal PMS are grouped in 2 x 8 cable groups and sent to 42 splitter ①. In a first stage the 16 signals are sent to different destinations:

   - to the ADC's ② delayed by 300ns
   - to the trigger box ③
   - to the discriminator ④

2. If the summed signal is above 2 MeV (low threshold) the TDC ⑥ and the scalers modules ⑦ start.

3. The number of crystals where the deposited energy was above 20 MeV (high threshold) is sent to the cluster multiplicity trigger ⑤.

4. the trigger box ⑧ generates a trigger signal. The trigger send a stop to analyze new events in TDC, scalers, and ADC modules and allow to digitize the present information⑨. The time when these modules are blocked determines the dead time of the electronics.

More detailed information can be found in D.Krambrich thesis [22].

3.5.3 The Particle Identification Detector: PID

Due to its short distance from the target no time-of-flight analysis is possible and NaI has no PSA. Therefore an inner detector is needed for charged particle identification. The PID was built by the Glasgow and Edinburgh nuclear physic groups [10]. It was successfully installed and commissioned in summer 2004. In 2007, a PID V2 was designed and installed in the experiment set-up in order to take into account the new energy range of MAMI-C (see picture 3.12), its shape and performance are similar to PID v1.

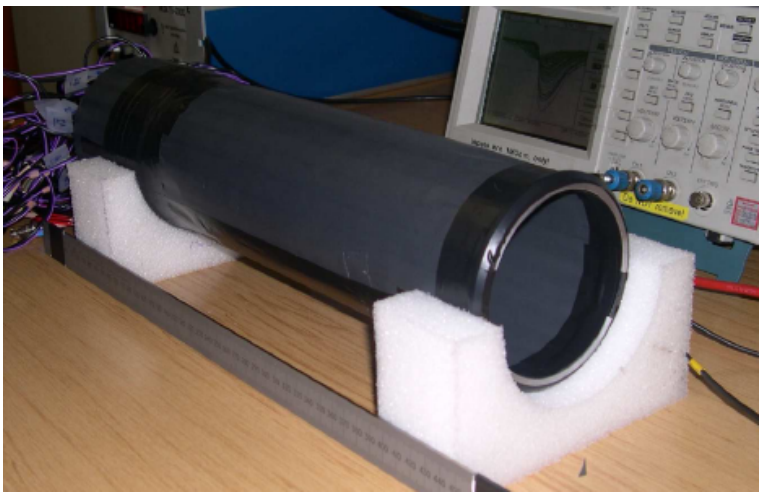

Figure 3.12: *PID standing out of the experimental set-up*

The particle identification detector consists of a segmented cylinder of 24 plastic detectors. The particle identification is performed by comparing the total energy deposition in the crystal ball with the small energy ΔE deposited in the PID scintillators by charged particles.

3.5.4 Experimental trigger

An experiment at this energy produces a huge amount of events. But depending on the studied channel, just a very small part of these events is of interest. As we are limited by the memory of the mass storage but also by the setup dead time,

it is important to set a good filter.
For this task, a trigger box was built. It combines all information from the different detectors and generates a trigger signal. Figure 3.13 shows a schematic view of the trigger box and its implementation in the whole electronics.

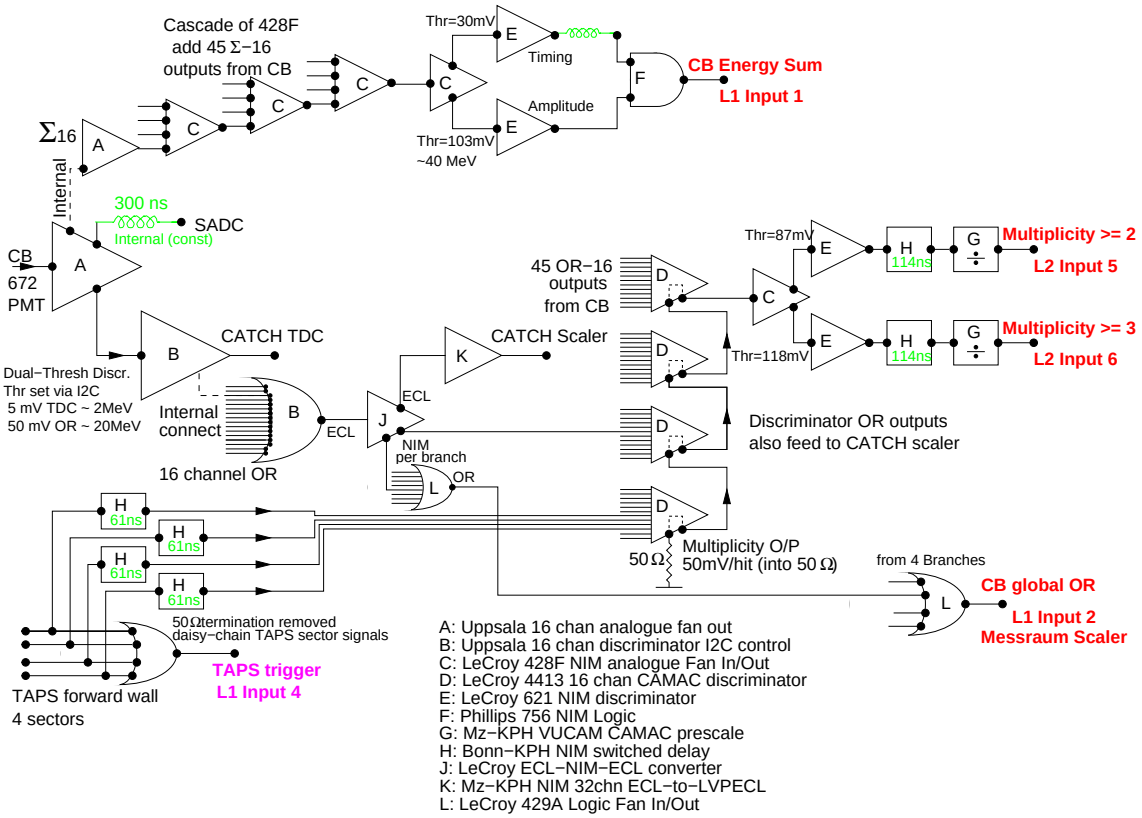

Figure 3.13: *Schematic view of the electronics set-up and trigger restriction*

We can distinguish two different and independent parts: the cluster multiplicity and the CB energy sum.

- **The cluster multiplicity** is used to reject or keep events according to the number of final state particles. For this purpose, the active splitter in the crystal ball electronics divides the 672 NaI crystal readout in 45 logical segments made of 16 contiguous crystals and calculates the analog energy sum of each individual segment. The typical size of a single energy deposition is small enough to be contained within one logical segment so that we can assume that one firing segment corresponds to one particle. The analog energy is then sent to the discriminator where, if the energy sum

is above a 20 MeV threshold, a so-called multiplicity hit will be recorded. TAPS contributes to this trigger in a similar way: it has been split in 4 logical segments made of 128 BaF_2 crystals. If any crystal in a segment has an energy deposition above the 20 MeV LED threshold, a multiplicity hit will be recorded. The trigger condition was therefore set to keep events with two or more multiplicity hits (M2+) and to reject events with a lower multiplicity.

- **The CB energy sum** concerns only the crystal ball. The CB energy sum of the Crystal ball is simply constructed by summing the analog energies of all 672 NaI crystals. If the total energy deposition is below a definite threshold 300 MeV in our experiment- the event will be rejected. This is not a very stringent condition and will keep a lot of single pion events. A higher energy threshold could have been set in order to reject more low energetic background if the TAPS energy had been taken into account in the energy sum. However, for technical reason- the TAPS electronics boards haven't been designed to provide a readout of the analog energies- this has not been implemented.

3.5.5 Data taking and experimental conditions:

The data were taken in November 2008, with the beam energy of 1508 MeV. The trigger conditions and the beam intensity had been changed in order to optimize the detection of multi-mesons. The parameters set during the run are summarized in table 3.14.

Period	November 2008
Running Time	300 h
Beam Energy	1508 MeV
Tagger NMR	1.832 T
Tagged photon Energy	450-1508MeV
Trigger condition	M2+, CBEnergy>300 MeV
Beam current	8 nA
Target Temperature	2.6K
Target surface Density	$0.73{\cdot}10^{23}$ cm^{-2}
Polarization	circular
Collimator diameter	3mm
Radiator	10μm Cu
Tagging Efficiency	72%
TAPS LED Low	30 MeV
Count rate (interrupt)	890 Hz
Amount of data	1.01Tb
Number of η mesons	1 200 000

Table 3.3: Summary of the most important experimental conditions. More technical information is available in the A2 logbooks and run sheets conserved at Mainz

Chapter 4

Data calibration, analysis, particle identification

After the end of the experiment, the raw outputs from all detector elements are stored as digital data on mass storage. In the first step of the analysis these raw data have to be calibrated in energy and in time. This chapter will explain this procedure.

4.1 Analysis software

AcquRoot was developed by the Glasgow Group especially for the first run of experiments for CB@MAMI in 2004. It is designed to read out and store the data coming out of the detectors and to provide an efficient framework for their analysis. AcquRoot is an upgrade of AQU, the software formerly used at MAMI since the completion of MAMI B and continued with the upgrade of MAMI C. It consist of an elaborate, multi-threaded program mainly written by J.R.M. Annand from the university of Glasgow. All relevant technical information can be found in [3]. From a user point of view, AcquRoot might simply be seen as an extension of ROOT , the high energy physics data handling suite provided by CERN. Written in C++, ROOT uses the modularity of this language and consists of a large number of classes, all of them performing a specific task. Using the same principle, AcquRoot can be seen as a graft, enriching ROOT with classes performing the specific tasks needed to handle the data from our

detectors. Fig 4.1, shows the structure of AcquRoot. This picture perfectly illustrates the advantages in using an object-oriented programming language: the basic operations such as energy and time calibration are performed locally (green): a dedicated class is written for each subsystem of each detector. For example, TA2PlasticPID deals with the CB NaI crystals. Going one step higher (blue), the data from each subsystem is grouped in three classes corresponding to each detector, TA2Tagger, TA2TAPS and TA2Crystalball where more specific work requiring information from more than one subsystem is performed. The typical example here is the particle identification, which in the case of TAPS combines informations from the BaF_2 crystals and the veto. Finally, all informations from the three detectors are merged into a central TA2Physics class in which the events are reconstructed and all the subsequent physics analysis is performed.

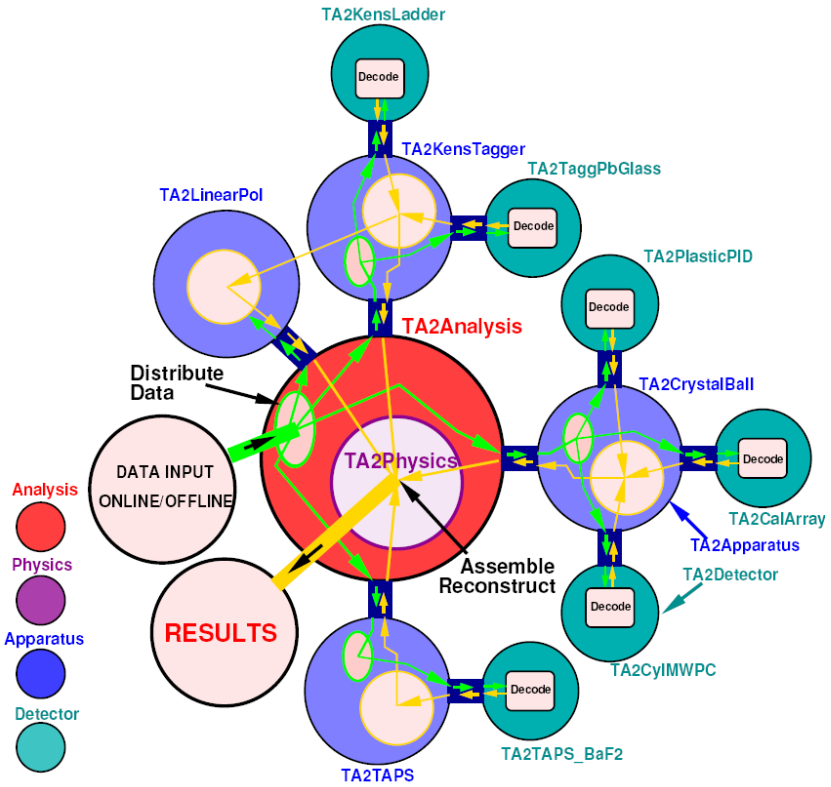

Figure 4.1: Tree organization of AcquRoot: arrows represent the data flow during the analysis process [3]

4.2 Calibration software

As the experimental conditions are changing during the beamtime, one has to make a different calibration for each day of the experiment (actually we can choose all possible time windows). Here a compromise between counting statistics (setting a lower limit for the time window) and time constants of detector instabilities (setting the upper limit) has to be found. For this purpose, our group has developed a library (CaLib) based on C++ and the CERN-ROOT library connecting and storing all information in MySQL especially for the calibration procedure. A schematic view of this library is shown in figure 4.2

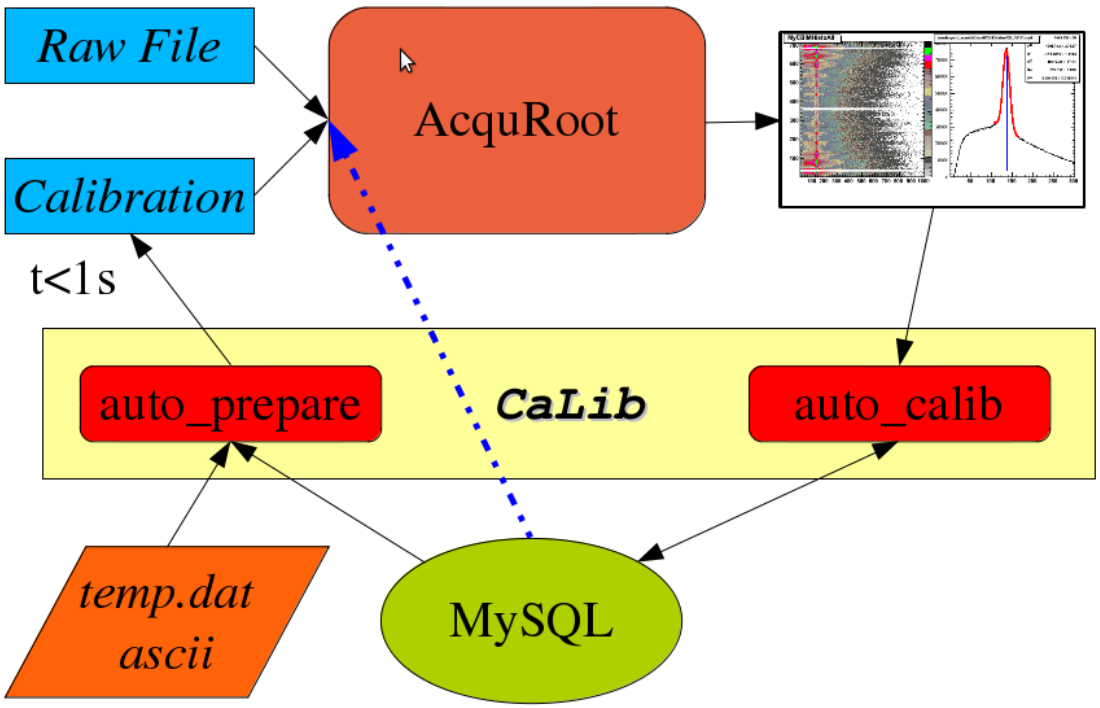

Figure 4.2: *Schematic view of CaLib. The system is managing the access to the database where all calibration constants are stored. A specific calibration file is made for each datafile.*

At the beginning we have to scan the entire data from the experiment with similar calibration parameters. Usually we expect a smooth performance of all detector systems. In order to increase the experimental resolution we are trying to choose the shortest possible runsets. But there are conditions where due to

some breaks during beamtime the performance of detectors changed. In such cases we divide the run sets according to these changes (16 different runsets for ^{3}He). Using databases allows us to use optimum calibration parameters for each run in an automatic way. The next sections will treat individually the different calibrations.

4.2.1 Energy Calibration

Energy calibration of TAPS elements

One wants to establish a correlation between ADC channels and the real energy deposited in the BaF2 crystals. So, the so called cosmic data have been taken before and after each beamtime period, sometimes also during breaks in the data taking. They consist of long time (half a day) beam off measurements for which most of the particles detected in the crystals are muons produced in cosmic ray interactions in the atmosphere. The minimum ionizing peak of muons which lays at 37.7 MeV is shown in fig 4.3.

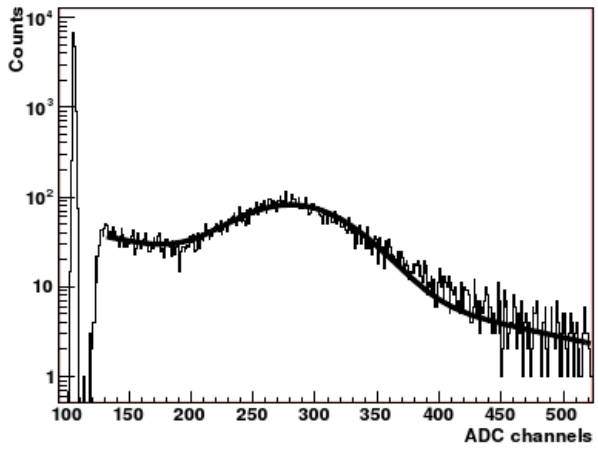

Figure 4.3: *Deposited energy of cosmic muons in BaF_2 element fitted with a gaussian plus a polynom of third order (black line). The first peak corresponds to the pedestal signal.*

These muons are minimum ionizing particles which deposit 6.45 MeV/cm in the BaF_2 crystals. In our setup, with the crystals being arranged horizontally and the muons mostly coming from above, the most likely energy deposition in the crystals is 37.7 MeV. This peak alone is not sufficient for an absolute calibration

of the energy. A second reference in the ADC spectra is provided by the TAPS pedestal pulser. During cosmic data-taking, this electronic module forced a read-out of all ADC's once per second, creating a large peak at zero energy. In order to carry out the calibrations, both peaks are fitted to determine their positions channel wise. These two values are then used to establish the matching between ADC channels and MeVs for each crystal. This procedure is applied twice, once for the long and once for the short integration.

Energy calibration of the Crystal Ball

During the commissioning phase, a preliminary calibration of the Crystal ball has been performed to set the hardware thresholds at correct levels. The NaI crystals were irradiated with a ^{241}Am/^{9}Be source. The response of the photomultiplier was adjusted using the peaks produced by the 4.438 MeV decay photons so that all 720 ADC spectra were aligned.
This low energy gain matching is not precise enough for a satisfactory calibration of the much more energetic particles involved in this experiment. The fine tuning of the calibration was done using the ^{3}He + $\gamma \rightarrow \pi^0$+ X reaction. For this purpose, the π^0 invariant mass was plotted for each NaI detector. Then the calibration of this detector module was aligned to the π^0 invariant mass: 135.6 MeV.

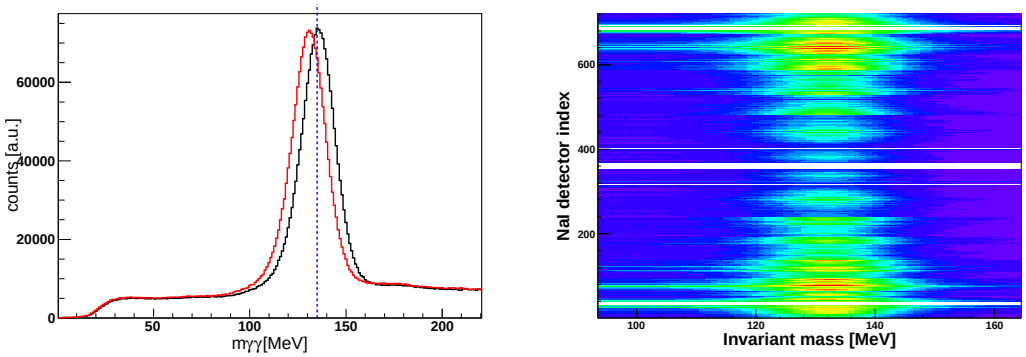

Figure 4.4: *Left: Invariant mass versus NaI index Right: π^0 invariant mass spectra for two photons detected in the CB. The Red line is before calibration, black is after the calibration of the gain. The invariant mass is at 135.6 MeV.*

With this procedure a resolution of 8 MeV was achieved for the π^0mass. Figure

4.4 shows π^0 invariant mass spectra for two photons detected in the CB before and after the calibration.

4.2.2 Time Calibration

This part will summarize the time calibration of the detector set-up and for the tagger. In order to know the total duration of the event, one has to know which signals are starting and stopping the TDC's of each detector. Table 4.1 shows the start and stop signals.

.	START	STOP
Tagger	Tagger Element	Trigger
TAPS	CFD	Trigger
Crystal Ball	Trigger	NaI Element

Table 4.1: *Summary of start and stop signal*

Time calibration of Tagger

The alignment of all tagger TDC spectra is presented in figure 4.5. It is done fitting each TDC spectrum with a Gaussian distribution, determining the mean position of this Gaussian and adding a corresponding offset to the TDC to correct for the misalignment of the peaks.

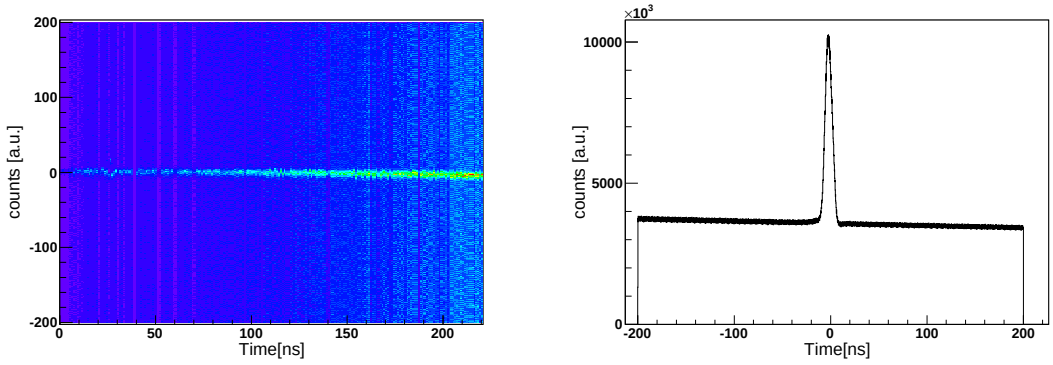

Figure 4.5: Right:*Left: Tagger time versus the tagger channel after the alignment of each single detector.Right: Tagger time for all channels*

Using, this method we can achieve an overall tagger time resolution of 10 ns (see figure 4.5, left). This width is dominated by the jitter of the trigger which start the time measurement. Since TAPS and the CB are stopped by the trigger, the jitter is removed in the relation tagger-calorimeter timing.

Taps Time calibration

The time calibration of TAPS was performed in two steps. First, all TDCs were aligned with a gaussian fit of their peaks. However, the relative alignment of the 384 TAPS TDC is not sufficient for the tagger random subtraction, the time of flight particle identification, and a good time resolution. Such tasks require to know the total duration of an event characterized by its 'beginning' and its 'end'. The time references chosen here are the tagger as the start signal and TAPS (or CB) as the stop signal. In practice, this means that we have to determine this coincidence time between the tagger and TAPS and to align all tagger and TAPS TDC. Before doing this, let's first have a look at how the TDCs start and stop signal are defined for each detector. This will define the way how TAPS and the tagger will have to be combined in order to perform this calibration.
For the tagger and TAPS, the start signal is given by individual elements. A common stop is applied by the electronic trigger. Things are opposite for the crystal ball. Since this trigger time has jitter which induces a resolution worse than the intrisic detector resolution, it is desirable to get rid of it. This is possible by the subtraction of t_{tagger} from t_{TAPS}:

$$t_{TAPS-tagger} = (t_{trigger} - t_{CFD}) - (t_{trigger} - t_{tagger}) = t_{tagger} - t_{CFD} \qquad (4.1)$$

Knowing this, each tagger element and each TAPS crystal have now to be calibrated individually. The TAPS time calibration will be done by first aligning TAPS TDC's relatively using a Gaussian fit so that all TAPS modules are aligned. A second step consisted in achieving one further alignment in combination with the Tagger to improve $t_{TAPS-tagger}$ in order to get a good time resolution. The procedure was repeated until the time resolution cannot be improved anymore. Fig 4.6 (right) shows the results of this calibration:

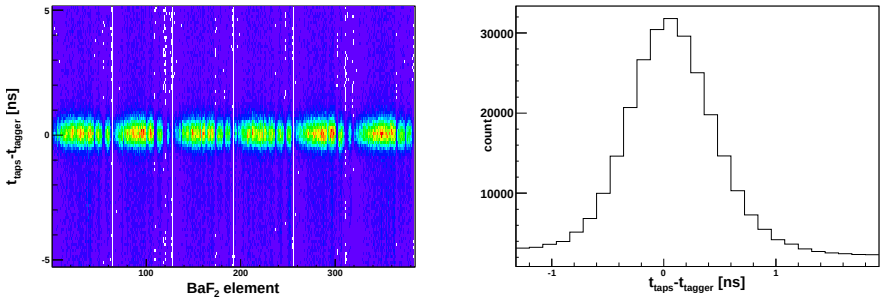

Figure 4.6: Right: *TAPS time calibration. Left: Alignment of all 384 time differences between one TAPS crystal and all tagger channels. Right: Time difference for all channels (projection of the left side plot on the X-axis). A resolution of 950 ps is obtained.*

CB Time walk calibration

Unlike TAPS and the tagger, the crystal ball time depends on the energy of the measured particles because CB uses LED's for timing instead of CFD's like TAPS (see 4.7). A particle with a small energy will need more time to activate the trigger low energy threshold that starts the measurement. A correction of this so called walk was applied to the CB times.

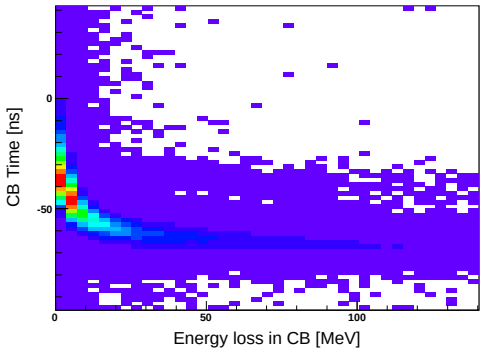

Figure 4.7: *Energy dependence of time spectra for one NaI crystal before the walk correction.*

We have:
$t_{id} = t_{meas} - t_{walk}$ with t_{walk} depending on the energy loss, t_{meas} is the time measured by the electronic set up and t_{id} the corrected time. The purpose of the

time walk correction is to calculate t_{walk}. t_{walk} is given by [17]:

$$t_{walk} = p_1 + p_2 E^{p_3} \tag{4.2}$$

Where p_1, p_2 and p_3 are the fit parameters applied to each 2D plot. The result of this correction is shown in figure 4.8

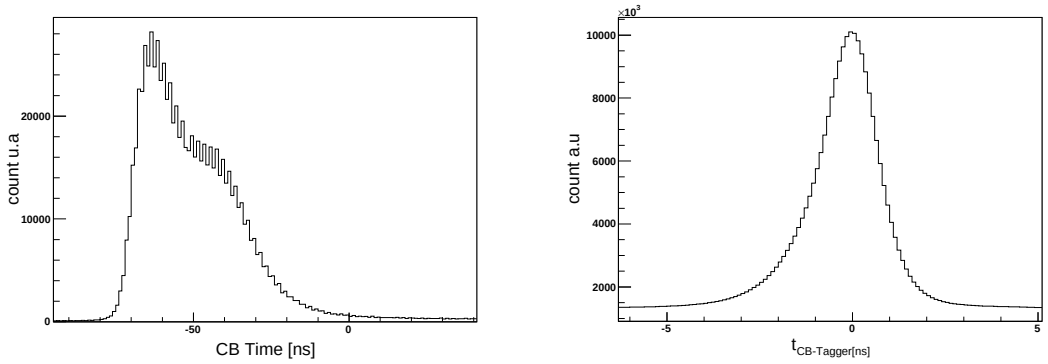

Figure 4.8: *CB Time before (Left) and after (Right) time walk correction. The width of the corrected spectrum is about 2.1 ns.*

4.3 Particle identification

4.3.1 Clusterization

When a photon hits a crystal, it creates an electromagnetic shower through electron-positron pair creation and bremsstrahlung photons. The typical size of such a shower is defined by the Moliere radius whose values - 4.3 cm for NaI and 3.4 cm for BaF2 - are larger than the size of the individual crystals. Therefore, the photon energy deposition spreads over a few crystals. The purpose of the clustering is to group all hits corresponding to a single particle and combine the informations of these neighboring crystals in order to reconstruct the particle. A clustering routine has been implemented that performs the following procedure:

- It first looks for the detector with the maximal deposited energy
- Scans all neighbors of this central crystals and adds all crystals with a non-zero hit to the cluster.

- For each added neighbor, this neighbor search is performed again and new crystals are added to the cluster

This procedure is repeated as long as crystals with non-zero hit remain. More and more clusters are built that way until no more isolated hit remains in the list of "activated crystals". Two overlapping clusters will be interpreted as one single cluster, but only a small part of events is lost this way.

4.3.2 Principle of particle's energy and position reconstruction

After the identification of the cluster, the next level is to determine the time, the energy and the position of the incident particles. The time is taken as the time of the central element of the cluster and the energy is the sum of all individual crystal energies. The position is more problematic. A proper determination is obtained when weighting the position of each crystal in the cluster with the square root of the deposited energy given by the formula [15]:

$$(x_x, x_y, x_z) = \frac{\sum_{i=1}^{N_{Crystals}} x_i \sqrt{E_i}}{\sum_{i=1}^{N_{Crystals}} \sqrt{E_i}} \tag{4.3}$$

Where x, y, and z are the position of the electromagnetic shower, the coordinates x_i, y_i of the clusters elements are weighted and summed up by the energy deposition E_i corresponding to the detector index.

4.3.3 Flight path correction

Due to the wall structure of TAPS, particles detected in the outer ring of TAPS are coming askew. A shift between the position where the particle is supposed to be detected and the actual position appears. This is illustrated in Fig 4.9.

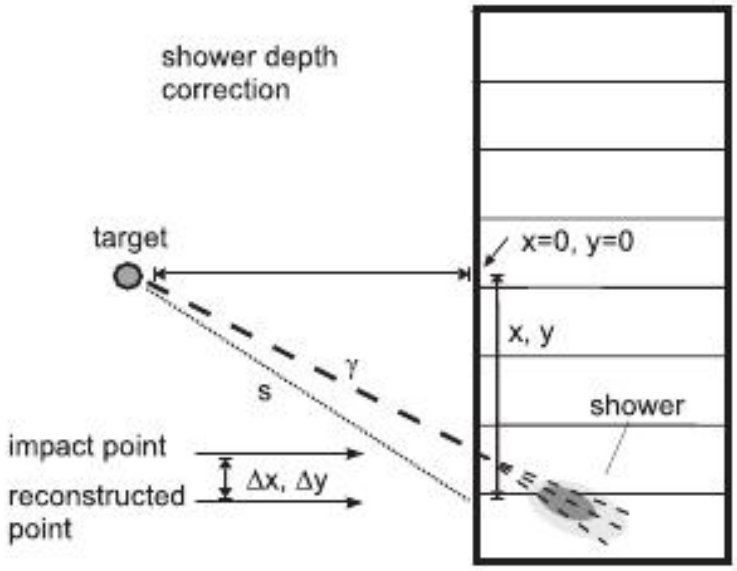

Figure 4.9: *flight path correction in TAPS [16]*

Each position is corrected by the factor given by:

$$\Delta x = \frac{x}{s + t_{max}} t_{max} \tag{4.4}$$

and

$$\Delta y = \frac{y}{s + t_{max}} t_{max} \tag{4.5}$$

Where t_{max} is the depth corresponding to the maximal energy deposition given by:

$$t_{max} = 2.05 \cdot (ln \frac{E}{12.7MeV} + 1.2) \tag{4.6}$$

E is the shower energy in MeV, The critical energy is equal to 12.7 MeV and the radiation length of BaF_2 is 2.05 cm.

4.3.4 Taps particle identification

Time of flight

Due to its characteristics (excellent time resolution, placed relatively far from the target cell), a time of flight analysis is possible for TAPS. By definition, the time of flight is either the time difference between the tagger and the time of the

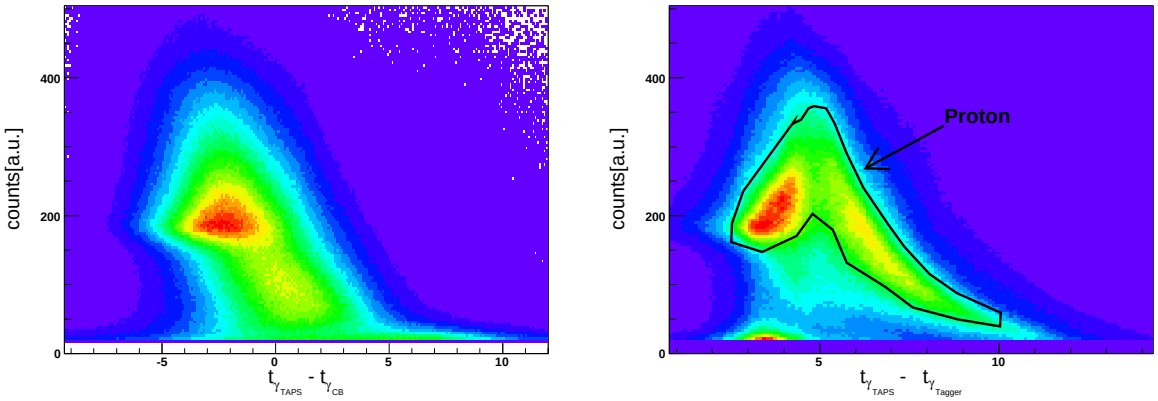

Figure 4.10: *Left: Time of flight with CB as time reference. Red mark is due to high energy photons coming from the quasi free $\pi^0 p$ reaction. Right: Time of flight with Tagger as reference time. The black line indicates the proton region (so called banana cut).*

cluster in TAPS or the difference between CB and TAPS time (see Figure 4.10).

This spectrum was constructed using the $\gamma + {}^3\mathrm{He} \rightarrow \pi^0 +$ p reaction. The 2 γ invariant mass was computed to be sure they effectively stem from a π^0. Results presented in 4.10 show a well defined curved zone corresponding to protons. Some photons or electrons from background reactions can also be seen at t = 0. The proton region is then fitted manually (black line) to define a cut to be used in subsequent analysis: a particle inside the delimited zone will be marked as a time of flight particle (i.e. a proton for example).

Veto Energy loss

Another method to distinguish charged particles is to use the plastic veto in front of each BaF_2 element. In the previous set-up, only the fired/non fired information could be used for particle identification i.e. only charged-neutral separation was possible. A charged particle was identified when the veto of the central crystal or the veto of any neighbor of the central module was activated.
Now, the plastic veto gives more than a yes/no information because an ADC is connected to each plastic detector. So it is possible to construct spectra of energy loss in the Veto versus energy deposition in Taps for the same hit. In fig 3.8 two zones are defined, to allow an identification of a charged particle, in particular a proton.

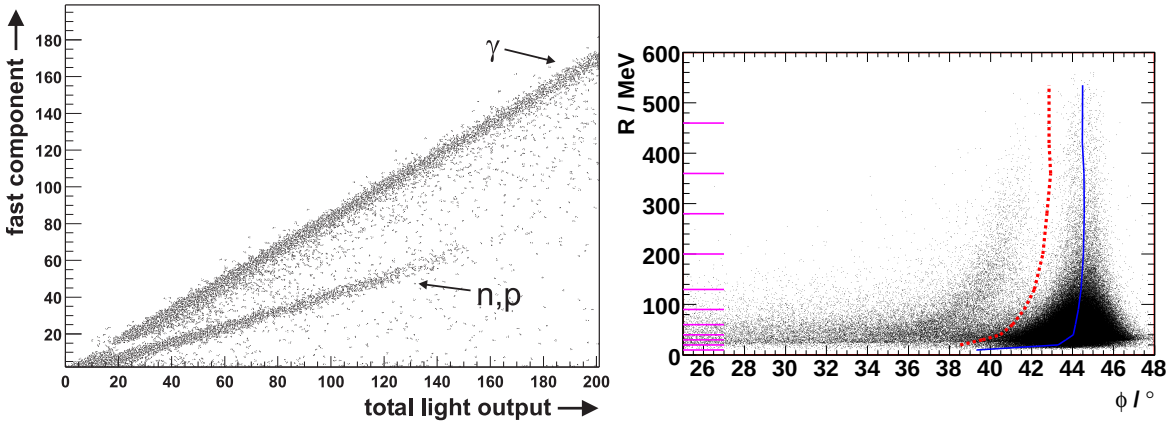

Figure 4.11: *Left: Long gate versus short gate. Right: Same representation in polar coordinates*

Pulse Shape Analysis (PSA)

As mentioned in part 3.4.1, BaF_2 has two scintillation light components. This property is used to discriminate baryons from electromagnetic showers. To achieve this, the two different ADC energy values determined using the long (- 2μs)- and short (-30 ns) - integration times are plotted versus each other as shown in figure 4.11.
The short and long gate energy signals have been calibrated such that photons appear at the 45° line in this plots. However, this representation is not very efficient for the particle separation in many modules. A more efficient method uses polar coordinates defined as:

$$R = \sqrt{E_{long}^2 + E_{short}^2} and \Phi = \arctan \frac{E_{short}}{E_{long}} \tag{4.7}$$

In this representation, the identification is easier, a vertical zone at 45° is corresponding to photons and a curved zone at smaller angles is corresponding to massive particles. The border between the two bumps is determined by projecting bands in R of these plots on the ϕ axis. The projection is fitted by a Gaussian function to determine the peak position and the 3σ border (see example fig 4.12). The identification is made by using the 3σ values together with the polar coordinate plots. A particle above 3σ is a photon and below marked as a proton.

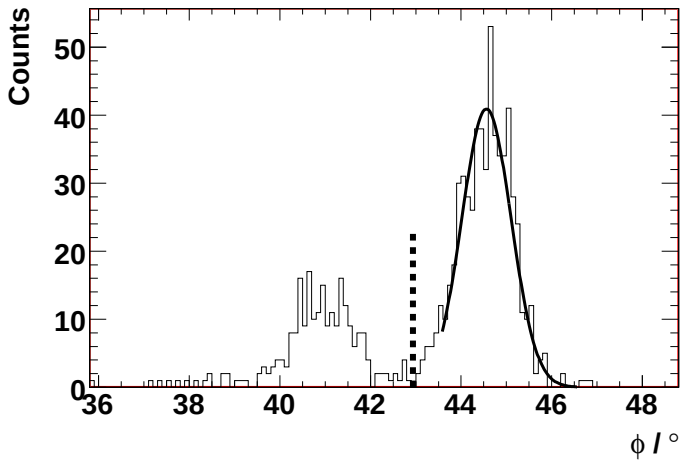

Figure 4.12: *Projection of Fig 4.11 on the x axis (for R = 200 MeV). The data is fitted to determine the peak position and the 3σ interval.*

4.3.5 CB particle identification

PID Banana plot

The PID is used to determine the nature of charged particles in the crystal ball. The particles are identified using the energy they deposit in the PID scintillating elements, which depends on their nature. The proton energy deposition ranges from 1 to 3 MeV depending on its energy. For each PID element, the energy of the charged particle is plotted against the total energy deposition in the crystal ball.
24 plots such as figure 4.13 are produced and show a clear separation between π^+ and protons. These plots show a zone at $\Delta E \approx 400$ keV corresponding to π^+ and a curved zone at higher energies corresponding to protons. Each zone is marked by hand. Using this cut, particles inside the top zone are marked as protons and in the bottom zone as π^+ mesons. At lower energies, a peak of background electrons can be seen.

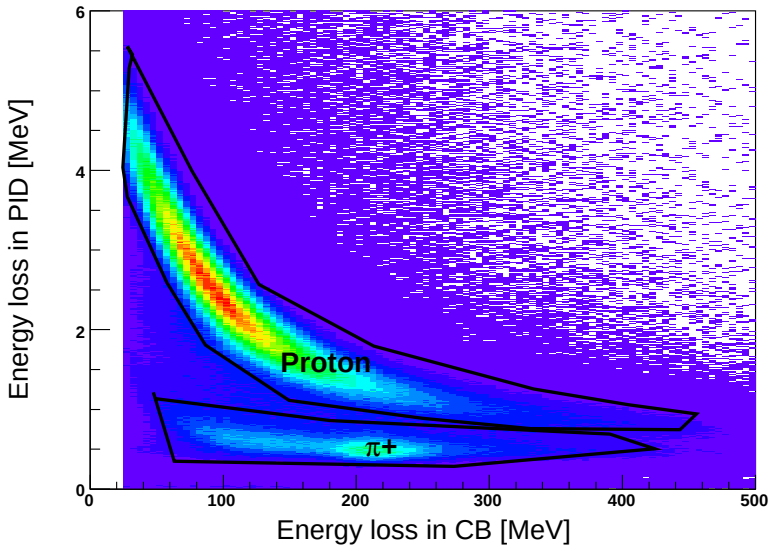

Figure 4.13: *Crystal ball versus PID energy deposition. Proton and π^+ zone are delimited by hand.*

4.4 Subtraction of the combinational background

During the experiment the beam intensity was usually so high that together with each event in the Crystal Ball/TAPS setup a number of electrons was detected in the tagger focal plane. Only one of those electrons corresponds to the bremsstrahlung photon which induced the reaction in the helium target. The other photons have not passed the collimator or have not interacted in the target. In order to identify the correct electron the timing measurement between the tagger and the production detectors is used. Obviously electrons corresponding to photons that have reacted in the helium target should be in coincidence with the reaction products ("prompt"), while the others appear at any time with respect to the reaction products ("random"). For each electron detected in the tagger, the time difference $\Delta t = t_{e^-} - t_{detec}$ is calculated where t_{detec} is the average time of all photons detected in TAPS (if TAPS is hit more then one time this is the time reference) and of all photons detected in CB (if TAPS is not hit the time of CB is the reference) for the event. The result is shown in figure 4.14: which is called the coincidence plot.

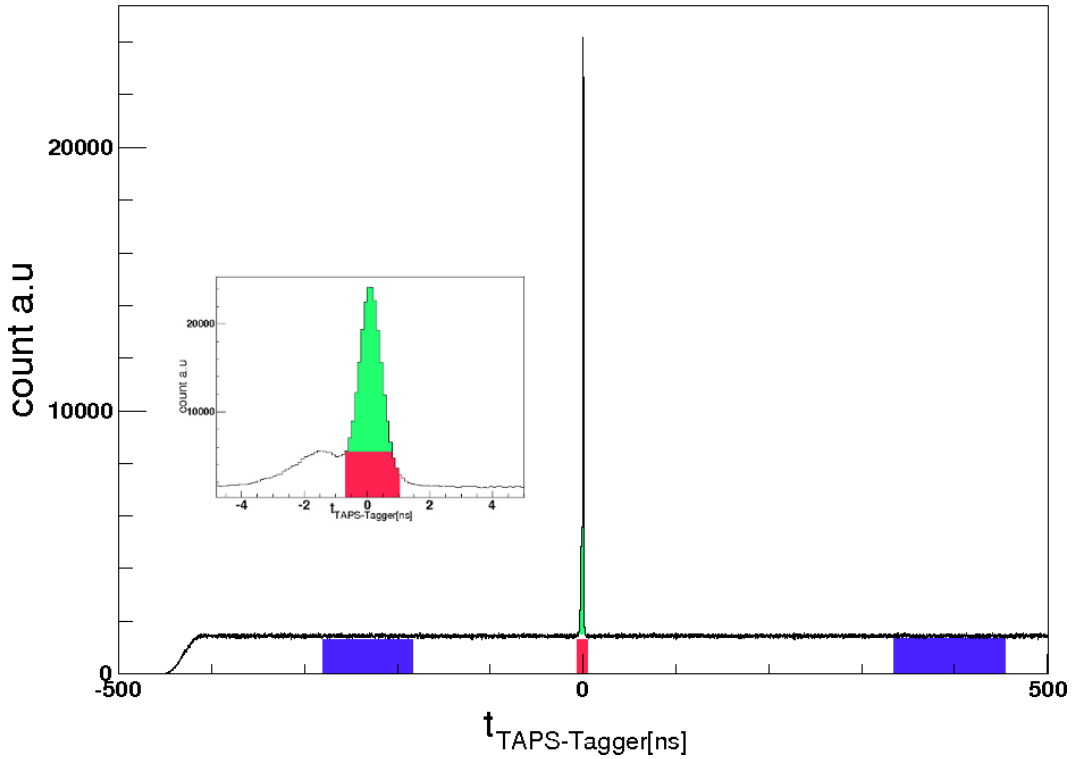

Figure 4.14: *Relative timing of CB and tagger. The marked regions corresponds to the coincidence (in red) and the background.*

In this coincidence plot, the three necessary zones needed to perform this random subtraction have been highlighted. In the zone centered around zero, the prompt electrons appear in the green zone while the random electrons appear in the red zone. As both contributions can't be distinguished with a simple cut on the time of flight, a third (blue) zone is defined far away from the prompt peak, where it is sure that the detected electron was a random electron. The events from the blue zones (normalized to the width of blue compared to red) are subtracted from the events in the prompt window.

4.5 Invariant mass reconstruction

Two photon decay reconstruction:

In most cases the π^0 decays into two photons, for the η meson the branching ratio for $\eta \to \gamma\gamma$ is 39.3%. By definition, M_{inv} (the invariant mass) is given by

the formula:

$$M_{inv} = \sqrt{\boldsymbol{p^2}} = \sqrt{\boldsymbol{p_1} + \boldsymbol{p_2}}^2 = \sqrt{\boldsymbol{p_1}^2 + \boldsymbol{p_2}^2 + 2\boldsymbol{p_1}\boldsymbol{p_2}} \tag{4.8}$$

Where p_1 and p_2 are the quadrivectors of γ_1 and γ_2. $p_1^2 = p_2^2 = 0$ because the invariant mass of a photon is zero and eq. [4.8] becomes:

$$M_{inv} = \sqrt{2p_1p_2} = \sqrt{2E_1E_2 \cdot (1 - \cos(\psi_{12}))} \tag{4.9}$$

Where E_1 and E_2 are the energies of the two photons and ψ_{12} is the opening angle between them. Fig 4.15 shows the invariant mass of two photons according to the eq. [4.9]. The π^0 mass peak ($M_{\pi o}$ = 135.9 MeV) and the η mass peak (M_η = 545.4 MeV) are identified. The background below the peak is essentially coming from misidentified photons and combinational background.

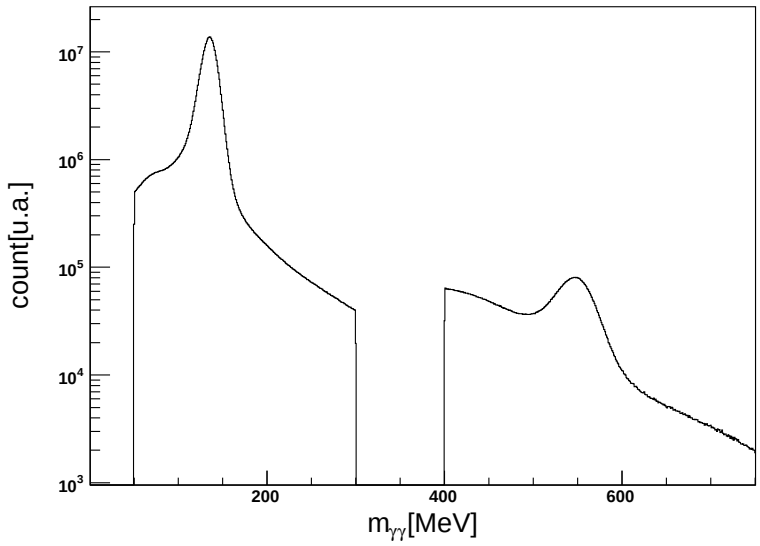

Figure 4.15: *Two photons invariant mass for CB and TAPS. π^0 and η are respectively at 134.8 MeV and 544.9 MeV. Between 400 MeV and 700 MeV the spectrum is scaled up by a factor of 100*

$\eta \to 3\pi^0 \to 6\gamma$ reconstruction

The η decays to $3\pi^0$ with a branching ratio of 32.5%. The quadrivectors of the best combination of three photon pairs selected by a χ^2 test (see D)were summed up. A cut between 110 and 160 MeV on the invariant mass of each pion has been

applied. The four-vectors of the three pions were then summed up and the η was reconstructed. A constraint on the $3\pi^0$ mass has been applied to the momentum of each $\gamma\gamma$ pair in order to improve the experimental resolution.

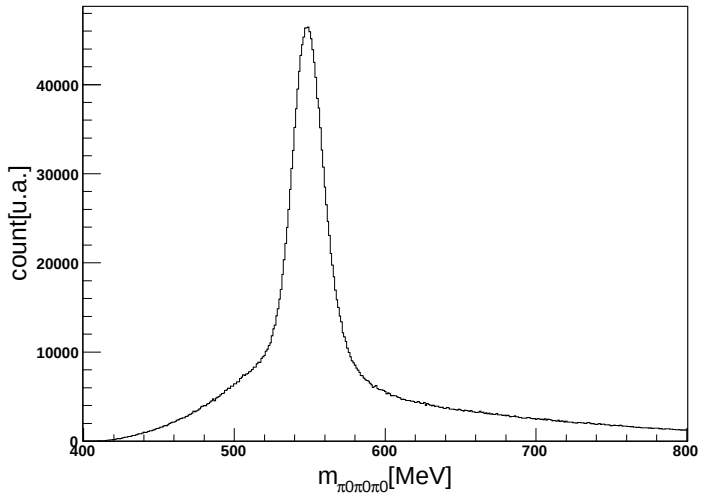

Figure 4.16: *$3\pi^0$ invariant mass reconstructed from six neutral hits for the whole energy range*

4.6 Software Trigger

The Crystal Ball energy triggers were modeled and included in the analysis of the simulated data.

4.6.1 Multiplicity Trigger

The multiplicity trigger in the hardware electronics for the experimental data was checked by measuring the energy of crystals when three clusters were identified. For an M2 trigger, this required at least one crystal from each cluster to exceed the threshold applied by the discriminators in the hardware. Fig 4.17 shows the energy deposited in the crystal with highest energy deposition in each cluster when two clusters are identified. It is clear there is a sharp drop in counts at 20 MeV.

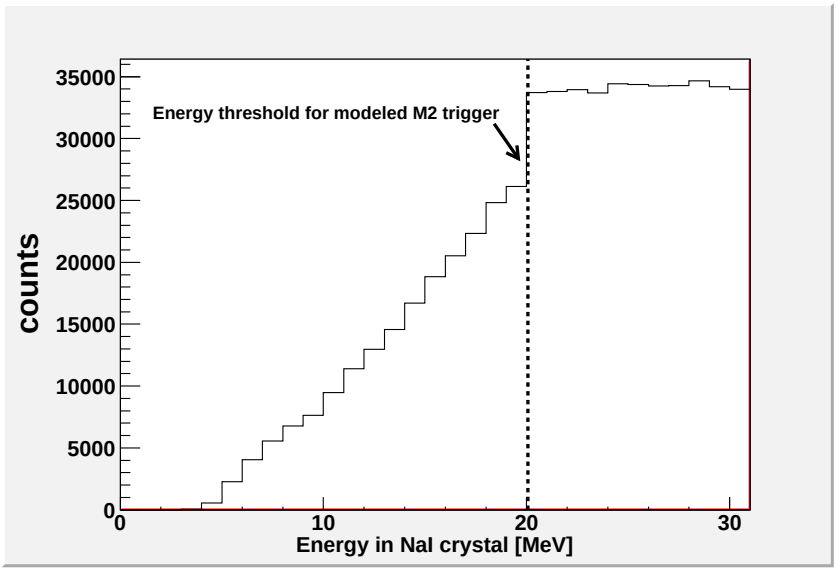

Figure 4.17: *The energy deposited (from the data) in the most energetic CB crystal. The energy threshold for the multiplicity trigger prevented the highest energy crystals having less than approximatively 20 MeV. The simulated trigger used the same value.*

To model the multiplicity trigger for the simulated data, the crystals were split into the same 45 units of 16 as the real detector system. For each event, the crystal with the highest energy deposition in each section was identified. At least two sections had to contain a crystal with the energy above 20 MeV for the event to pass. This condition was applied to the real data as well as to the simulated data.

4.6.2 Crystal Ball energy sum

The energy sum of the crystal ball was formed from the sum of the analog energies of all 672 NaI crystals. Therefore, it was important to have an accurate calibration of the crystal ball allowing to align the gains of all PMTs. A simple cut was set in the analysis: The event is analyzed when the energy sum of all photons from all clusters in the ball is above a certain value (300 MeV).

Chapter 5

Inclusive η production

The aim of the present work is to study the following reactions:

- $\gamma + ^3He \rightarrow \eta$ + N (quasi-free inclusive)
- $\gamma + ^3He \rightarrow \eta + ^3He$ (Coherent production)
- $\gamma + ^3He \rightarrow \pi^0 + p + X$

The η -mesons are identified via: $\eta \rightarrow 2\gamma$ or $\eta \rightarrow 3\pi^0 \rightarrow 6\gamma$ and the π^0 via their $\pi^0 \rightarrow 2\gamma$ decays. The principal difference between the methods to identify the coherent and the quasi-free cross section is the detection of the charged particle. Indeed, the ^{3}He cannot be detected. So, the missing energy (introduced in the next chapter) will be used to identify the coherent channel. This procedure needs a specific analysis.
In the next chapters, we will describe how the different reaction channels have been selected as well as all cuts which were applied to extract the results.

First of all, one has to mention that the extraction of the quasi-free inclusive η reaction is straight forward up to 800 MeV. Above this energy, the cross section will not be extracted in this work, a more specific analysis has to be performed to remove the additional background coming from the production of π-η pairs. The quasi-free inclusive reaction is the most important background channel for the coherent reaction thus it must be well controlled. Moreover, the larger cross section of this channel allows detailed test of the analysis procedures and the results can be compared to the previous experiments.

5.1 Event selection for η production

Only events with two or three hits (the third hit is a nucleon) were selected for $\eta \rightarrow 2\gamma$ and events with six or seven hits (7th is also a nucleon) for $\eta \rightarrow 3\pi^0 \rightarrow 6\gamma$. Then, the η was identified via the invariant mass analysis explained in section 4.5.

5.2 The reaction identification

The η -meson is identified by its 2γ or $3\pi^0$ invariant mass distribution. The invariant masses show a peak at $\pm$ 547.3 MeV typical for the η. The invariant mass and the missing mass are plotted for different energy ranges as shown in Fig. 5.1 and Fig. 5.2. Just above the η threshold the missing mass is clean (second raw). In the studied energy range (600 MeV-810 MeV) no cuts are applied to remove the competing background (η -π pairs). The peaks are not centered around zero in the threshold region due to the asymetric influence of Fermi motion (reactions with beam momentum antiparallel to the momentum of the participant nucleon are enhanced with respect to those with parallel momenta).

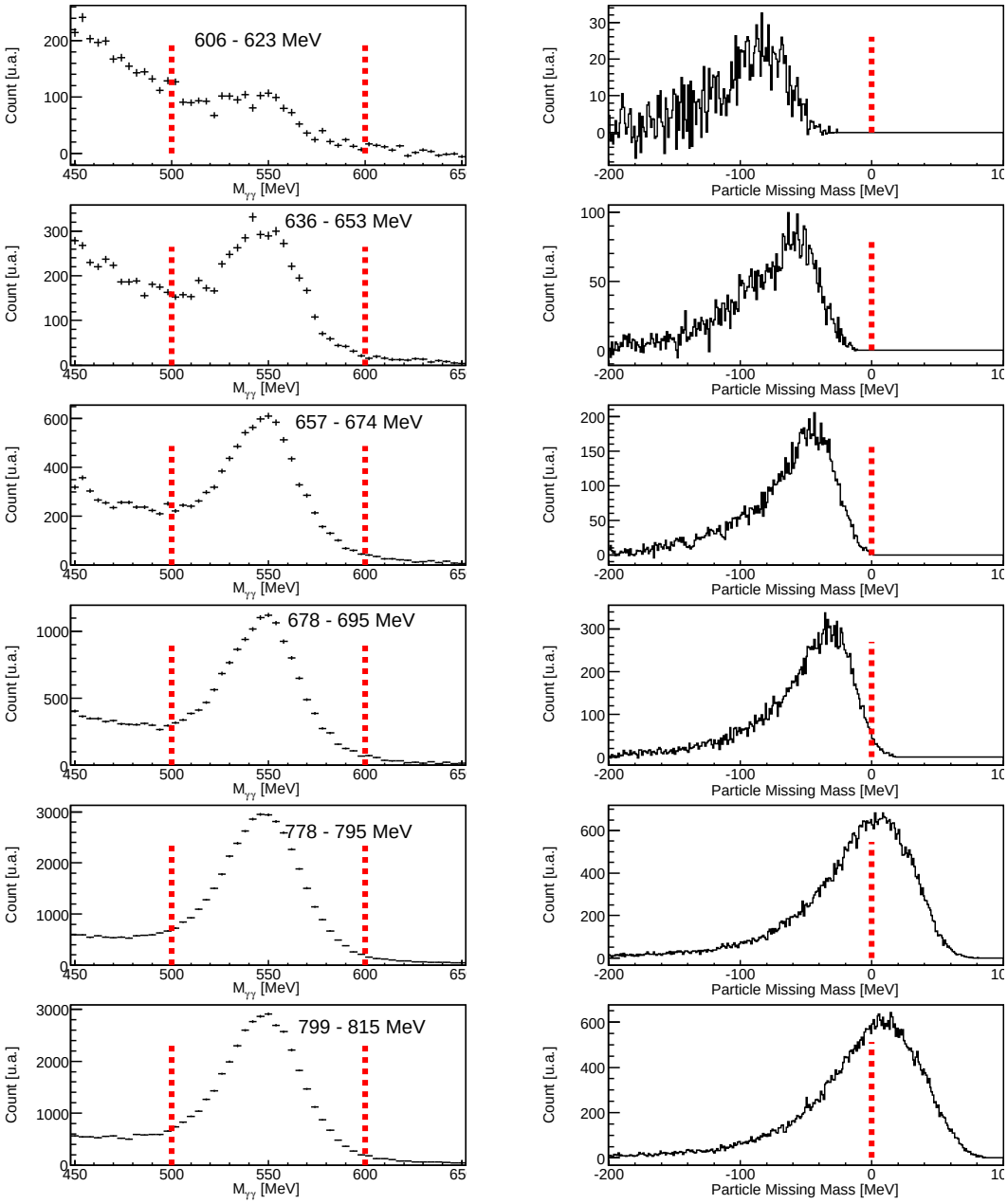

Figure 5.1: *Left column: Invariant mass spectra of $\eta \to 2\gamma$ for different energy bin applied to the data. Right column: Missing mass distribution in quasifree kinematics for the same photon beam ranges.*

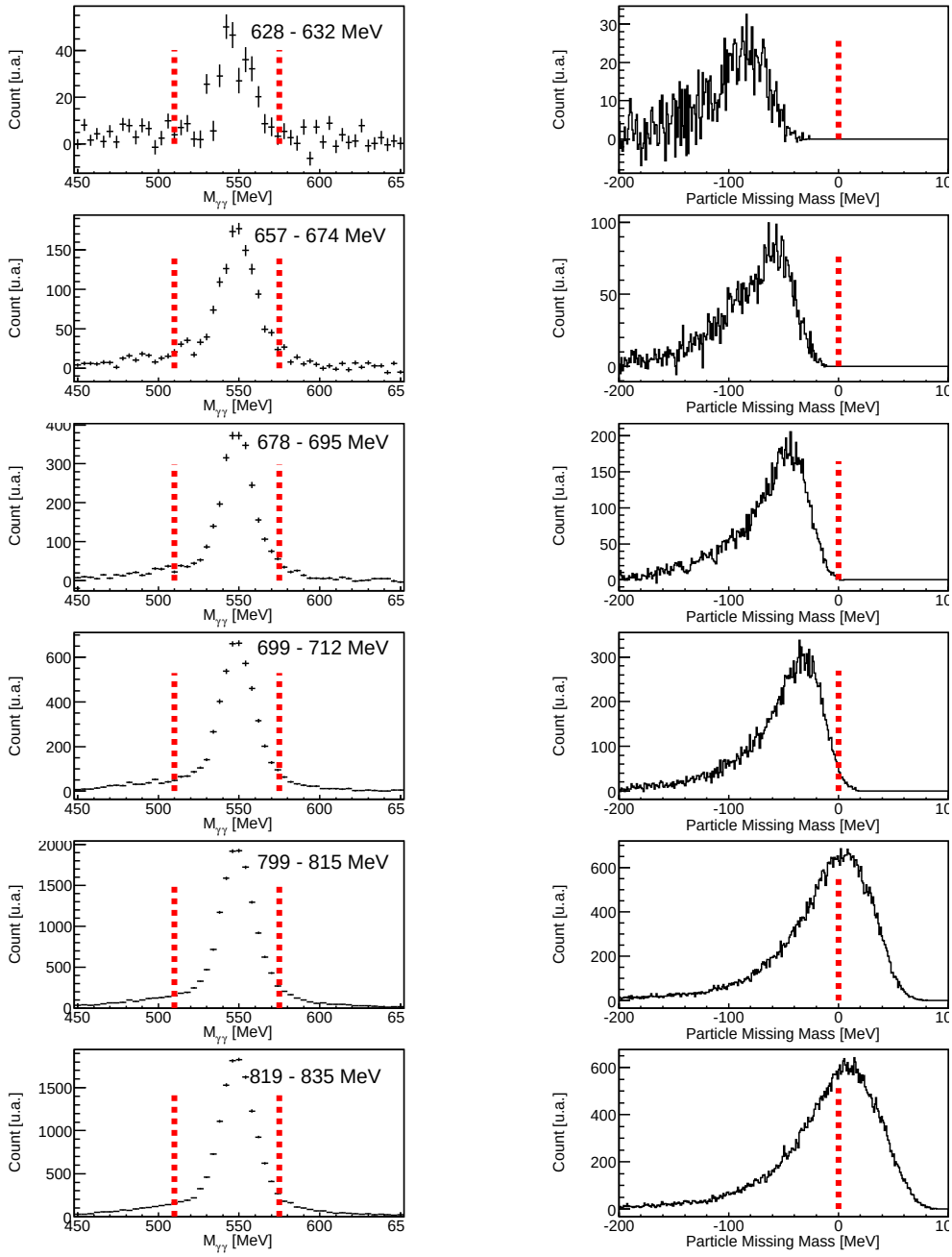

Figure 5.2: *Left column: Invariant mass spectra of $\eta \to 6\gamma$ for different energy bin, the vertical red line represent the cut applied to the data. Right column: Missing mass distribution for the same photon beam ranges. No cut is applied.*

5.3 extraction of the signal for $\eta \to 2\gamma$

In order to extract the signal, the invariant mass of $\gamma\gamma$ is fitted with a Gaussian function plus a polynomial function of third order. In order to minimize the fluctuation, the peak position and the width of the Gaussian has been also fitted using a polynomial of degree 3 (see figure 5.3).

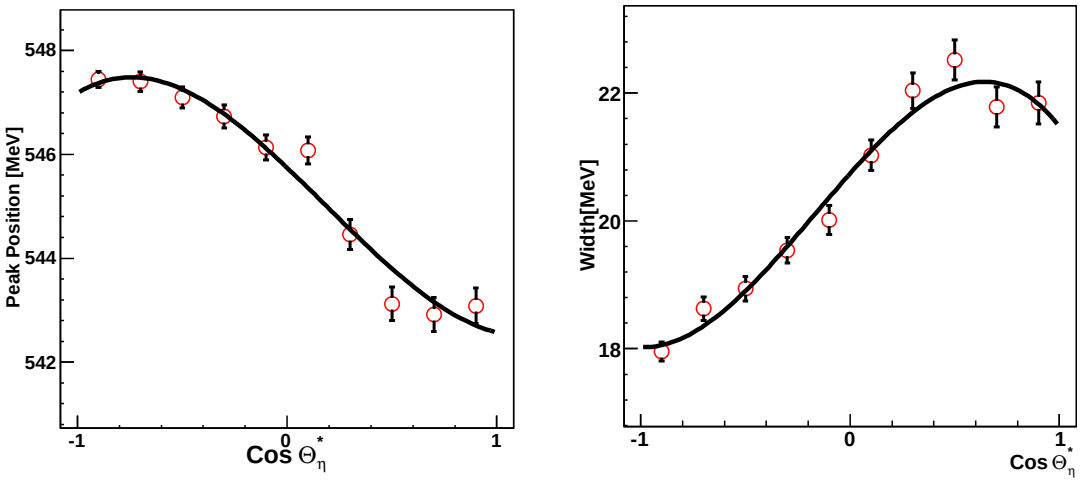

Figure 5.3: *Left: Peak position of the Gaussian fit for different cos θ_η for E_γ = 620 MeV. The black curve is a fit (polynomial function of degree 3). Right: Width of the Gaussian fit for different cos θ_η for E_γ = 620 MeV. The black curve is a fit (polynomial function of degree 3)*

The invariant mass histograms were then refitted using the same Gauss + polynomial of degree 3 function but with fixed parameters extracted from the fit of the Gaussian (position and width). The signal is then obtained by integrating the new Gaussian between 500 MeV and 600 MeV (red curve in figure 5.4). This analysis is done for each energy bin and each angular bin.

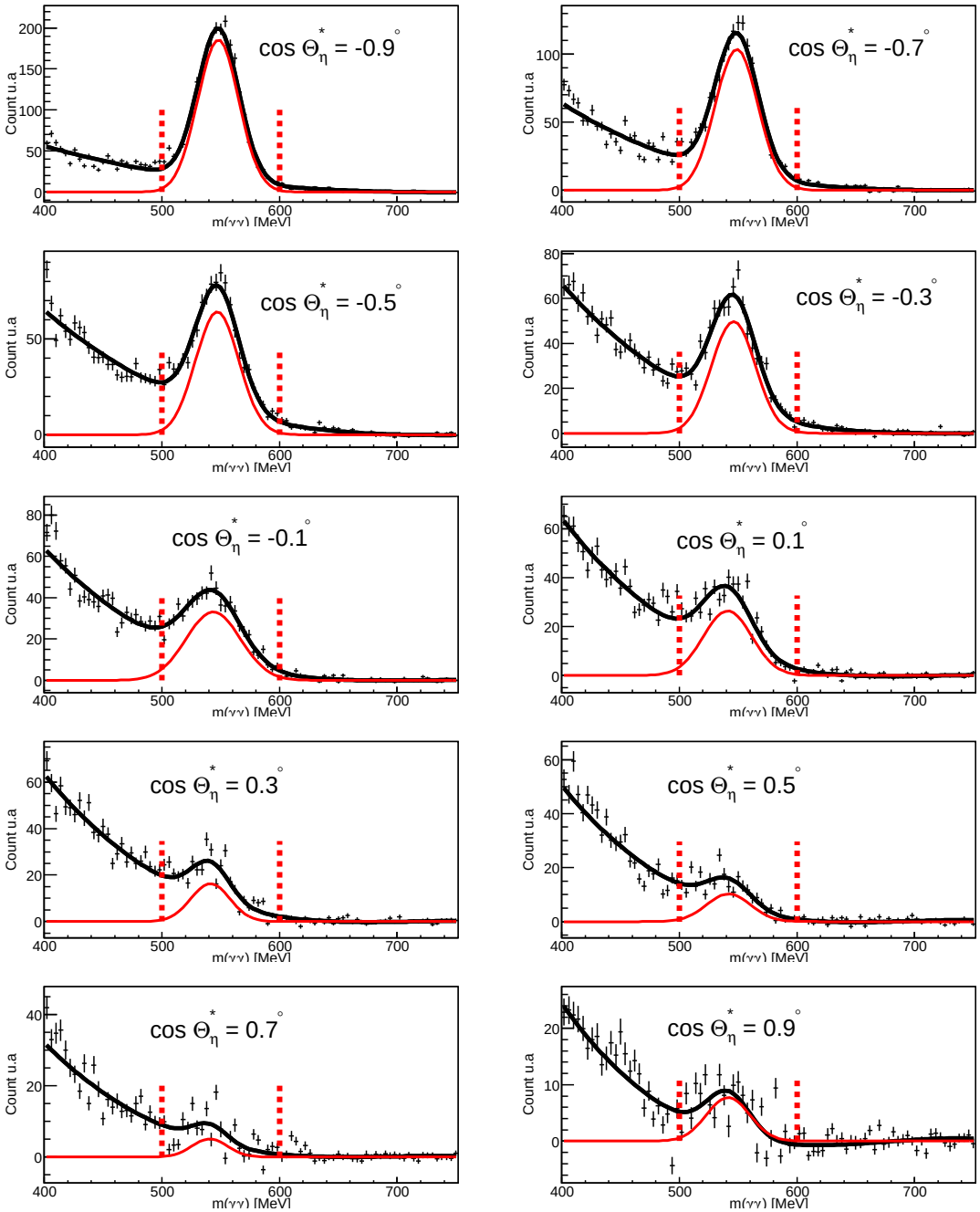

Figure 5.4: *Invariant mass of $\eta \to 2\gamma$ for the energy range between $E_\gamma = 640$ MeV and $E_\gamma = 660$ MeV for each angular bin. The black curve is the fit (Gaussian plus a polynomial function of third order) applied to the data. The red curves is the Gaussian function. The integral between 500 MeV and 600 MeV of the red curve is the numbers of η extracted.*

5.4 Invariant mass cut and extraction of the signal for $\eta \to 6\gamma$

Figure 5.5 shows the invariant mass spectra of $3\pi^0$ for each angular bin in the energy range between 640 MeV and 660 MeV. One can see that the η resonance is background free. This is due to the kinematical constrains (above 760 MeV an additional background appears due to the η -π pairs production and misidentified triple π^0 events). The events will be selected between 510 MeV and 575 MeV. The competitive background starts to appear above 760 MeV, but it is non-negligible above 850 MeV. Fig 5.6 shows the count rate of inclusive η 's for $\eta \to 2\gamma$ (red points) and $\eta \to 6\gamma$ (blue points).

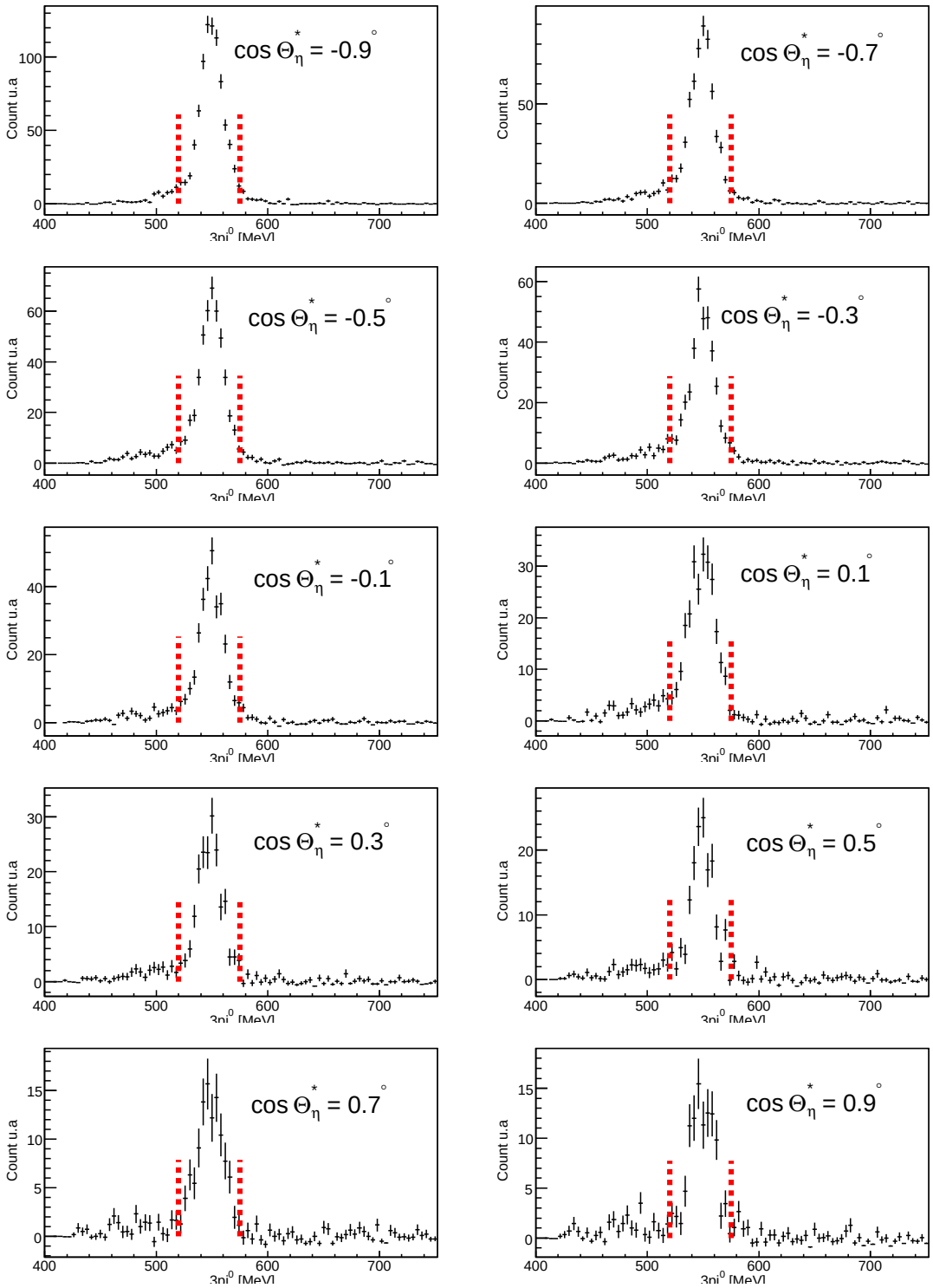

Figure 5.5: *Invariant mass of $3\pi^0$ for the energy range between $E_\gamma = 640$ MeV and $E_\gamma = 660$ MeV. The integral between both red dotted line is the numbers of η extracted.*

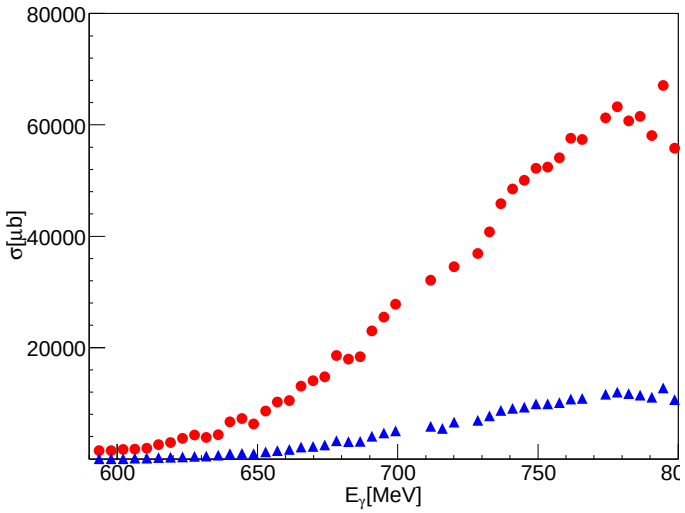

Figure 5.6: *Excitation function of $\eta \to 2\gamma$ (red points) and $\eta \to 6\gamma$ (blue points).*

Chapter 6

Coherent reaction

For the extraction of the coherent cross section, the exclusive detection (where the η is detected in coincidence with the ^{3}He nucleus) would in principle be the easiest way of identification. This would require the detection of the ^{3}He nucleus. However, this is impossible due to the charge of the ^{3}He. The ^{3}He nuclei loose their kinetic energy already when traversing through the target or through other material on the way to the detector. Another method has to be applied. This is the calculation of the so called missing energy.

6.1 Missing energy analysis

The principle of the missing energy analysis is to compare the measured energy of the η meson with the energy calculated assuming coherent production. The comparison is done in the center of momentum frame. E_η^{meas} is calculated. The photon energy E_γ and the energy of the η-meson is given by the experiment:

$$E_\eta^{meas} = \gamma \cdot (E_\eta^{lab} - \vec{p} \cdot \vec{\beta}) = \gamma \cdot (E_\eta^{lab} - p\beta \cdot \cos(\theta_\eta)) \tag{6.1}$$

with $\vec{\beta}$ the velocity:

$$\vec{\beta} = \frac{E_{\gamma \cdot \vec{e}_z}}{E_\gamma + m_{^3He}} \tag{6.2}$$

and γ the Lorentz factor:

$$\gamma = \frac{E_\gamma + m_{^3He}}{\sqrt{s}} \tag{6.3}$$

$\sqrt{s}$ is the energy in the CM:

$$s = 2 \cdot E_\gamma \cdot m_{^3He} + m_{^3He}^2 \tag{6.4}$$

The calculated energy of the ηmeson is:

$$E_{\eta}^{calc} = \frac{s + m_{\eta}^2 - m_{^3He}^2}{2\sqrt{s}} \tag{6.5}$$

The missing energy is given by:

$$E_{miss} = E_{\eta}^{meas} - E_{\eta}^{calc} \tag{6.6}$$

When E_{η}^{meas} is equal to E_{η}^{calc}, the η is produced coherently.

6.2 Background subtraction

Fig 6.3 ($\eta \to 6\gamma$) and 6.2 ($\eta \to 2\gamma$) show missing energy spectra (second raw). A clear peak is observed in the region between the coherent and breakup thresholds. In this range only coherent production of η mesons is possible. However for the decay $\eta \to 2\gamma$ some background is appearing for missing energies above 10 MeV, which is visible also for higher incident photon energies. It is related to background in the invariant mass spectra (see 6.2 left column)
The following sequence is applied to remove this background:

- An invariant mass spectrum is plotted for each missing energy bin
- A Gaussian fit is applied (gauss + polynomial of degree three) (an example of this fit is shown in fig 6.1). The widths and the peak positions are fitted as function of E_{γ}.
- Fitted parameters are used to fit again with a Gaussian
- The count for the missing energy spectra are recalculated by integration of this gaussian

Figure 6.2 (third raw) shows the results of this procedure. The missing energy spectra are now clean. This background was clearly coming from misidentified photons and combinatorial background because is is not visible in figure 6.3. Indeed, $\eta \to 6\gamma$ doesn't need such a procedure because the energy spectra are already clean.

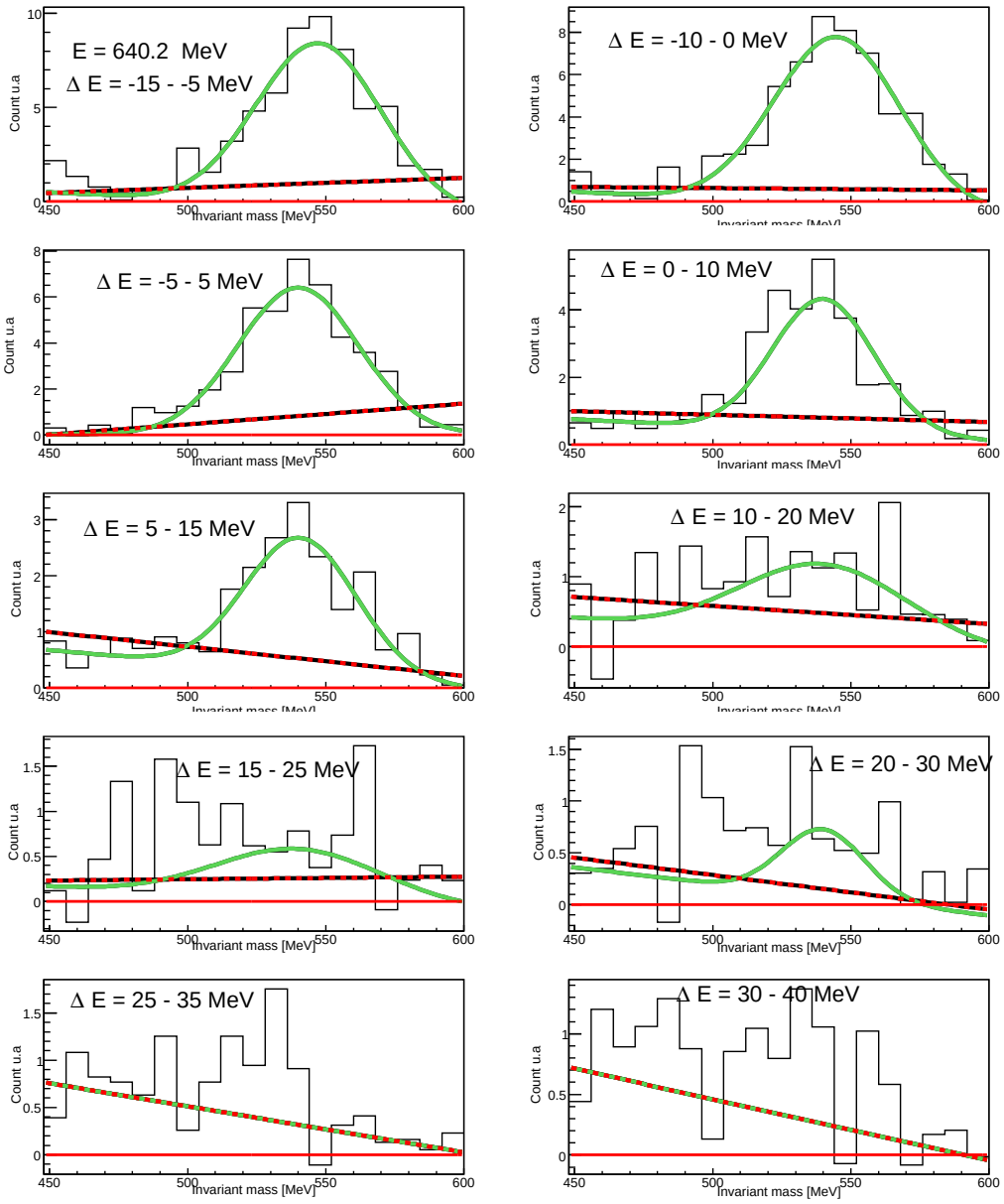

Figure 6.1: *Invariant for different missing energy bin (beam energy : 640 MeV). The red curve is a gaussian plus polynom degree three. The dotted red line is the background fit.*

The quasi free contribution appears above 607 MeV. This contribution will be removed by fitting the simulated missing energy lineshape to the data.

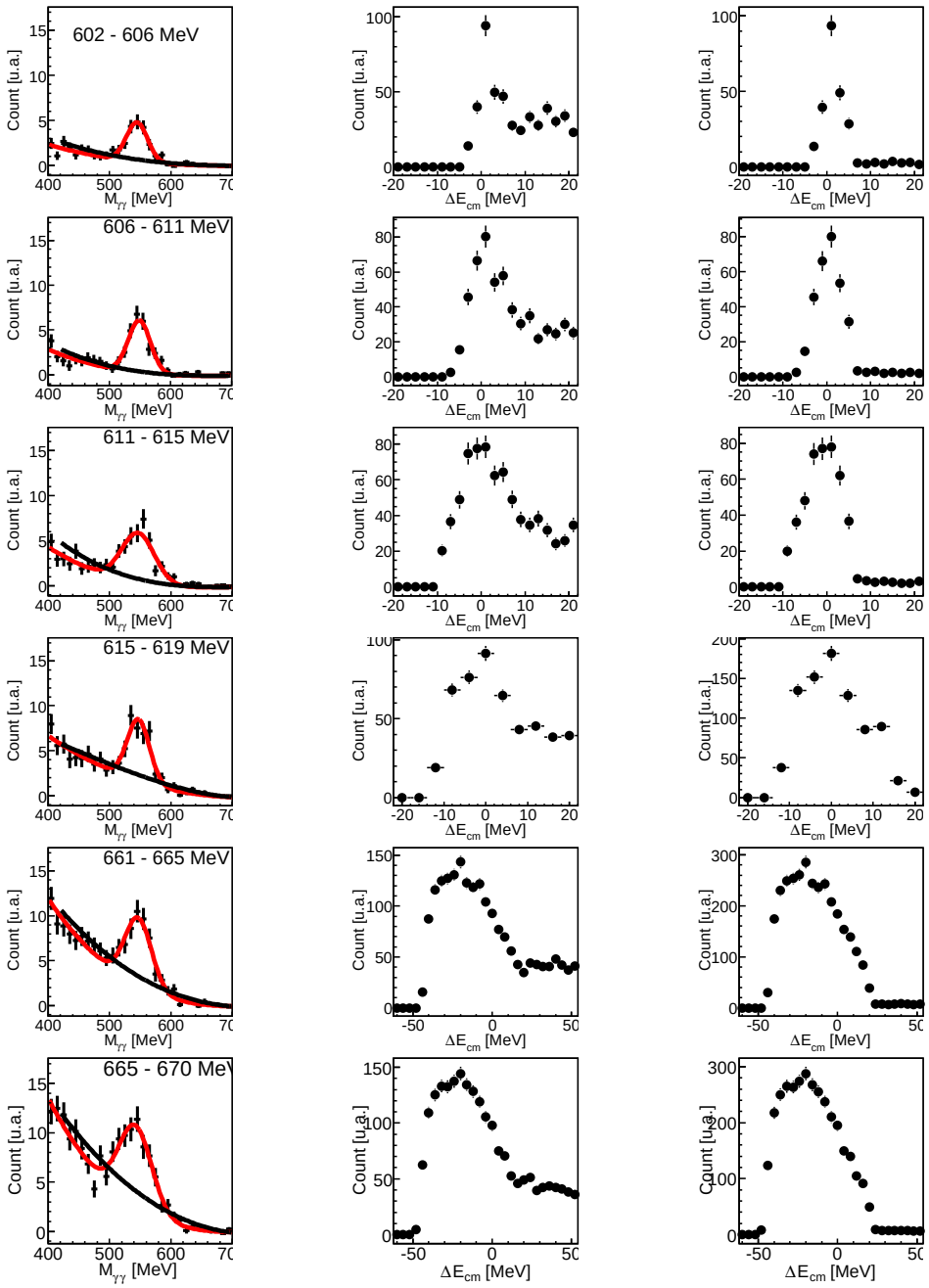

Figure 6.2: *Left: Invariant mass spectra of* $\eta \to 2\gamma$. *Middle: Missing energy spectra before background substraction. Right: Missing energy spectra after background substraction.*

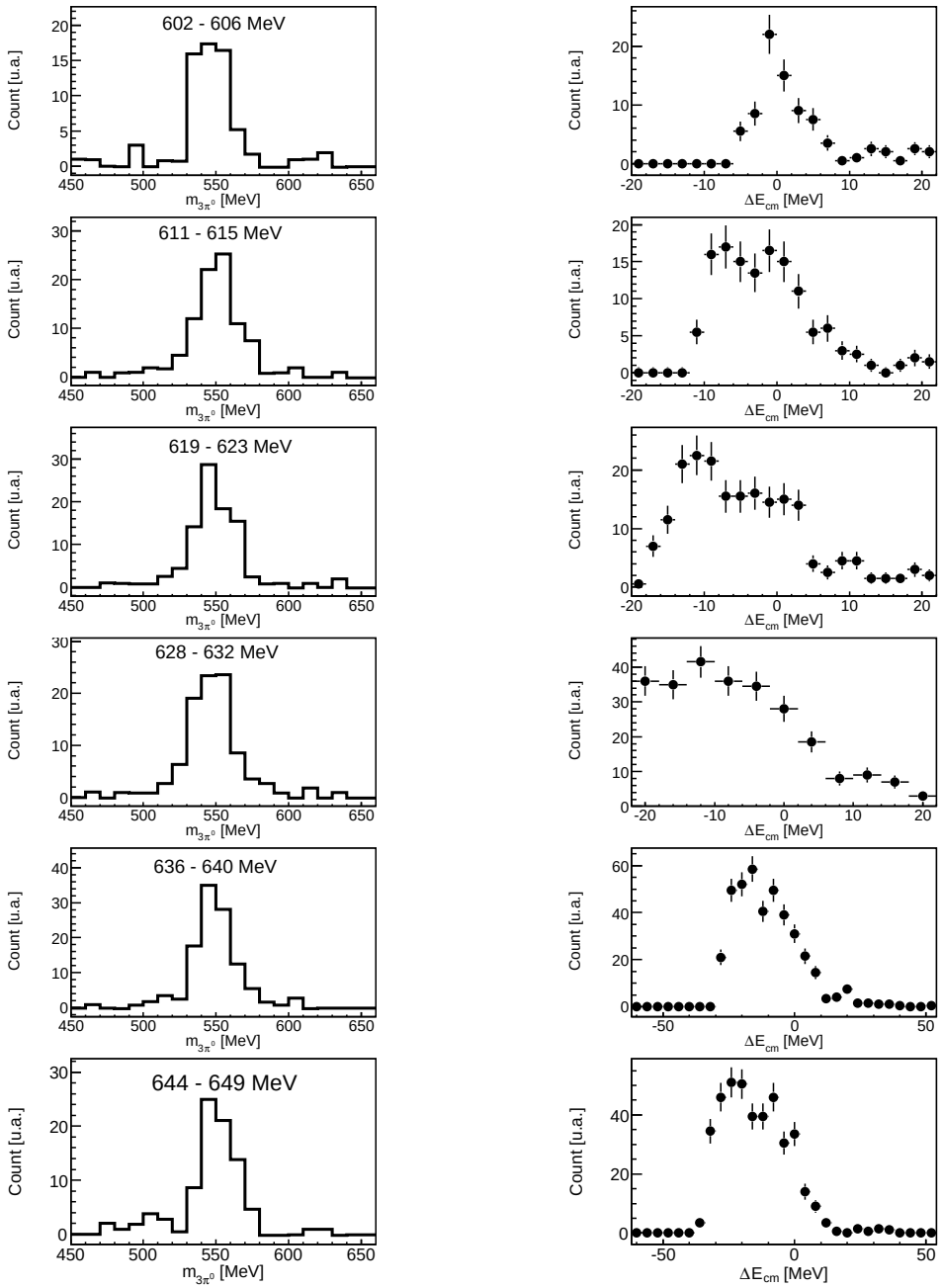

Figure 6.3: *Left: Invariant mass spectra of* $\eta \to 6\gamma$. *Right: Missing energy spectra.*

6.3 Simulation of quasifree (proton, neutron and deuteron) and coherent η production

6.3.1 quasifree simulation

The nucleons bound inside the ^{3}He are moving with the so called Fermi motion. A momentum distribution (or Fermi motion distribution noted $\vec{(p)}_f$) is plotted in fig 6.4. The calculation of $\vec{(p)}_f$ for the ^{3}He nucleus is a function of the density ρ_p and the related Fermi momenta p [38]:

$$\vec{p}_f(p) = p^2 \rho_p(p) \tag{6.7}$$

The Impulse Approximation (IA) was used to simulate the quasi-free photopro-

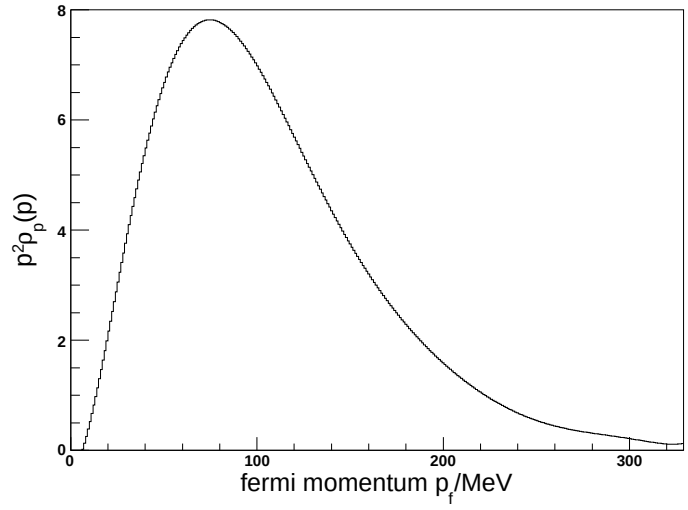

Figure 6.4: Nucleon's Fermi distribution of ^{3}He nucleus with the mean momentum $<\vec{p}_f = 105$ MeV$>$

duction off nucleons and deuterons bound inside the helium nucleus. The IA is an approximation to study the collision of an incident particle with a bound target particle by taking into account the momentum distributions of the bound particles but ignoring interactions with the rest of the nucleus (FSI). The momentum distribution or the Fermi distribution p_f, can be constructed from the Paris [23] or another wave function [2] or in the most simple approximation ignoring the high momentum tail as a normalized Gaussian distribution with proper sigma. In the spectator - participant approach a participant particle (nucleons or deuteron)

with momentum p_f corresponds to a spectator with p_f which becomes on-shell in the the γ^3He reaction. Three different quasi-free contributions need to be distinguished:

- $\gamma + {}^3\mathrm{He} \rightarrow p + \eta + X$ (deuteron as spectator)
- $\gamma + {}^3\mathrm{He} \rightarrow n + \eta + X$ (pp as spectator)
- $\gamma + {}^3\mathrm{He} \rightarrow d + \eta + X$ (p as spectator)

6.3.2 Coherent reaction

The two body kinematics calculation for the η energy is possible in the center of mass frame. The available energy in the cm system, $\sqrt{s}$, is calculated like :

$$\sqrt{s} = \sqrt{2 \cdot E_\gamma \cdot m_{^3He} + m_{^3He}^2} \tag{6.8}$$

Where E_γ is the energy of the incoming photon. The ^{3}He nucleus and the η meson have their momentum and energy calculated in the CM system. The η meson is generated isotropically. Then the cm momenta have to be transfered to the laboratory system.

6.3.3 Fit of the simulated missing energy line shape to the data

The next task is to fit the simulated line shape of the quasi-free and the coherent contributions to the data. This adjustment determines how many coherent events are created. The background coming from the breakup will be removed. The data line shape is parametrized by the function: $f_{data} = ax_{coh} + bx_{qfp} + cx_{qfn} + dx_{qfd}$. The simulated contribution of the coherent and the quasi free simulations of the proton, the neutron and the deuteron (respectively $x_{coh}, x_{qfp}, x_{qfn}, x_{qfd}$) are fitted simultaneously to the data. a, b, c, d are the fitting coefficients.
This adjustment is shown in figure 6.5 and 6.6 (for $\eta \rightarrow 2\gamma$) and 6.7 (for $\eta \rightarrow 6\gamma$) for different photon energies E_γ. The upper left plots for 6.5 and 6.7 show spectra with energies between the coherent and the quasi-free threshold. In these plots, only coherent η production is energetically possible. Therefore, no quasifree contribution is seen and the coherent contribution is identical to the sum of both. With increasing photon energies the quasifree contribution becomes

more and more dominant. The distribution compares well with the measured data, and the adjustment of coherent and quasifree simulations seems to work up to energies of about 699 MeV. Up to this energy, the fraction of coherent η production can be extracted quite reliably.

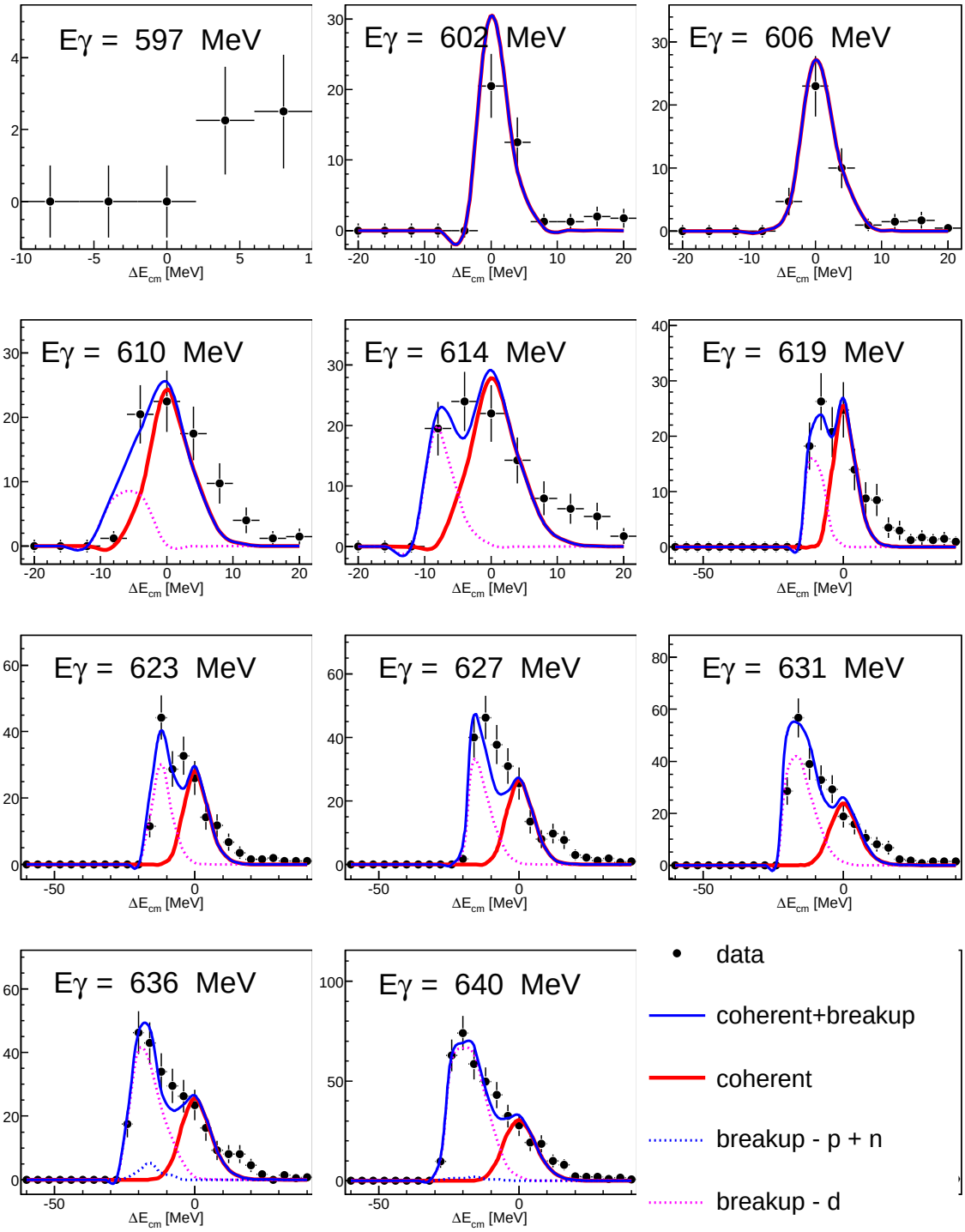

Figure 6.5: *Missing energy spectra for $\eta \rightarrow 2\gamma$ (after background correction)assuming coherent and quasi-free kinematics in different regimes of the incoming photon beam (cut on the invariant mass between 500 MeV and 600 MeV). The simulation of the coherent reaction (red), the quasi free (proton and neutron) reaction (blue) and quasi free on deuteron (pink) are adjusted to fit the data. The solid blue line shows the sum of the simulations. At threshold (between 600 MeV and 607 MeV), the η production proceeds exclusively via the coherent process.*

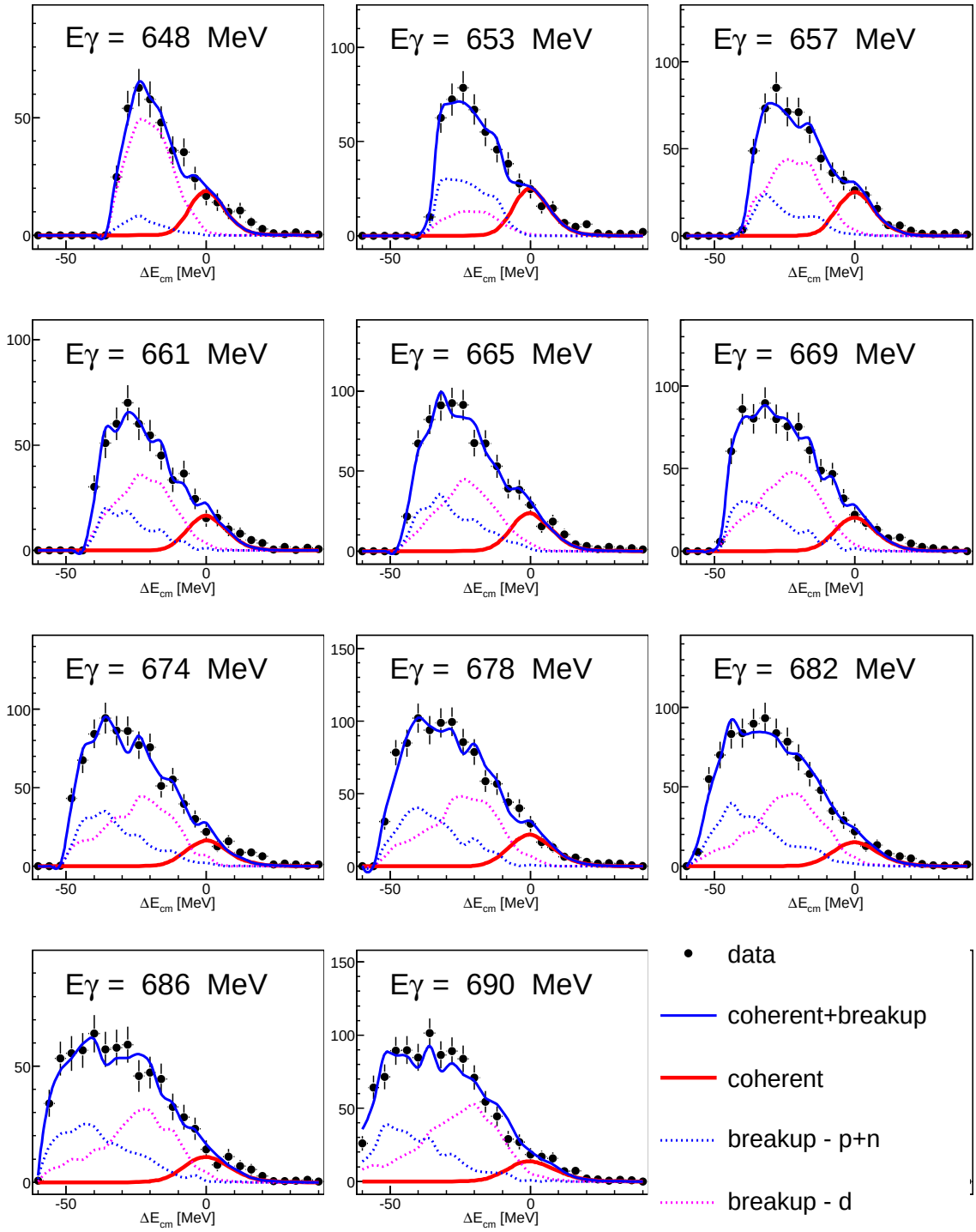

Figure 6.6: *Missing energy spectra for $\eta \to 2\gamma$ (after background correction)assuming coherent and quasi-free kinematics at higher energies (cut on the invariant mass between 520 MeV and 585 MeV). For photon energy above 699 MeV the adjustment of simulations and data is no long possible because the coherent process does not contribute anymore.*

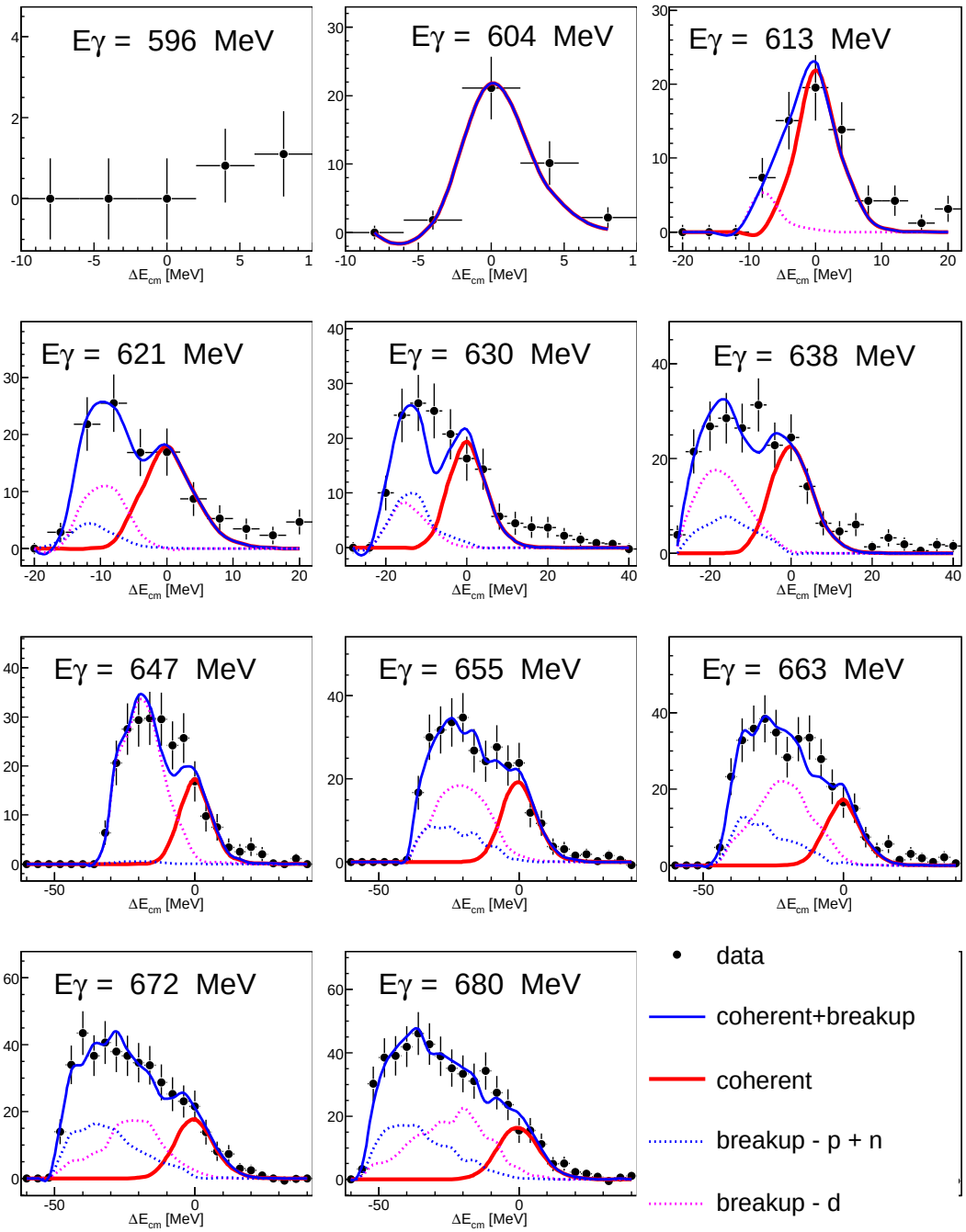

Figure 6.7: *Missing energy spectra for* $\eta \to 3\pi^0$ *assuming coherent and quasi-free kinematics.*

Extraction of the signal for both η decays

The integral of the coherent simulation (normalized to the experimental data) are assumed to be the signal of the coherent channel. Fig 6.8 (left) shows the excitation functions of the $\eta \to 2\gamma$ and the $\eta \to 6\gamma$ decay channels. The points are the integral of the red curves in figures 6.5 and 6.6.

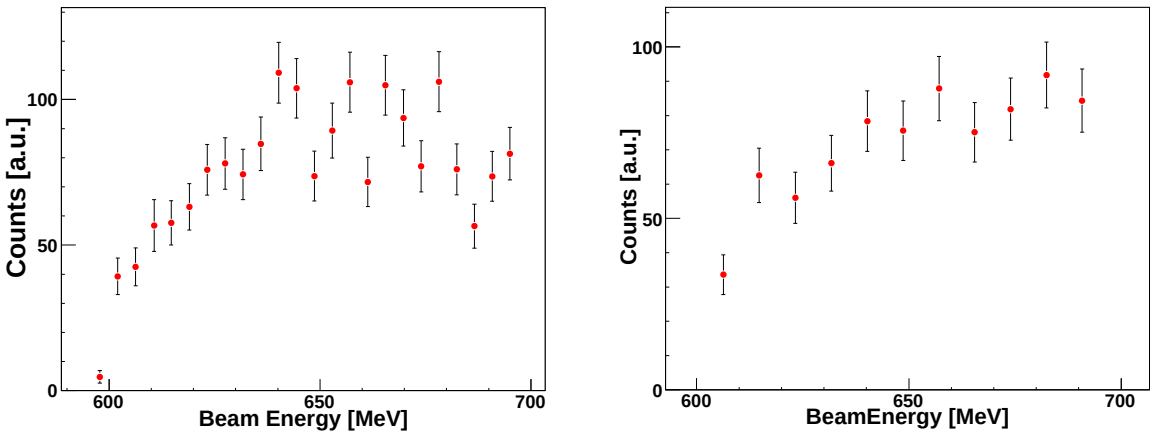

Figure 6.8: η excitation function, the points are the integral of the red curve from figure 6.5 and 6.7 Left: $\eta \to 2\gamma$ Right: $\eta \to 6\gamma$

Extraction of the signal for both η decay (angular distribution)

The coherent η signal has been extracted for each tagger channel and each bin of cos θ where θ is the angle of the η in the center of momentum of (γ, ^{3}He). Fig 6.9 and Fig 6.10 (for $\eta \to 2\gamma$) show the missing energy spectra for different photon energies E_γ and cos θ and Fig 6.11 and Fig 6.12 show the same picture for $\eta \to 6\gamma$. The coherent signal was then obtained by integrating the coherent contribution.
The count rate of η coherent events has been extracted in this part. In the next chapter the different parameter used to normalise the excitation functions will be explained.

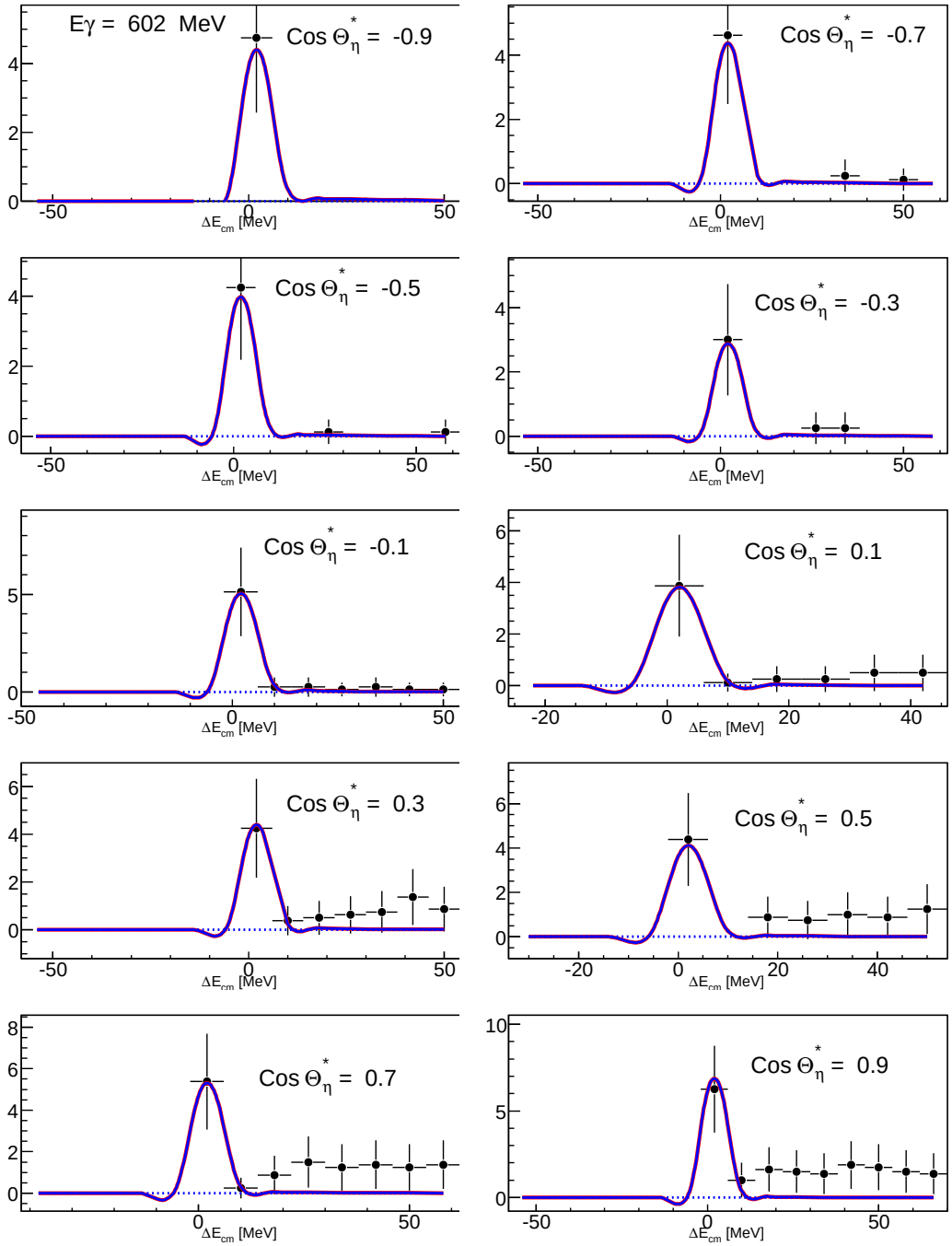

Figure 6.9: *Missing energy spectra for $\eta \to 2\gamma$ assuming coherent (red curve)and quasi-free kinematics (dasehd blue curve) for each angle bin at $E_\gamma = 602$ MeV. The integral of the red curve is the count rate of coherent event.*

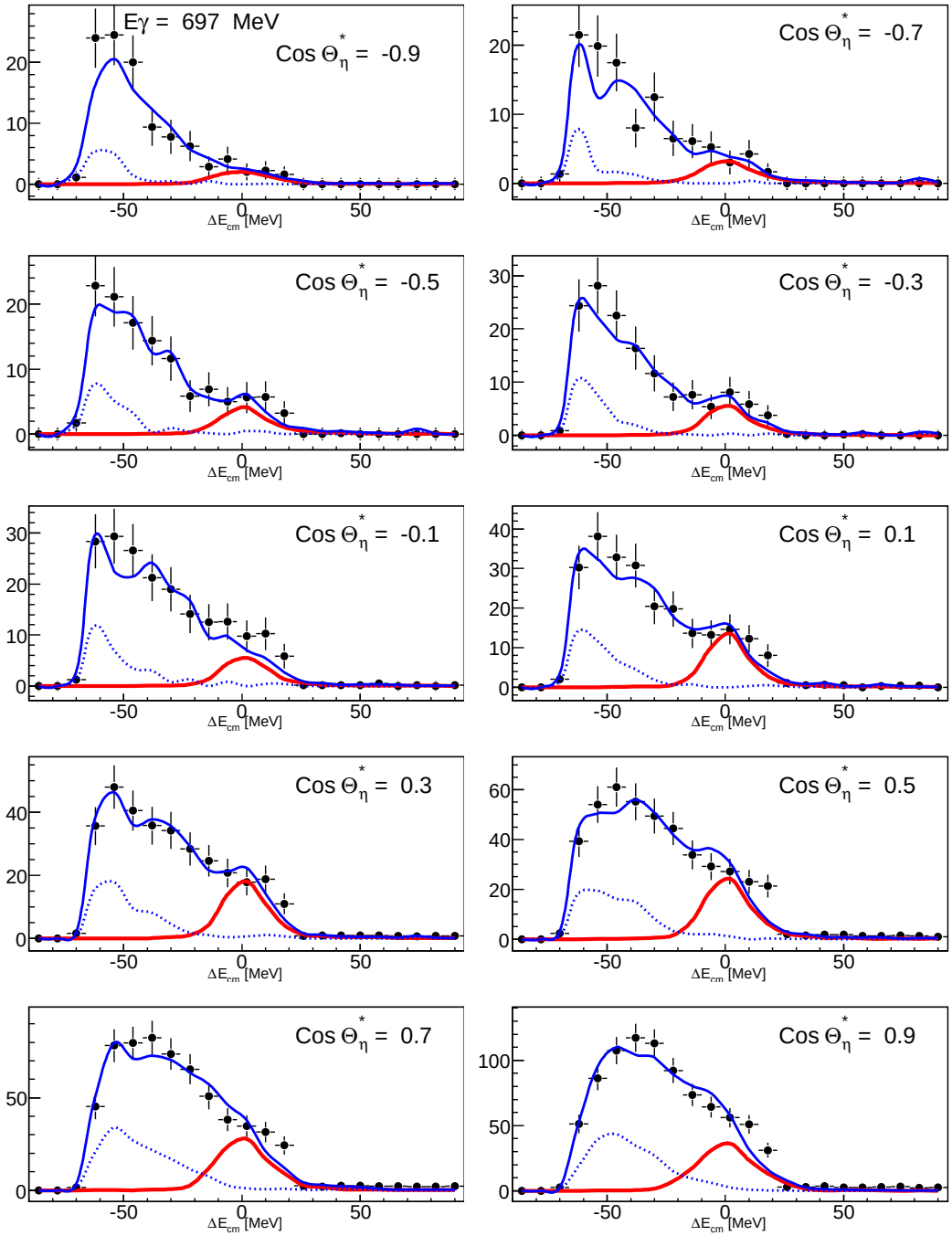

Figure 6.10: *Missing energy spectra for $\eta \rightarrow 2\gamma$ assuming coherent (red curve)and quasi-free kinematics (dasehd blue curve) for each angle bin at E_γ = 699 MeV. The integral of the red curve is the count rate of coherent event.*

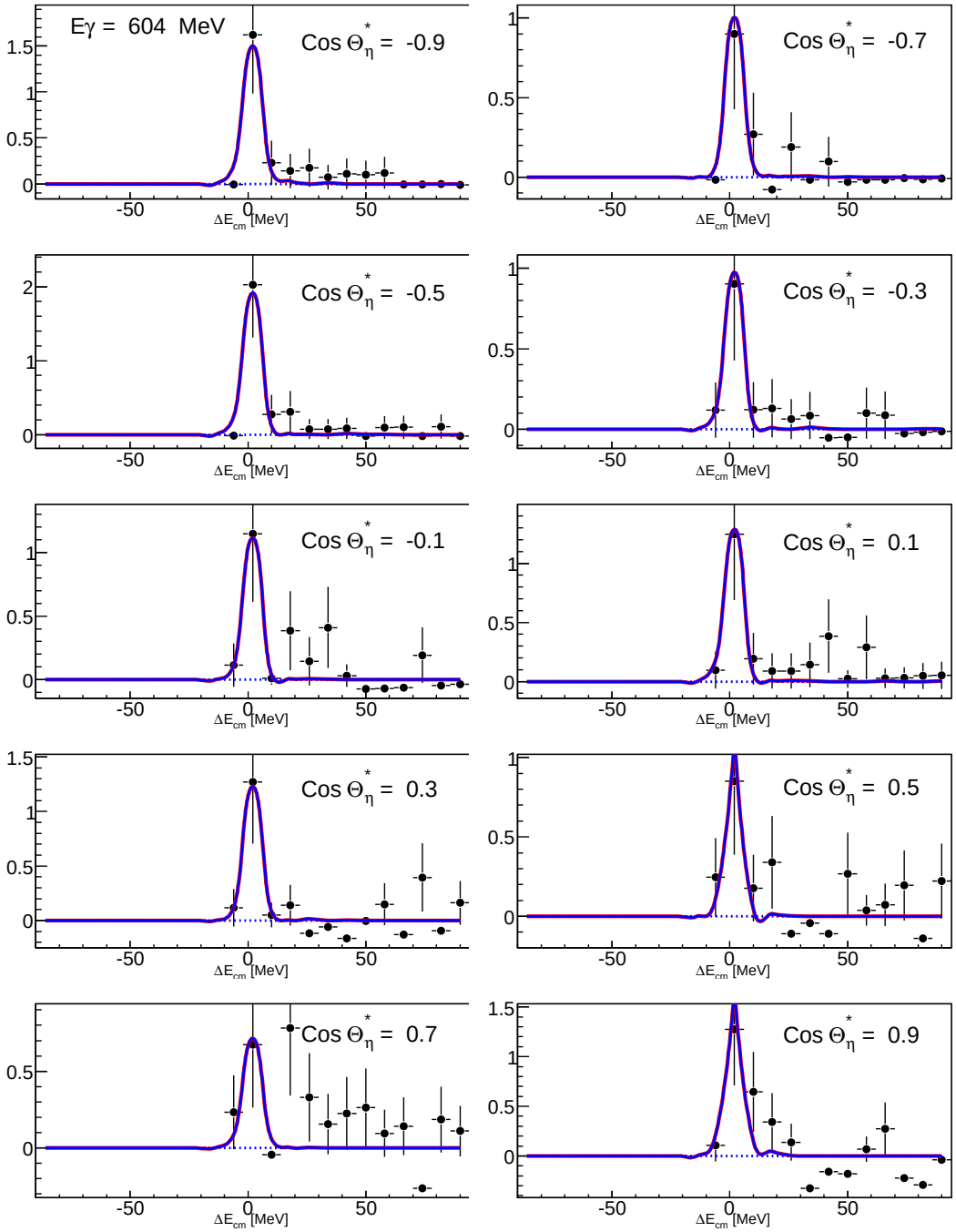

Figure 6.11: *Missing energy spectra for $\eta \rightarrow 6\gamma$ assuming coherent (red curve)and quasi-free kinematics (dasehd blue curve) for each angle bin at E_γ = 604 MeV. The integral of the red curve is the count rate of coherent event.*

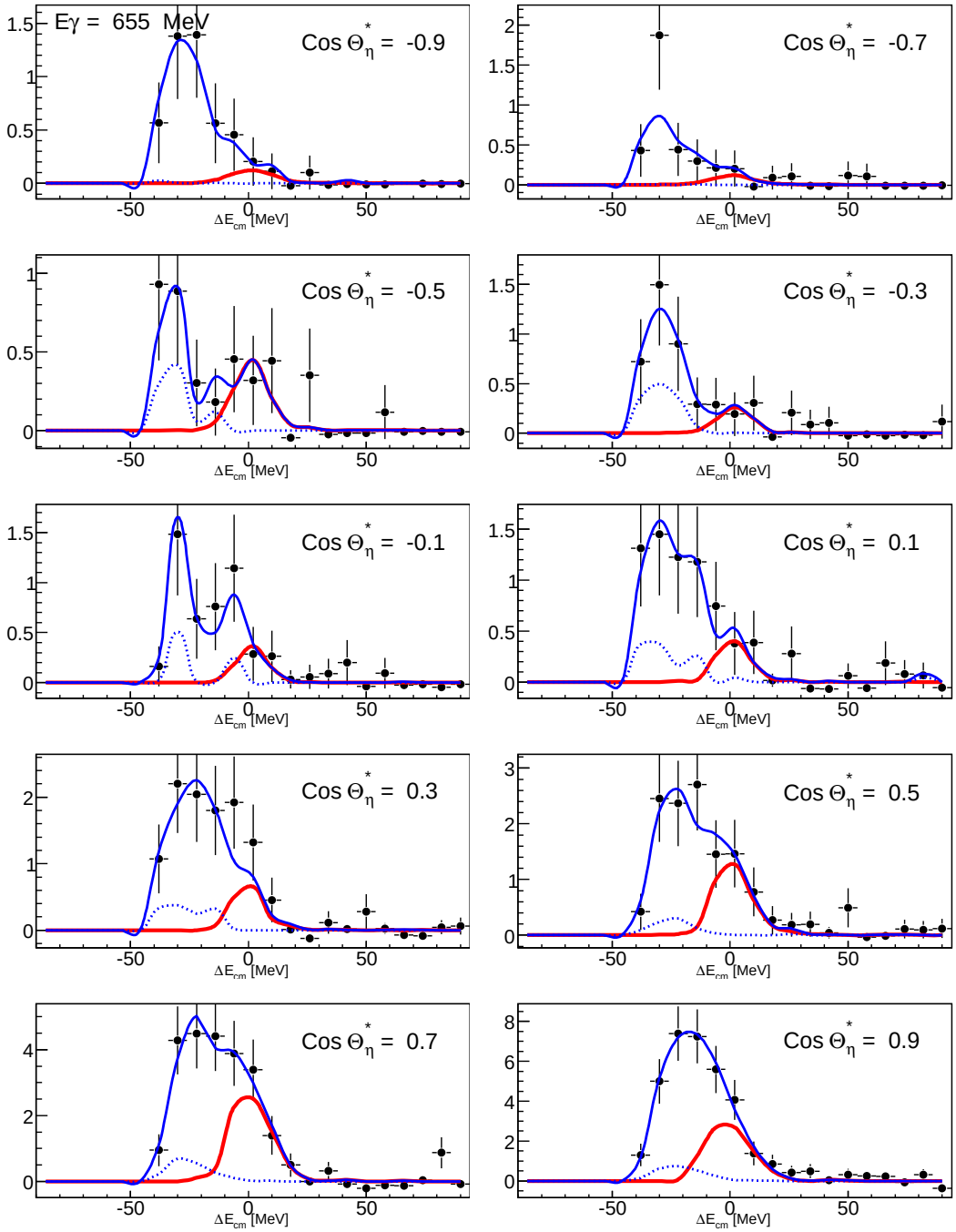

Figure 6.12: *Missing energy spectra for $\eta \rightarrow 6\gamma$ assuming coherent (red curve)and quasi-free kinematics (dasehd blue curve) for each angle bin at E_γ = 683 MeV. The integral of the red curve is the count rate of coherent event.*

Chapter 7

π^0-proton channel

There are two coherent reactions: one elastic (seen in 9.2.2) and one inelastic discussed in the present part. This inelastic channel is useful to define the sign of the imaginary part of the scattering length (the elastic channel gives the value of the real part.) The reaction: $\gamma +^3 He \rightarrow^3 He_\eta \rightarrow \pi^0 + p + X$ with the π^0 and the proton emitted in back-to-back is investigated. The π^0 is identified by the invariant mass analysis described in section 4.5. The desired channel has two principal background contributions:

- The double π^0production
- The quasifree production of π^0-proton pairs

7.1 double π^0 production

The main background channel for the single π^0 final state is the double pion production. In this work, the configuration of the experimental set-up allows us to eliminate this background in a proper way. The 4π trigger allows us to choose only the cases with 2 neutral particles and one charged hit. The missing mass of the deuteron γ + ^{3}He $\rightarrow \pi^0$+ p + d shows a sharp peak at 0 MeV as seen in Fig 7.1. The four-vector's missing mass is calculated from the incident photon beam energy and the reconstructed meson according to the formula :

$$(E_N, \vec{(p)}_N) = (E_\gamma, \vec{(p)}_\gamma) - (E_m, \vec{(p)}_m) \tag{7.1}$$

with E_N the missing proton energy, E_γ the energy of the incoming photon, E_m the energy of the produced meson and $\vec{(p)}_N$ the missing nucleon momentum, $\vec{(p)}_\gamma$ the incoming photon momentum and $\vec{(p)}_m$ for the meson momentum. The energy and momentum of the missing nucleon is then given by:

$$E_N = E_\gamma + m_N - E_m \tag{7.2}$$

$$\vec{p}_N = \vec{p}_\gamma - \vec{p}_m \tag{7.3}$$

So, the missing mass of the deuteron becomes:

$$m_N = \sqrt{(E_\gamma + m_N - E_m)^2 - (\vec{p}_\gamma - \vec{p}_m)^2} \tag{7.4}$$

Fig. 7.1 shows the distribution of the missing masses for different energies of the incident photon beam. A cut between -50 MeV and 50 MeV is applied to select only events with a proton. The proton is reconstructed via the kinematic of the reaction. This is a good approximation.

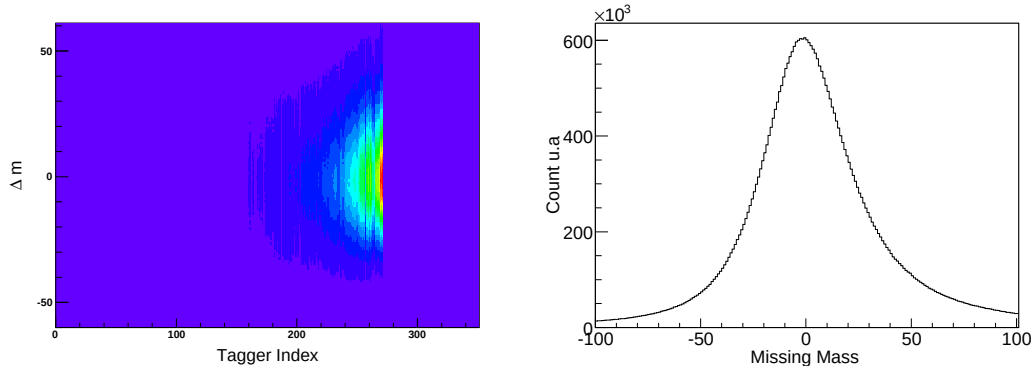

Figure 7.1: *Missing mass spectra for π^0-proton production off ^{3}He. Left: The missing mass remains the same for all incoming photon energies. Right: The event are selected when the missing mass is between -50 MeV and 50 MeV.*

7.2 quasifree production of π^0-proton

One has to understand the kinematic of the dominating quasifree π^0-p background. The simulation is used to understand the kinematic of the quasifree π^0-p background. The incoming photon interacts with the nucleon producing a resonance (show in fig 1.6) which decays into a meson and a nucleon. Fig 7.2 (left) shows the momentum of the resulting π^0 in the center of momentum and (right)

the proton kinetic energy in the laboratory frame when the particles are coming from a quasifree reaction.

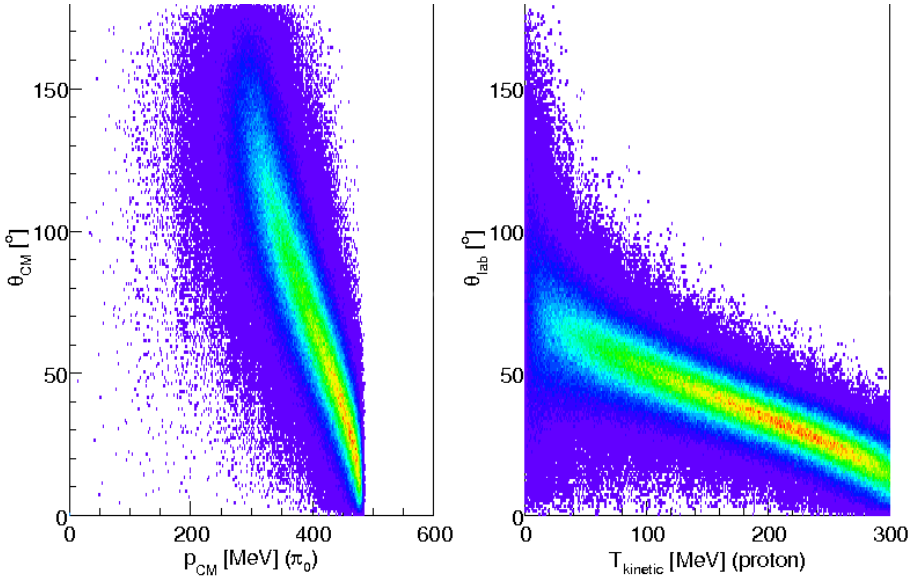

Figure 7.2: *Kinematic of $\pi^0$and proton decays from the quasifree reaction. Left: π^0 momentum in CM, Right: energy kinetic of proton in the lab system.*

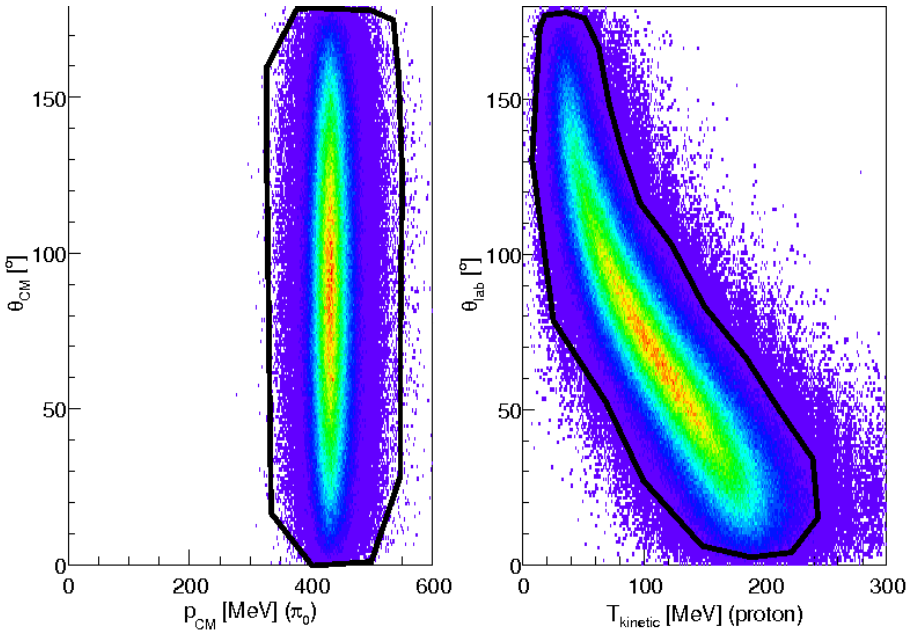

Figure 7.3: *Kinematic of $\pi^0$and proton decays from an η bound state. Left: π^0 momentum in CM, Right: energy kinetic of proton in the lab system.*

The entry channel of the reaction is the production of a coherent η off the ^{3}He implemented in the generator code. The produced η are isotropic in the center of momentum of γ^3He .
After the η binds to the nucleus, a nucleon (only a proton in the simulation) interacts with the bound η and creates a S_{11} resonance. The final state is a π^0 and a proton resulting from the decay of the S_{11} resonance. Fig 7.3 (left) shows the momentum of the resulting π^0 in the center of momentum and (right) the proton kinetic energy in the laboratory frame. The cuts indicated in black will be applied in the analysis in order to isolate only the π^0-p decays coming from a bound state. The pictures 7.3 and 7.2 emphasize how much the two kinematics γ + ^{3}He $\rightarrow^3$He $_\eta \rightarrow \pi^0$+ p + X and γ + ^{3}He $\xrightarrow{S_{11}} \pi^0$+ p + d are different.

7.3 Back-to-back emission in the π^0-p channel

Even if we apply the anti-quasi free cut described above, we still have a contribution coming from this competing channel. One has to optimize the angular range where one can observe the bound state. For this task, the comparison between the opening angles of π^0-p pairs coming from the bound state and the classical quasifree reaction is necessary. Fig 7.4 shows the two simulated distributions.

The simulation shows that the signal corresponding to opening angles between 165° and 180° is isolated. So, this optimzed cut will be use to isolate the π^0-proton event in back-to-back emission coming from a bound state decay.

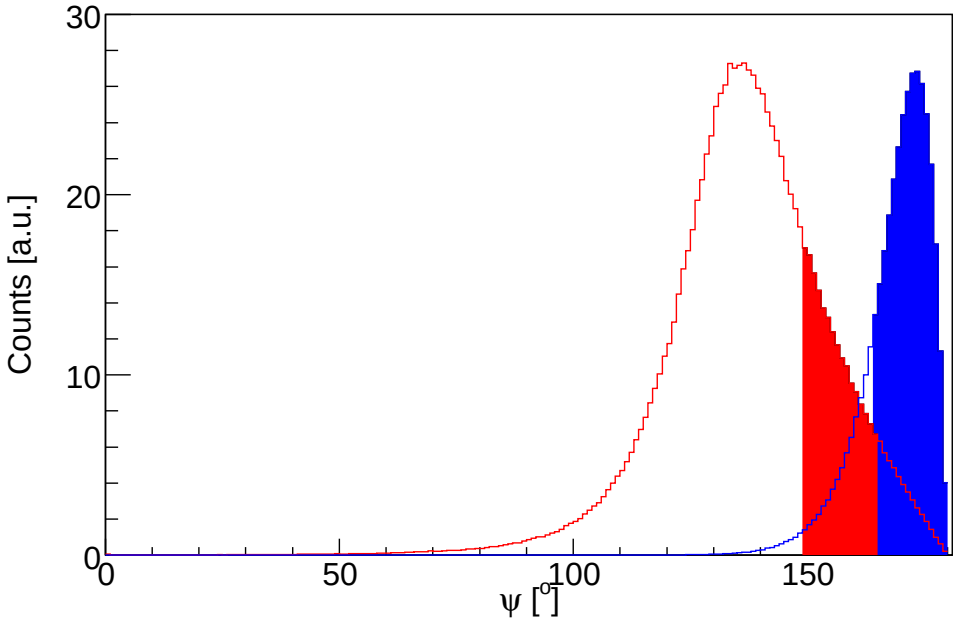

Figure 7.4: *Calculation for the distribution of the opening angle of π^0 and proton in the γ-^3He system for events decaying back-to-back in the S_{11} rest frame, blue is coming from η bound state and is generation in case of quasifree reaction. Blue and red zone are the optimized angle cut.*

Chapter 8

Absolute cross section normalization

The cross section is given by the formula:

$$\sigma = \frac{N_X}{N_{e^-}\epsilon_{tagg}\epsilon_{det}N_{target}\Gamma_{X\to Y}} \tag{8.1}$$

Where N_X is the absolute number of reconstructed events given by the previous chapter and the denominator factors allow the normalization of σ to the conditions of the experiment. They are accounted for in this chapter:

- N_{e^-} is the number of electrons measured by the tagger
- ϵ_{tagg} is the tagging efficiency therefore $N_{e^-}\epsilon_{tagg}$ corresponds to the photon flux impinging on the target, see section 8.1.1
- ϵ_{det} is the overall detector efficiency, see section 8.2.1
- N_{target} is the number of target nuclei see section 3.3
- $\Gamma_{X\to Y}$ the branching ratio of the studied channel into the measured decay products, provided by table 1.5

8.1 The photon flux

8.1.1 Tagging efficiency: $\epsilon(E_\gamma)$

In order to determine normalized cross sections, one needs to know the number of photons impinging on the target. In our case, the number of photons reaching

the target should, in the ideal case, be equal to the number of scattered electrons detected in the tagger. As some photons get lost on their way from the radiator to the target, mostly due to collimation, it is useful to define the tagging efficiency as the probability for a bremsstrahlung photon to reach the target:

$$\epsilon_{tagg} = \frac{N_\gamma}{N_{e^-}} \tag{8.2}$$

The tagging efficiency was estimated approximatively on a daily basis with a dedicated measurement. N_{e^-} was determined for each channel using the ladder scaler. The number of photons reaching the target was determined with a special Čerenkov Pb glass detector, large and thick enough ($>$ 20 X_0) to avoid that photons escape, placed in the beam line and used as the stop signal for the tagger TDCs. The tagging efficiency measurements were performed with a beam intensity low enough for the Pb glass not to saturate. Using such a low intensity, the random background in the ladder is negligible and each detected photon can be associated with an electron in the tagger without ambiguity. Before and after each tagging efficiency measurement, the background activity was recorded for ten minutes without any beam. Combining all this, the tagging efficiency is computed channel wise using:

$$\epsilon_{tagg} = \frac{N_\gamma[i]}{N_{e^-}[i] - \frac{t}{t_{back}} N_{e^-}^{back}[i]} \tag{8.3}$$

were t_x is the duration of the tagging efficiency measurements and i runs over all tagger channels. When measuring tagging efficiency after long production runs, the background activity was noticeably higher, coming back to a constant value after $\sim$ 5 minutes. For this reason, only background data taken after each tagging efficiency measurement were used to determine ϵ_{tagg}.

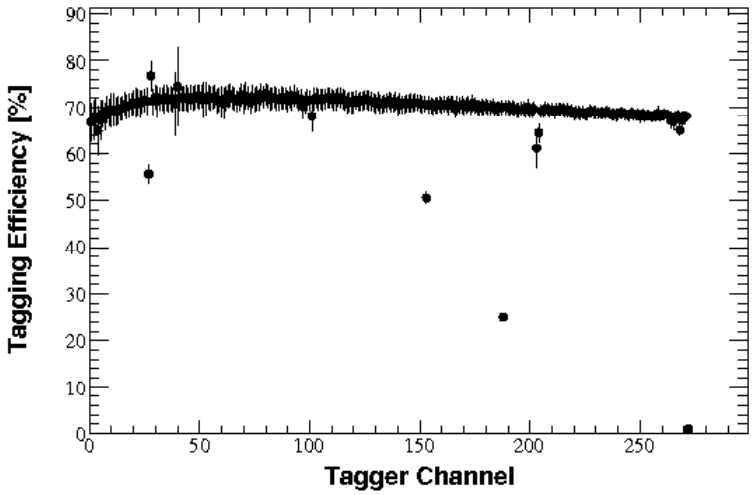

Figure 8.1: *The tagging efficiency as a function of the tagger channel*

Fig 8.1 shows the tagging efficiency for one sample file. Altogether, the tagging efficiency was measured 14 times during the complete experiment. As the conditions might change during data taking the evolution of the tagging efficiency in time has to be taken into account. This is simplified by the fact that the shape of the tagging efficiency as a function of the energy is very stable. Only the absolute value has to be cared of. Still, the tagging efficiency was only measured periodically, approximatively once a day. This leaves room for fluctuations between two consecutive determinations.

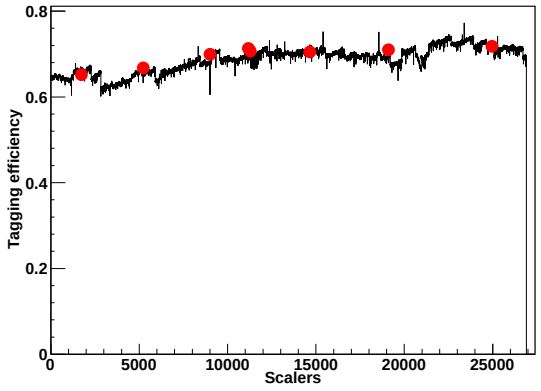

Figure 8.2: *Averaging of tagging efficiency. The ratio P2/Tagger (black line) is compared to the individual measurements (red dots)*

To account for this, an ionization chamber, called P2- was placed behind the target to measure the beam intensity. During the run, the ratio between the counting rates in P2 and in the tagger was continuously monitored. This P2 tagger ratio is proportional to ϵ_{tagg}. As shown in fig 8.2, it is scaled to match the individual tagging efficiency measurements and then integrated over the whole time range. Than the result of this integration is used to correct the average value from 8.1. It can be however noticed that this P2/tagger ratio is very stable so that the correction to apply always remains below 5%. Figure 8.3 shows a typical scaler spectrum.

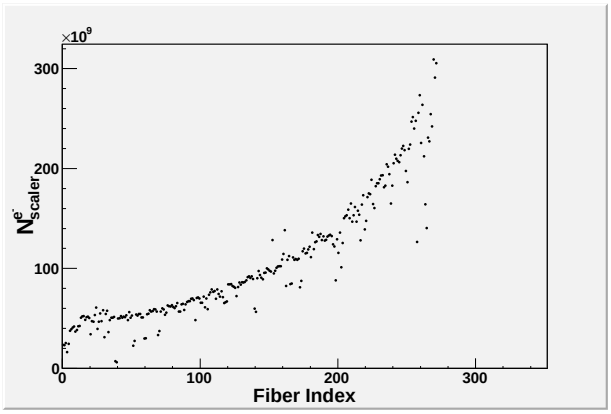

Figure 8.3: *Scaler spectra*

8.2 Simulation and detection efficiency

As mentioned in the previous chapter, our detector has been designed to provide a complete 4π solid angle coverage so that each single event gets observed. Reality is of course different compared to the ideal case and, for different reasons, some events are not detected. A final state particle might get lost, in most cases due to its low energy, below the detectors thresholds. It might also be that a particle escapes through the forward or backward beam holes in TAPS and the Crystal Ball. An event will also be rejected if it does not fulfill the trigger conditions, the number of detected events won't be equal to the number of events actually produced in the target. In order to calculate fully normalized cross sections (for the inclusive and the coherent channel), it is important to evaluate this event losses. This is the so-called detection efficiency.

8.2.1 The detection efficiency ϵ_{det}

Knowing the performances of a detector is a recurrent concern to every physical experiment involving the detection of particles. The GEANT (GEometry ANd Tracking) toolkit was developed early in CERN history to allow a precise simulation of the detectors. Simulating the behavior of a detector with a GEANT based program is a two-step work. First, the virtual detector is build by describing the geometry of its elements in terms of dimension, position and material. This doesn't only concern the detector itself but any of the elements that could affect the particles behavior (this is the geometry part of the job). Once this is done, a set of generated particles are passed to the simulated detectors. GEANT simulates the interaction of these particles with matter in any traversed element and calculates the deposited energy in the detectors. Any other relevant value, such as the detection time can also be simulated (tracking).
Simulations of the Crystal Ball and TAPS have a long history, having been created together with the detectors and evolved along with them. When the new round of experiments started at MAMI, detailed and reliable software were already available for both Crystal Ball and TAPS. As the Crystal Ball geometry was by far the most complex, it was decided to base the new simulation on the software previously developed by the Crystal Ball collaboration, referred to cbsim. Cbsim was a GEANT 3 program that featured a complete description of the Crystal Ball as it was used at its previous location at SLAC. In the last three years, CBSim has evolved to a GEANT 4 program coded in C++.
As mentioned, GEANT calculates the interaction between any particle and the simulated detectors. But it is left to the user to provide a start distribution describing the studied physical process in an accurate way. Each of these start distributions exist in two versions for the decay of the η in 2γ and 6γ. Each created particle is tracked by the simulation software. All classical effects like Compton effect, scattering processes, bremsstrahlung for a charged particle are included. Roughly speaking, the same information is available for data and simulation because all experiment conditions are coded.
Basically, the detection efficiency is the ratio of the number of reconstructed events compared to the number of events created by the event generator:

$$\epsilon_{det} = \frac{N_{detected}}{N_{started}} \tag{8.4}$$

To apply this efficiency to the data, one has two solutions. The first one is to correct the data event-by-event applying the efficiency depending on the measured $T_{\eta,lab}$ and $\theta_{\eta,lab}$ as weighting factor. The second solution is to apply the

correction depending on the η -mesons center of momentum angle and incident photon energy with the phase space simulation. This purpose will be discussed in relation with the different reactions in the next part.

The grid efficiency (inclusive reaction)

The inclusive reaction identification is based on the identification of only the η -meson. The η -meso n detection efficiency depends on the correlation between the kinetic energy ($T_{\eta,lab}$) and polar angle ($\theta_{\eta,lab}$) of the mesons. The detection efficiency was simulated as function of $T_{\eta,lab}$, $\theta_{\eta,lab}$. This efficiency was corrected event-by-event using the measured $T_{\eta,lab}$, $\theta_{\eta,lab}$ of the mesons. It is therefore independent on any assumptions about the kinematical distributions of the η -mesons.

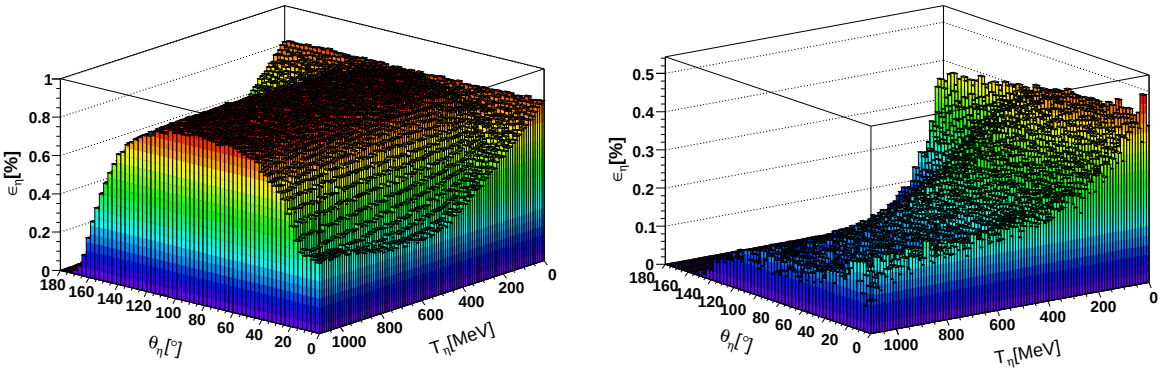

Figure 8.4: *The η meson detection efficiency for two (Right)and six neutral hits (Left)*

The chosen start distribution for the η -meson was isotropic. This start distribution $N^{start}[\theta, E_{kin}]$ contains the number of emitted η per bin of $[\theta, E_{kin}]$ for each channel. The start events were then analyzed like real data (cuts, trigger ....) after passing through GEANT. The analysis gives the second distribution $N^{recontruct}[\theta, E_{kin}]$. So the detection efficiency is:

$$\epsilon_{det_\eta} = \frac{N^{recontruct}[\theta, E_{kin}]}{N^{start}[\theta, E_{kin}]} \tag{8.5}$$

The resulting efficiency is a function of the η polar angle θ in the lab frame and its kinetic energy (figure 8.4).

^{3}He $\gamma \rightarrow \eta$ ^{3}He efficiency

Like for the inclusive channel, the efficieny is determined with a Monte-Carlo sicompmulation. The generated events are filtered with the same cuts as the data. The analysis is based on the idea that for coherent production no further hits than the two or six photons from the η -decay my be seen in the detector. The procedure can be summarized as follows:

- Coherent $\eta \rightarrow 2\gamma$ and $\eta \rightarrow 6\gamma$ events are isotropically launched into the setup
- Only 2 neutral hits for $\eta \rightarrow 2\gamma$ and 6 neutral hits for $\eta \rightarrow 6\gamma$ are accepted
- Cut on the invariant mass between 500 MeV and 600 MeV for $\eta \rightarrow 2\gamma$ and between 520 MeV and 585 MeV for $\eta \rightarrow 6\gamma$ are applied
- It is assumed that the software trigger condition is fulfilled by the six γ's of the $3\pi^0$ or the two γ's from the $\eta \rightarrow 2\gamma$
- No hits in the PID and in the TAPS Vetos are allowed
- The number of η -mesons corresponding to 2 neutral hits(N_{2hits}^{detec}) and to 6 neutral hits (N_{6hits}^{detec}), is determined
- the corresponding detection efficiency is deduced as$\epsilon_{\eta\rightarrow 2\gamma} = \frac{N_{2hits}^{detec}}{N_{started}}$ and $\epsilon_{\eta\rightarrow 6\gamma} = \frac{N_{6hits}^{detec}}{N_{started}}$

The resulting detection efficiency $\epsilon_{\eta\rightarrow 2\gamma}$ and $\epsilon_{\eta\rightarrow 6\gamma}$ is shown respectively in figures 8.5 and 8.6. The detection efficiency is plotted as function of the cosine of the η polar angle in the center of momentum for different incident photon beam energy ranges.
The detection efficiency will by applied to each value of cos θ bin and for each energy bin. The excitation function is then multiplied by the corresponding value of the tagging efficiency.

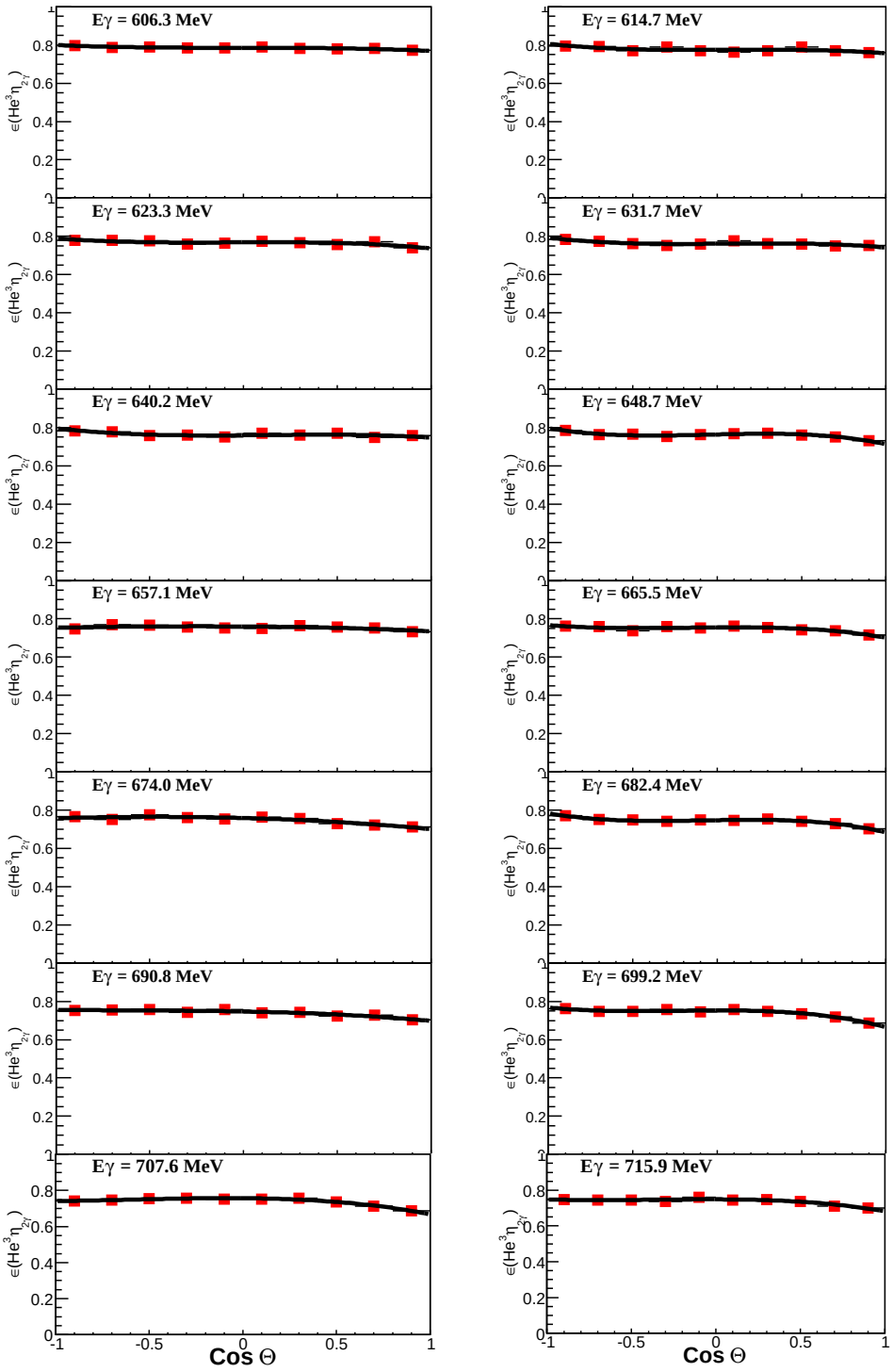

Figure 8.5: *Efficiency of coherent $\eta \to 2\gamma$ for each energy bin from threshold to 700 MeV as a function of the cos* Θ

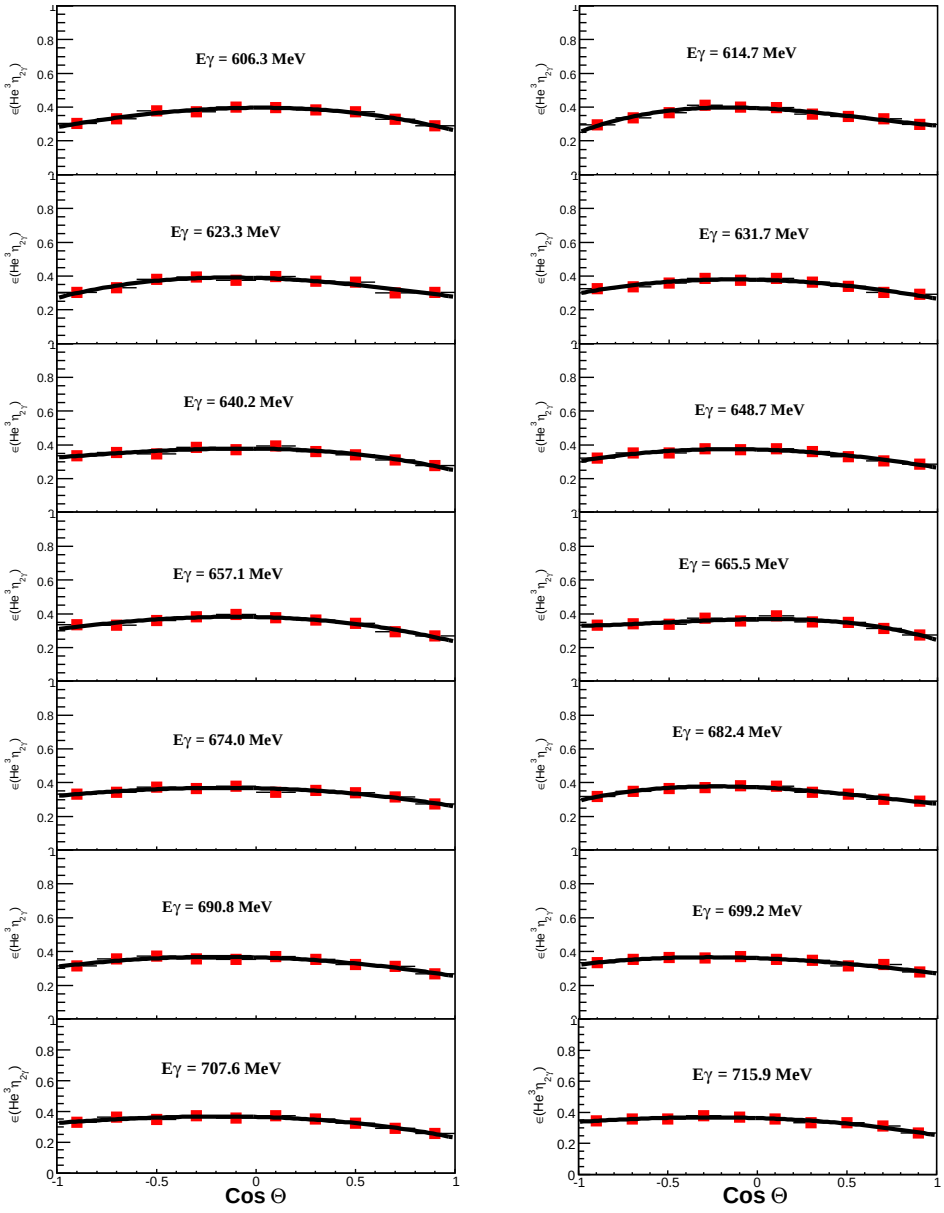

Figure 8.6: *Efficiency of coherent* $\eta \to 6\gamma$ *for each energy bin from threshold to 700 MeV as a function of the cos* Θ

8.3 Systematic errors

The discussion about the results would not be complete without an estimation of the systematic errors. The main sources of systematic errors are coming from three components. The first one is coming from the target. It's dimension was

measured as 5.3 cm ± 0.4 cm. The source of uncertainties is due to the deformation of the target cell when the temperature of ^{3}He is decreasing [40]. The resulting uncertainty for the cross section is evaluated to 7.5%. As the length of the target changed, the center of the target and then the surface density of the liquid ^{3}He has also a small uncertainty. Indeed, the temperature of the liquid is varying in a window of ± 0.6% (which give a similar variation for the density), moreover, one has to take into account the uncertainty on the measurement. The cryogenic temperature has been measured by a RuO_2 resistance with a intrinsic precision of 0.4% according to the documentation [24].
The second source of error is the flux determination which can vary up to 5% within the beamtime, more information about the uncertainties can be found in section 8.1.1. Basically it corresponds to the difference between the maximum and the minimum values of the P2/Tagger ratio in the picture 8.2.
Another source of sytematic uncertainties are the cuts applied to the data like invariant mass or missing energy cuts. A cut was applied on the invariant mass between 500 MeV and 600 MeV. Fig 8.7 (Left) shows the coherent cross section (for $\eta \to 2\gamma$)after a variation of ±10% on this cut.

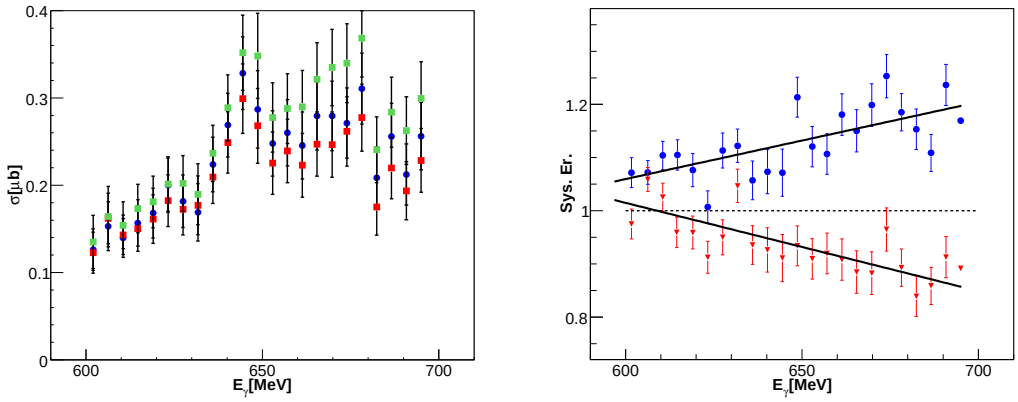

Figure 8.7: *Left: Coherent cross section of the decay $\eta \to 2\gamma$. Red, blue and green points corresponds respectively to invariant mass cut of [510,590]MeV, [500,600]MeV, [490,610]MeV. Right: Systematic difference of the coherent cross section. Blue points are the difference between red and blue points (left plot). Green points are the difference between red and green points. The black line is a fit of first order.*

Finally, one has to consider the uncertainty coming from the missing energy fits. For this purpose, one can vary the boundaries of these fits by about 10%. Figure

8.8 (left)shows the coherent cross section after the variation. The systematic difference (see 8.8 (right)) shows that the uncertainties are not depending on the fit boundaries apart for two points. This exception is due to a lack of statistic in this energy bin. Altogether, the quadratic addition of these uncertainties gives an overall of 5%. This additional error is not big enough to change the interpretation of our results.

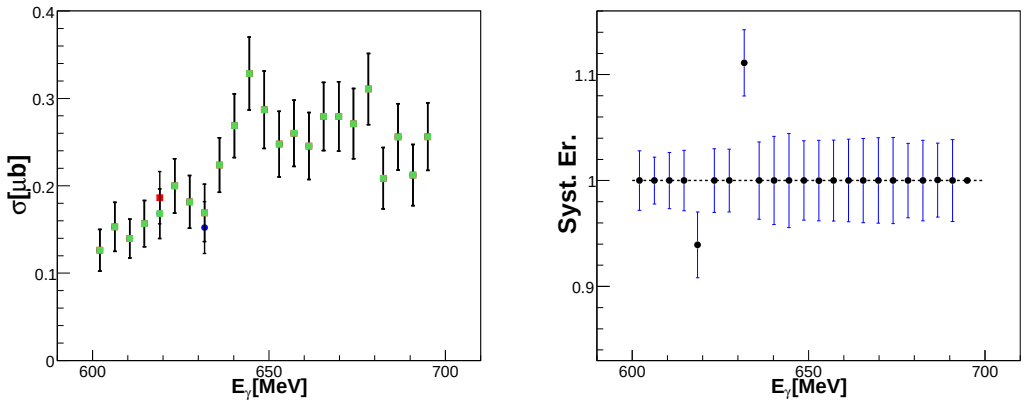

Figure 8.8: *Left: Coherent cross section of the decay $\eta \rightarrow 2\gamma$. Red, blue and green points corresponds respectively to invariant mass cut of [510,590]MeV, [500,600]MeV, [490,610]MeV. Right: Systematic difference of the coherent cross section. Blue points are the difference between red and blue points (left plot)*

Chapter 9

Results

The results of the ^{3}He experiment are discussed in this chapter. First, the inclusive quasi-free cross section is compared to the previous experiment by Pfeiffer et al. and to the ETA-MAID folded with the ^{3}He Fermi motion. Secondly, the results for the coherent η production will be presented and compared to calculations obtained by three theoretical groups using different approaches. The results of coherent η photoproduction off ^{3}He hint at the existence of a η bound state. The final part will treat the decay channel π^0-p, with which, one might access the imaginary part of the scattering length.

9.1 Total η production

9.1.1 Total η cross section

The total cross section for the inclusive η photoproduction off ^{3}He is extracted (Fig 9.1) by correcting the excitation function with the efficiency event-by-event and then by normalizing the distribution with the parameters described in the previous section. The total cross sections of the two decay modes (2γ and 6γ) are in good agreement with results from [30]. The cross section has a maximum of about 29 μb at an incident photon beam energy of 825 MeV. As explained in chapter 5, for larger values of incident photon beam energies ($E_\gamma > 800$ MeV) a background related to the competing $\eta\pi$ channel should be removed. This has been done using a missing mass analysis as detailed in [45].
Up to 820 MeV, the inclusive quasi-free cross section is compared to the ETA-MAID folded (black curve in fig 9.1). The ETA-MAID model (black curve) is

folded with the ^{3}He -nucleus Fermi motion.

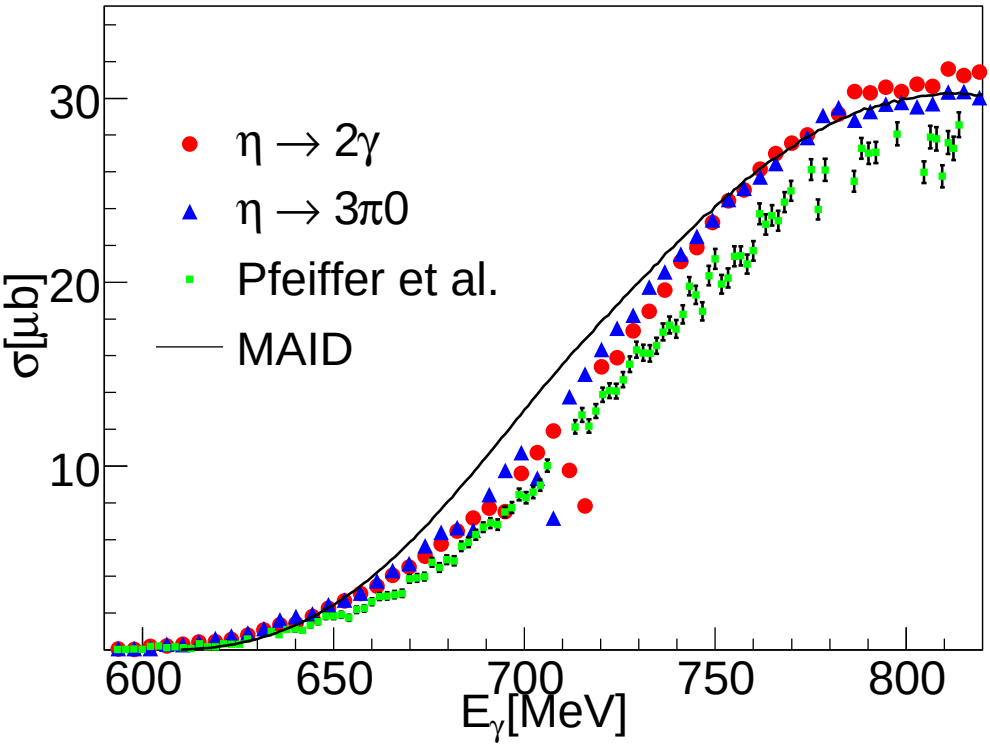

Figure 9.1: *Cross section for η inclusive production as function of the incident photon beam ($\eta \to 2\gamma$ in red , $\to 6\gamma$ in blue). The data are compared to the previous experiment's results (green squared) and to ETA-MAID model (solid line)*

9.1.2 Angular distributions

The angular distributions are indispensable to understand details that total cross section do not provide. The possible multipole decomposition of the production amplitudes has been for example explained in sect. 1.7. Considering only this resonance, according to the formula 1.14, the differential cross section should be isotropic (i.e. flat). The angular distribution in fig 9.3 is calculated by considering the nucleon at rest for different incident photon beam energies.
Close to the production threshold, the differential cross sections shows a backward peak because the incoming photon has a Fermi momentum opposite to the participant nucleon. This condition is enforced by energy conservation. Around

the free production threshold, the $S_{11}(1535)$ resonance is dominating.

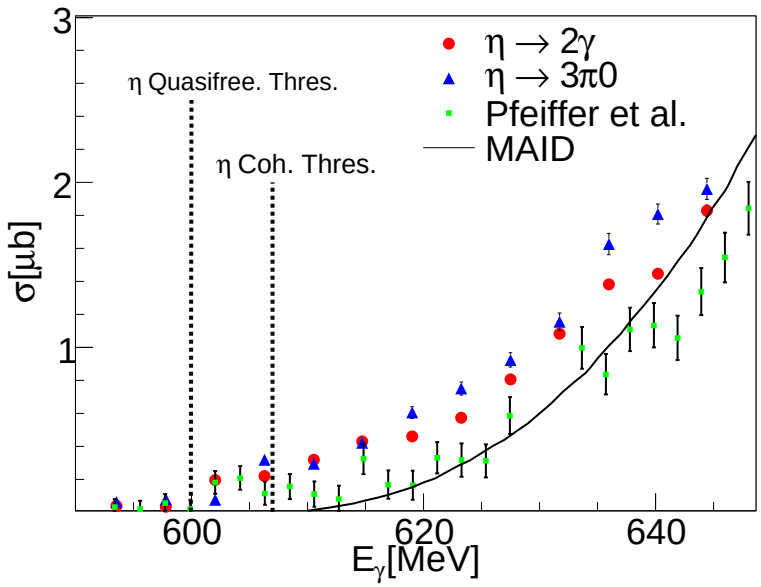

Figure 9.2: *Total cross for the inclusive η production as function of the incoming energy beam. The result of the ETA-MAID model assuming $\sigma_n = 0.66 \cdot \sigma_p$ (solid line) is compared to the data. The vertical lines indicates the production thresholds for the coherent η photoproduction (left line) and for the quasi-free reaction (right line).*

The differential cross sections are also compared to the ETA-MAID model. One can see that the agreement between the model and the experimental data is not optimal. This can be also seen in figure 9.2, where the total cross section is plotted around the quasifree and the coherent thresholds. The difference might be due to the fact that the eta-MAID cross section has been calculated for a free nucleon, folded with the ^{3}He fermi motion. No FSI of the rescattered η has been taking into account in this calculation. Quantitatively the deviation of the shape of the angular distributions from this simple model is as expected. At higher incident photon energies the effect of Fermi motion only smears out the angular distributions. Therefore the model results are essentially isotropic like the elementary angular distributions off the free nucleon. Final state interaction has the tendency to reduce the relative momentum between the meson and the rest nucleus, leading to the forward-backward asymatry oberved for the data. This effect is much more pronouced for the ^{7}Li studied in [26].

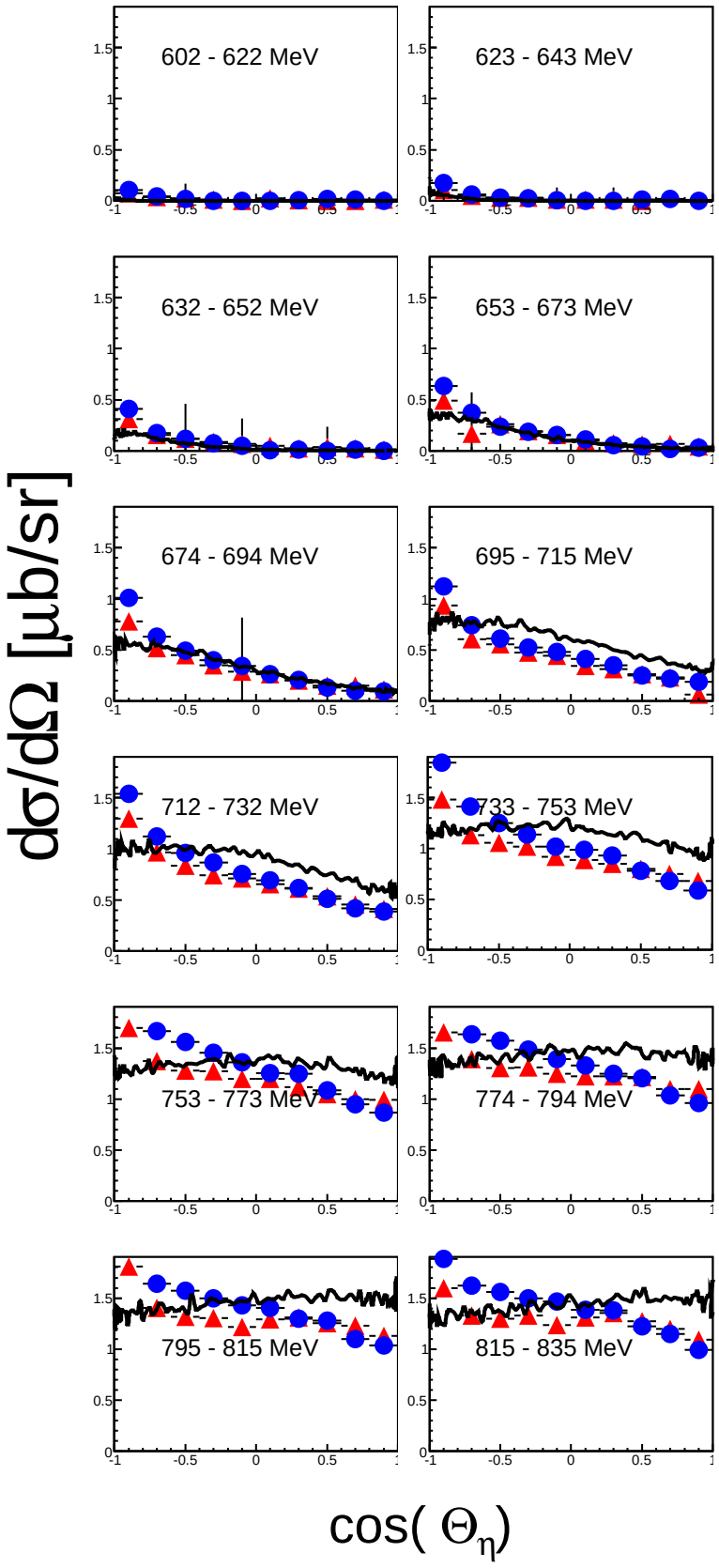

Figure 9.3: *Angular distribution as function of the cosine of the polar angle of the η meson in the γ-N system decaying into 2γ (blue) and into 6γ (red) for different incident photon beam energies compared to ETA-MAID (solid black line).*

9.2 Coherent production of η meson

9.2.1 Angular distributions

The differential coherent cross section was extracted using the method explained in section 6.3.3. The angular distributions are shown in figure 9.5 for $\eta \to 2\gamma$ and in figure 9.6 for $\eta \to 6\gamma$ and compared to the expected angular distribution on the proton (scaled to fit the data), taking into account the ^{3}He form factor are given in equation 9.1:

$$\frac{d\sigma}{d\Omega}_{coh} \sim F^2(q) \cdot \frac{d\sigma}{d\Omega}_p \tag{9.1}$$

At threshold (from 602 MeV up to 610 MeV) the angular distributions are almost flat which means that the η 's are isotropically emitted. Above 610 MeV, the angular distributions become peaked toward forward angles. For the first three energy bins (i.e. from the coherent threshold up to the quasi-free threshold) the angular distributions show a different behavior than the expected ones. However, above the quasi-free threshold, the angular distributions are in good agreement with what is expected from eq. 9.1.
One should note that this peaking toward forward angles is due to the form factor. If one eliminates the form factor from the equation 9.1, we would expect a "flat" distribution. Therefore at threshold, one could naively say that the angular distribution is proportional to the amplitude squared. Since the amplitude is proportional to the reverse of the module of the scattering length ($A \sim \frac{1}{|a|}$), the angular distributions will be in this naive view proportional to $\frac{1}{|a|^2}$.

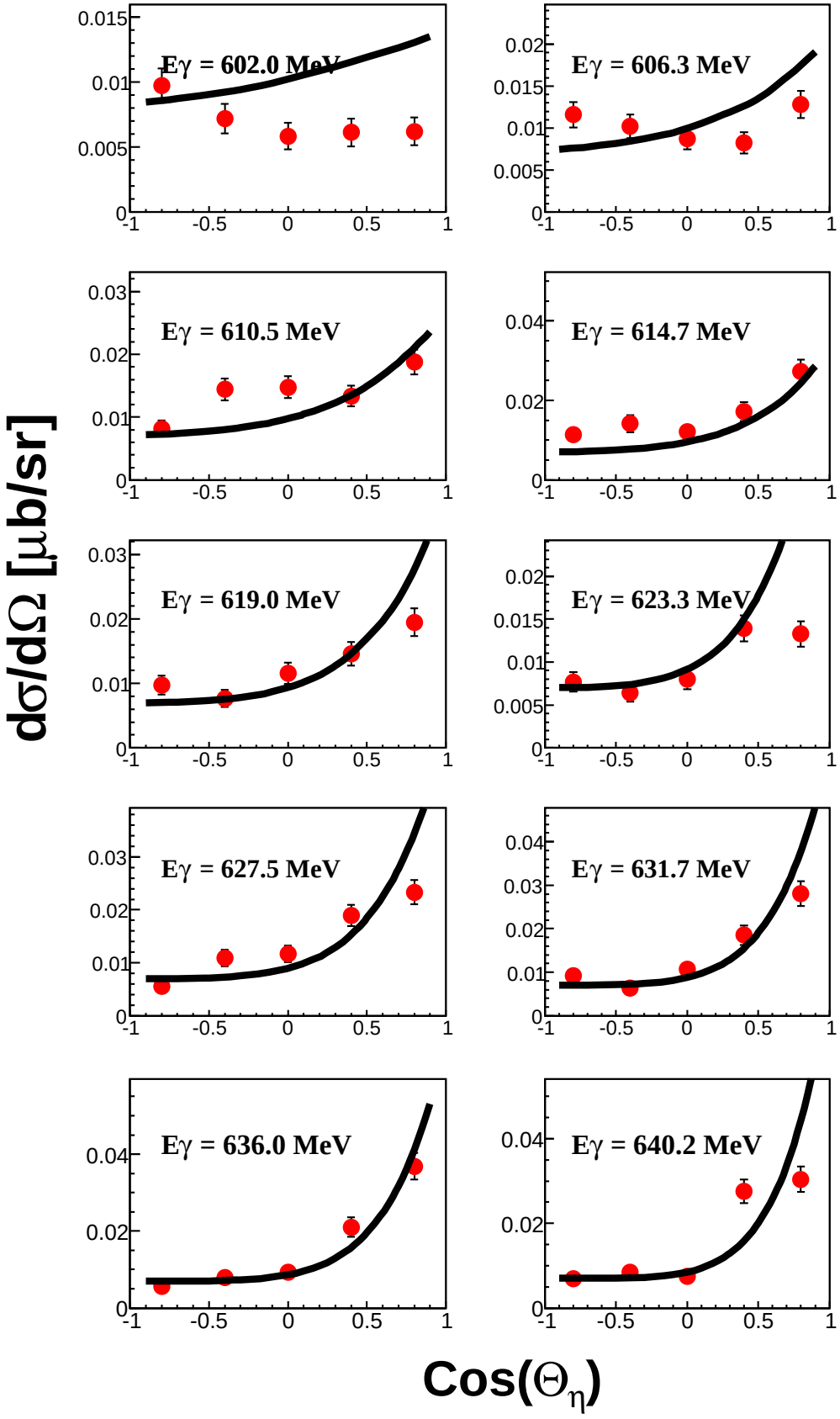

Figure 9.4: *Coherent $\eta \to 2\gamma$ Differential cross sections (ang. distributions) in the (γ,^3He) center of momentum system. The black line correspond to cross section expected from eq. 9.1. It corresponds to an extrapolation of the η photoproduction off proton folded with the ^3He form factor.*

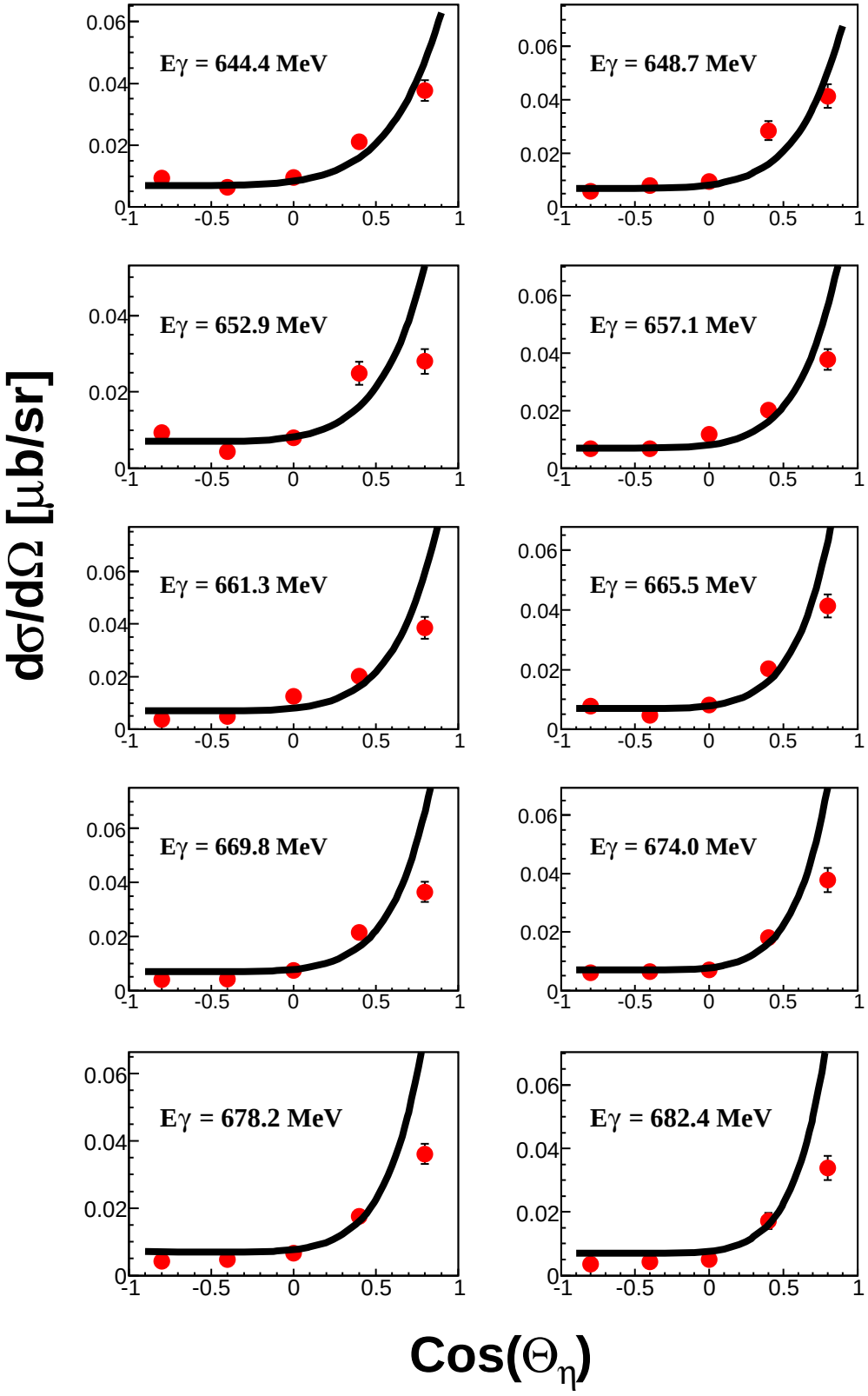

Figure 9.5: *Coherent $\eta \to 2\gamma$ Differential cross sections (ang. distributions) in the (γ,^3He) center of momentum system. The black line correspond to cross section expected from eq. 9.1. It corresponds to an extrapolation of the η photoproduction off proton folded with the ^3He form factor.*

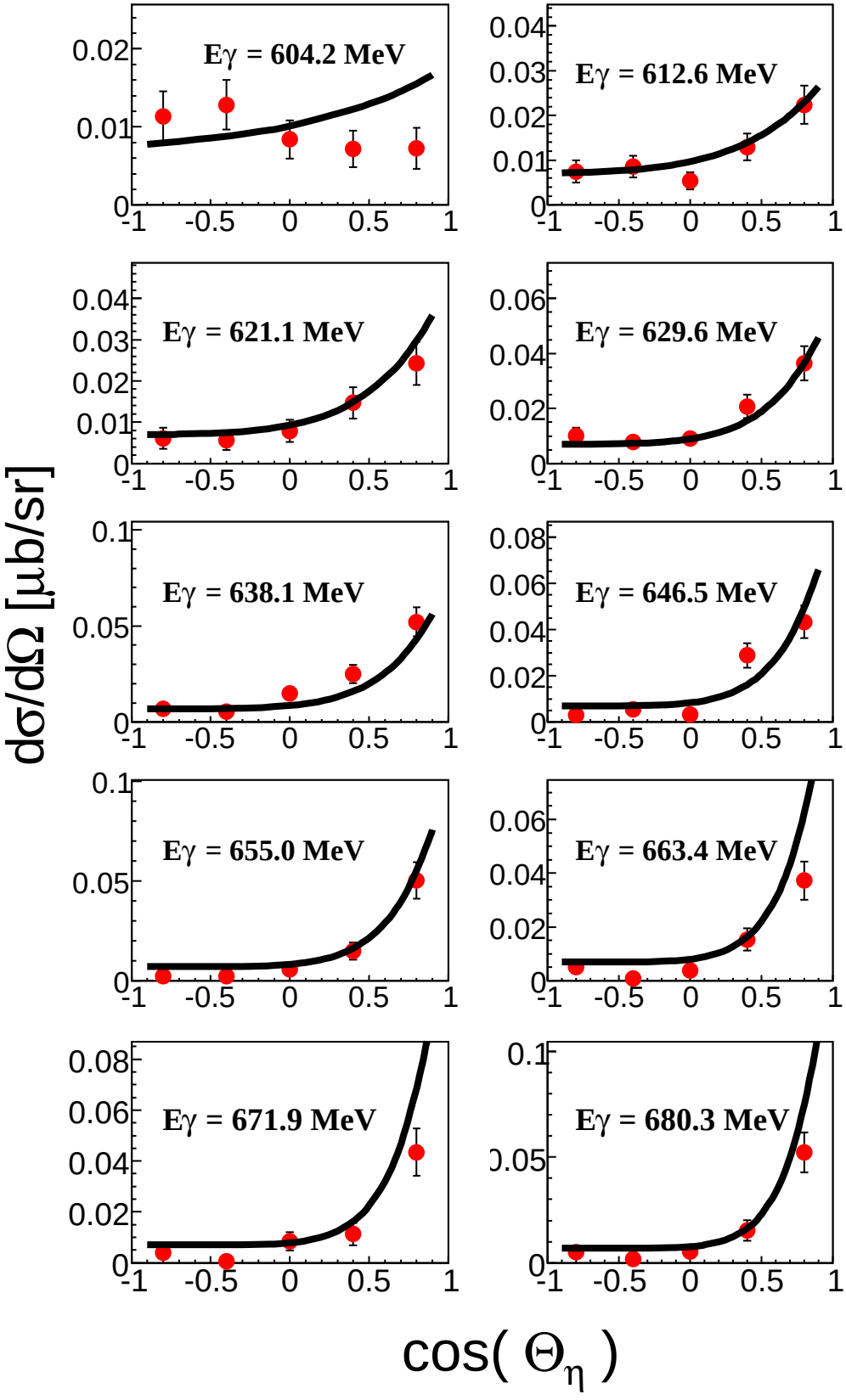

Figure 9.6: *Coherent $\eta \to 6\gamma$ Differential cross sections (ang. distributions) in the (γ,^3He) center of momentum system. The black line correspond to cross section expected from eq. 9.1. It corresponds to an extrapolation of the η photoproduction off proton folded with the ^3He form factor.*

9.2.2 Total cross section

The total cross section has been obtained by integrating the angular distributions. Fig 9.7 (left) shows the total coherent cross section compared to the quasifree cross section from the coherent threshold up to 700 MeV. The obtained coherent cross section shows a strong enhancement at threshold in line with the previous results as shown in figure 9.7 (right). However, in contrast to the results obtained by Pfeiffer et al., the cross section does not show any drop around 630 MeV.
As discussed in sect 8.2.1 the strong enhancement at coherent threshold might be explained by the small value of the scattering length module. One should note that apart from the better statistical quality, the present data have also smaller systematic uncertainties than the previous ones. This is mainly due to a better signal-to-background ratio in the missing energy spectra because of the larger solid angle coverage (almost 95% against 30% for the previous experiment).

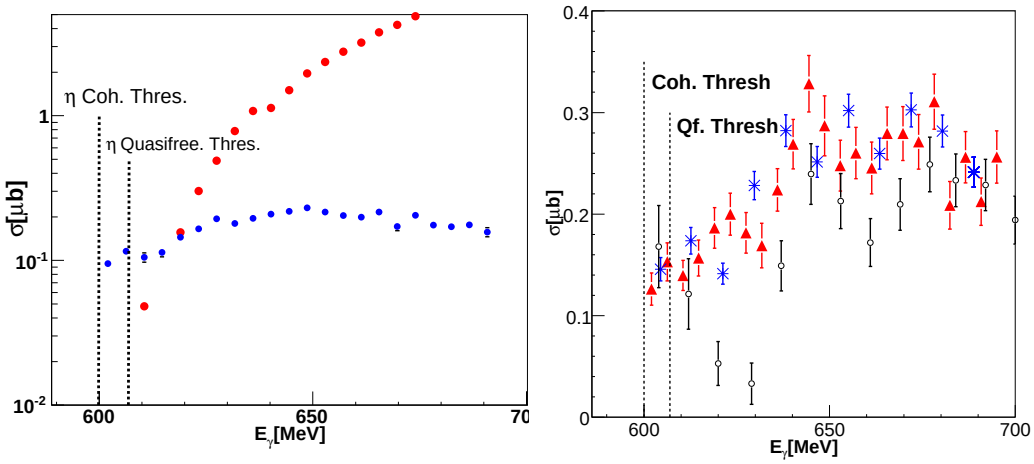

Figure 9.7: *Left: Comparison of coherent (blue points) and breakup cross section (red points) cross section of $\eta \to 2\gamma$. Right: η Coherent cross section ($\eta \to 2\gamma$ in red $\eta \to 3\pi^0$ in blue) compared to results by Pfeiffer et al (black)*

The almost 4π solid angle coverage allows to suppress a large fraction of events from breakup reactions via detection of the participant nucleons, since only events with two (or six) photons and no further hit in the detector have been excepted.

Comparison to the Kamalov model and Shevchenko models

We can compare the data to the predictions made by Kamalov and to the ones made by Shevchenko which have been discussed in the introduction. The comparison is shown in Fig 9.8. The work of Kamalov et al. [21] is based on an optical model modified by the implementation of the Fermi motion and the Pauli blocking effect. The Kamalov calculation shows a much smoother rise then the steep rise observed in the present data. Kamalov did in fact not include any η^3He bound states.

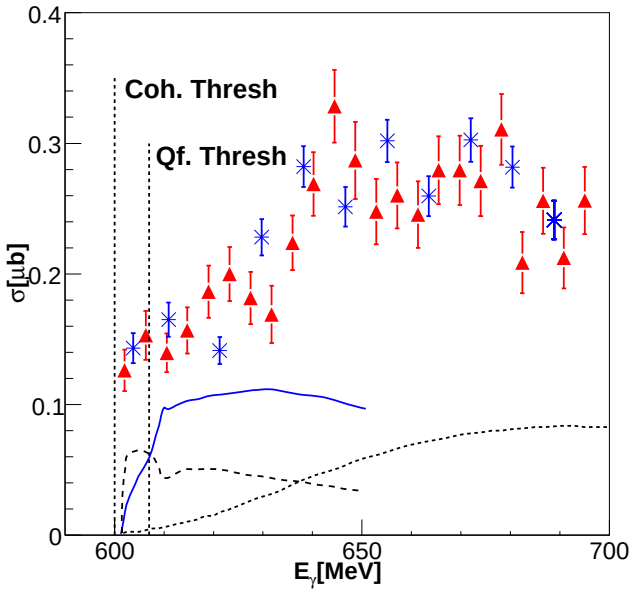

Figure 9.8: *Comparison of η coherent cross section with models by Kamalov et.al. (dotted line) and Shevchenko et.al. (dashed line, solid line)*

Concerning the comparison with the Shevchenko model (discussed in section 2.2) which predicted a strong rise at the coherent threshold region, the model did not reproduce the absolute scale of the measured cross section. This might mean that the scattering length used in the Shevchenko calculation is too small or that the ηN potential is too large.

Comparison with the Fix and Arenhoevel model

The measured total coherent cross section has been after that compared at threshold to calculations made by A.Fix and H.Arenhoevel [13] (see section 2.2) as shown in figure 9.9. These calculation show similar behavior as the Shevchenko model.

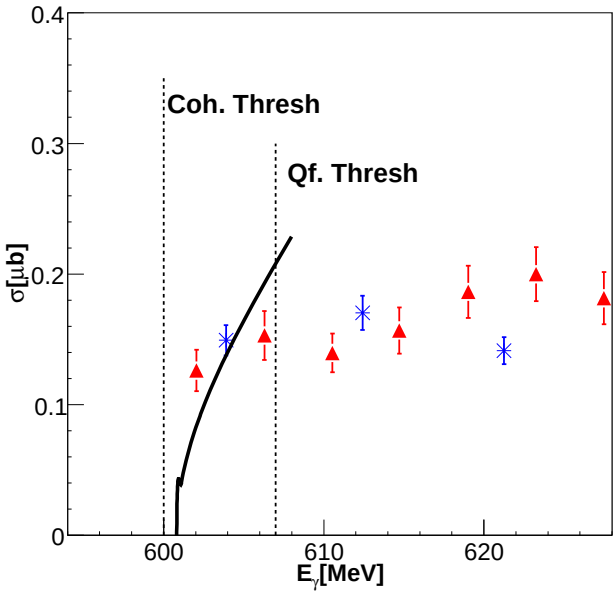

Figure 9.9: *Total coherent cross section for η production compared to Fix and Arenhoevel model*

In the calculation of Fix et al. the steep rise in the vicinity of the coherent threshold is due to a virtual state (which doesn't imply necessarily a bound state). Fix's model could not determine theoretically whether the η -N interaction is on the "bound" or "unbound" state. This not possible because the model fit the results from the reaction dp $\rightarrow\eta$ ^{3}He [27]. This reaction suffered from poor statistics as shown in figure 9.10. A definitive answer is requiring a more precise measurement on the order of keV instead of MeV.

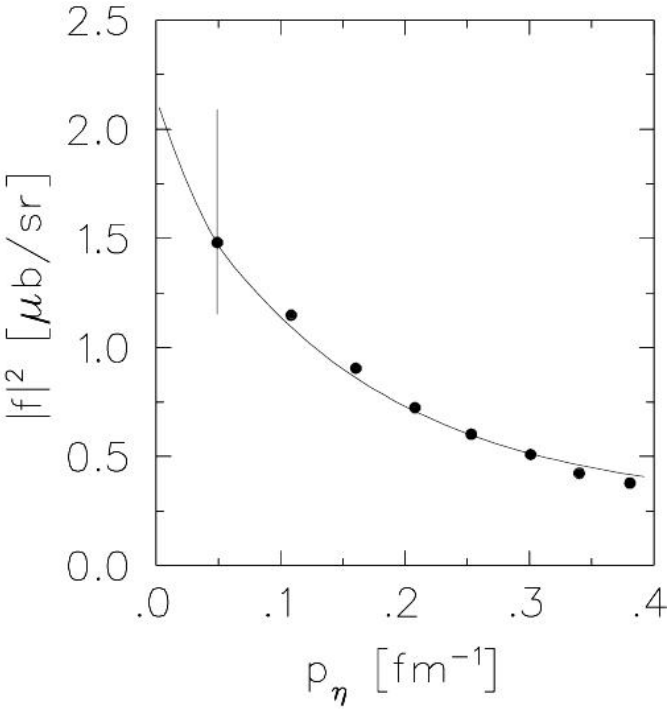

Figure 9.10: *Production amplitude squared for the reaction* $^3He\ (\gamma,\eta)^3He$ *(black line) compared with the experimental results for* $d(p,\eta)^3He$ *[27] (black point).*

Summary

None of the models presented reproduced reasonably the measured coherent cross section. However, both calculations of N. Schevchenko reproduced the strong rise observed at threshold. The scattering length was the same in both calculations. The only difference comes from the transition matrix of η N. According to [37] a real part above 0.5 means that the η undergo a strong final state interaction inside the nucleus which could lead to a meson bound state. Assuming a resonance-like behavior, the state should manifest itself in a sharp rise just above threshold as shown in Fig 9.11(the left side of the peak is subthreshold and cannot be observed via the η production for this reason.)

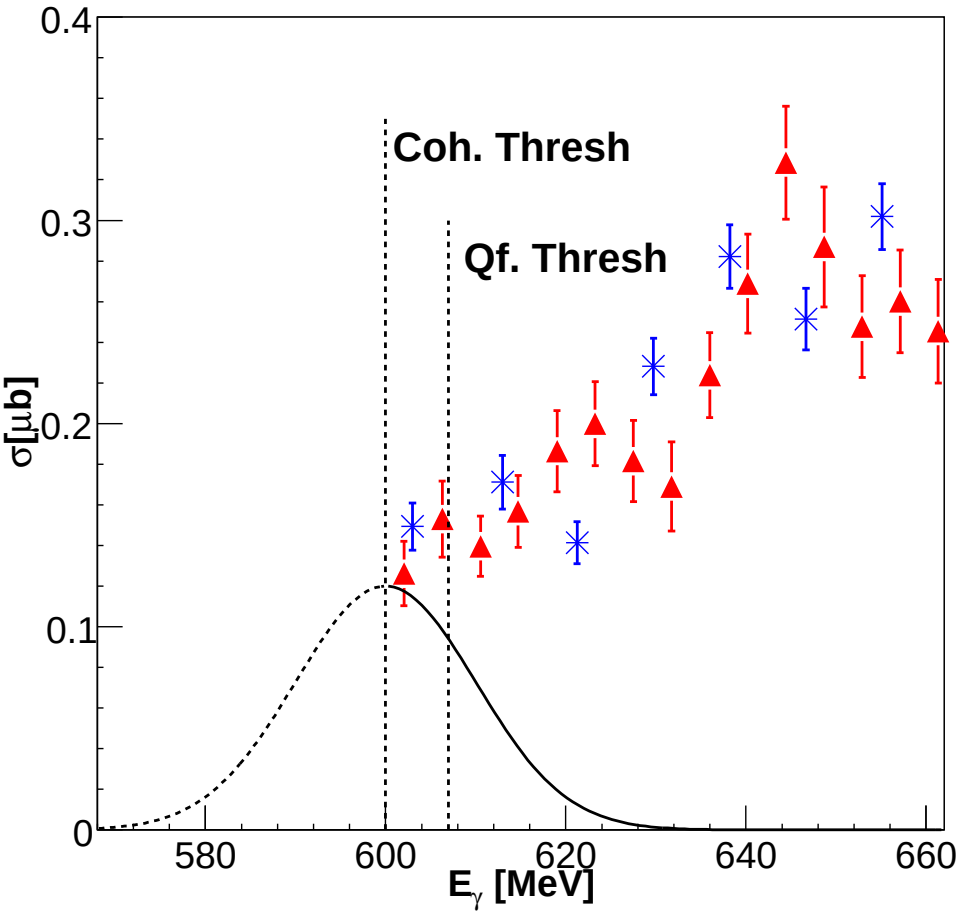

Figure 9.11: *η coherent cross section. The expected shape of the resonance like structure is plotted (with a FWHM of 39 MeV see [30])above threshold in continue black line, below threshold in dotted black line.*

Interpretation from the photon induced reaction

More recently a more precise measurement of the reaction $pd \rightarrow^3 He\eta$ has been done by Mersmann et al.. C. Wilkin et.al. [43] gave then an explanation of the shape of the differential cross section close to threshold. At these energies, the η is exclusively produced via a s-wave, before the p-wave quickly contributes. In photoproduction both contributions are isotropic which is clearly seen in the flat distributions at threshold (see figure 9.4). The s-wave amplitudes are independent of p_η whereas the p-waves vary linearly with p_η. In the threshold region these two

components can interfere with each other and this interference is proportional to $\cos\theta$. To observe this dependence on $\cos\theta$, one could plot the angular dependence in terms of an asymmetry parameter α defined as:

$$\alpha = \frac{d}{d(cos\theta_\eta)} ln\left(\frac{d\sigma}{d\Omega}\right)\Big|_{cos\theta_\eta} = 0 \tag{9.2}$$

where $\frac{d\sigma}{d\Omega}$ is approximated as:

$$\frac{d\sigma}{d\Omega} = \frac{q}{k}(A_0 + A_1\cos\theta + A_2\cos^2\theta) \tag{9.3}$$

α corresponds to the ratio $\frac{A_1}{A_0}$ (the complete description of the calculation is in appendix A). The variation of α for the present data and ANKE measurement is shown in fig 9.12 as a function of the η momentum.

The picture shows that at high p_η i.e. above 70 MeV, the asymmetry parameter rises linearly and at low values of p_η α becomes negative. The solid line in Fig 9.12 is the result of fitting the experimental data with the equation:

$$\alpha = 2p_\eta \frac{\Re f_s^* C}{|f_s|^2 + p_\eta^2 |C|^2} \tag{9.4}$$

where p_η is the η momentum and the expression $f_s^* C$ represents the phase variation of the s-wave amplitudes. This phase variation comes from the interference between the s and p-waves.

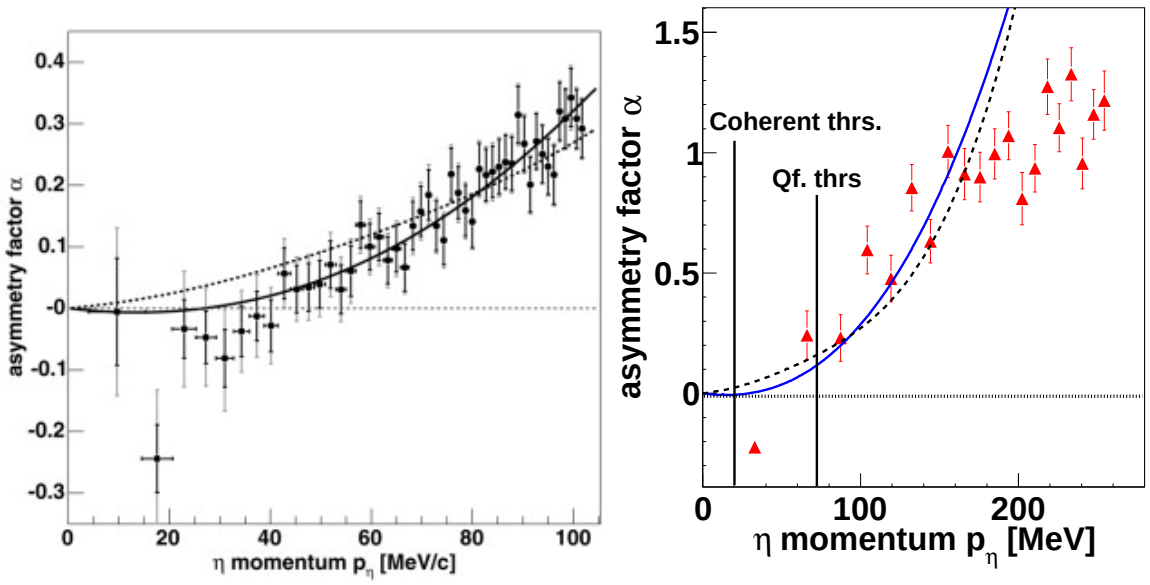

Figure 9.12: *Asymmetry parameter α extracted from 9.2 as a function of the c.m momentum of the η meson. The solid line is a fit of the data where the s-wave amplitude f_s was introduced. The dashed line was obtained after neglecting the phase variation of f_s Right: Results from the ANKE data from [28]* Left:*Results from the present experiment*

The stronger the interference between s-waves and p-waves is, the stronger the rise of the α becomes. The dotted line is obtained after neglecting the phase variation of f_s by replacing f_s by $|f_s|$. This fitting fails to reproduce the shape of the low-momentum data.
The term C in equation 9.4 is proportional to the positions of nearby poles p_1 and p_2. The present statistic is not high enough to extract these poles. However, the fit seems to reproduce the same behavior in the medium range of energy bin and even goes to negative values at low kinetic energy like the experimental data. C. Wilkin has extracted from the experimental data the η -^{3}He scattering length: $a = (\pm 10.9 + 1.0i)$. The two signs of Re(a) indicate the possibility of either a bound or a virtual state.

Summary

The explanation given by C. Wilkin might not be necessarily applied to the photon induced reactions. However an alternative explanation can be given: the

behavior of the α parameter could also be due to the influence of the form factor. In figure 9.4 the angular distribution is reproduced by the equation 9.1 where the form factor is the dominant term.

9.2.3 Comparison with ^{7}Li results

The coherent η photoproduction has also been observed in ^{7}Li data taken during 2005 in an experiment performed at the MAMI facility. This was the first observed coherent η signal in a A>3 nucleus. The coherent ^{3}He cross section is compared in Fig 9.13 to the ^{7}Li one [26]. As expected, the ^{7}Li coherent cross section shows a softer rise then the ^{3}He one. That might be due to the fact that the pole of the η bound state is further away in Li compare to He.

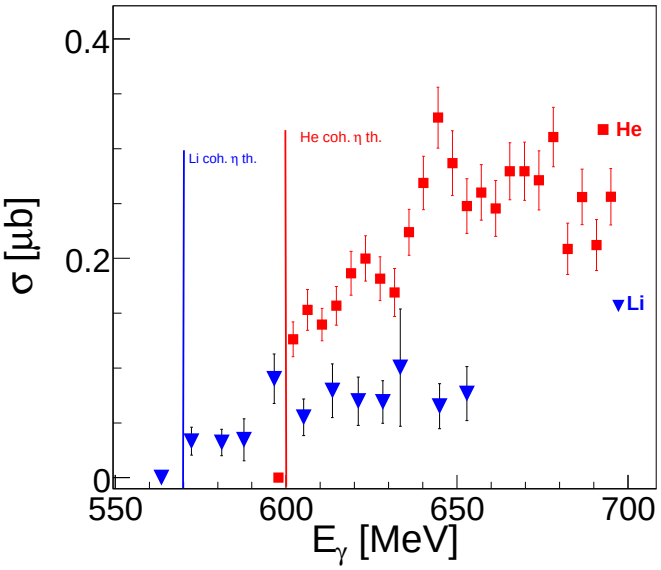

Figure 9.13: *η coherent cross section extracted by integrating the normalized coherent simulation. The ^{3}He data (Blue) is scaled by the mean value of the ratio : $F^2(q^2)_{^7Li}/F^2(q^2)_{^3He}$ to be comparable with the ^{7}Li (Red). The short dashed lines are the coherent production threshold (510 MeV for ^{7}Li and 600.6 MeV for ^{3}He)*

9.3 π^0-proton channel

The reaction: $\gamma + {}^3He \rightarrow {}^3He_\eta \rightarrow \pi^0 + p + X$ with the $\pi^0$and the proton emitted in back-to-back is investigated. This channel is a good candidate to extract the value of the imaginary part of the scattering length.

Fig 9.14 shows the excitation function for different opening angles of the pion and the proton in the γ^3He frame, the vertical lines indicate the position of the resonance in this energy region. As expected, the single π^0 photoproduction is emitted by the excitation of the $\Delta(1232)$. One can observe that the $\Delta(1232)$ resonance position is shifting towards high incident photon beam energies when the opening angle is decreasing. If one observe the kinematics of the reaction: in the center of momentum system (of ^{3}He and proton) the decay of the $\Delta(1232)$ takes place with the opening angle of 180° as long as the Δ is at rest in this frame. For smaller opening angles, the resonances cannot be at rest anymore but have to decay in-flight in the γ^3He frame. This is the case for increased photon energies since the available energy in the center of momentum frame is larger. So the Δ position is shifted towards higher photon energies for decreasing opening angles.
Fig 9.15 left shows the comparison between the excitation function corresponding to a π^0-p decay in a opening angle in the range 150°-165° and 165°-180° in the γ-^{3}He system.

The remaining background is reduced by calculating the difference between both distributions, a clear enhancement is observed at the η coherent threshold (vertical dashed line) seen in Fig 9.15 (right). This peak-like structure has been observed in the previous experiment with 10 times less statistic.

However, a more precise observation of the opening angles shows that in the range 120°-140° a first structure appears around 550 MeV and a second structure at 750 MeV. These two bumps drift toward higher incident photon beam energies for increasing opening angles.

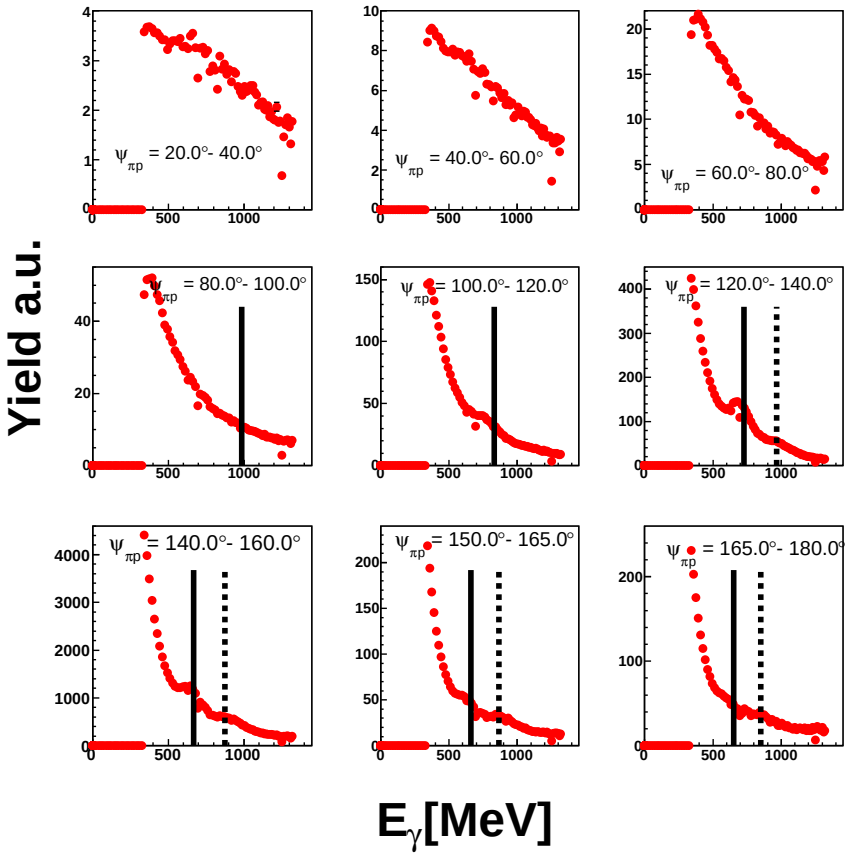

Figure 9.14: *Count rate of π^0-p production in the γ-^{3}He center of mass for different opening angle ranges. The dashed-dotted represent the expected position (according to appendix C) of the $F_{15}(1680)$ and the solid line is the $D_{13}(1520)$. The delta resonance is moving from the right to the left side.*

They are residual signals from the second (D_{13}) and third nucleon (F_{15}) resonance region in single π^0-production after specific kinematical selection related to the opening angle. The observed structure is therefore probably an artifact from the single π^0 photoproduction off the nucleon.
This is illustrated by single π^0 photoproduction off the deuteron [11] (see fig 9.16) where are the D_{13} and the F_{15} resonances are clearly seen.

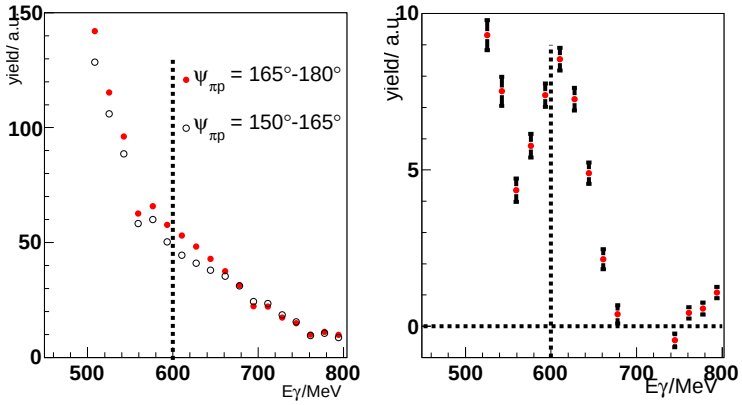

Figure 9.15: ***Left**: Count rate of the π^0-proton production for opening angle range of 150°-165° (open circles) compared to 165°-180° (red) in the CM system. **Right**: Difference of both excitation functions. A cut on the proton kinetic energy is applied in order to remove background coming from the quasifree production. Dashed line is the position of the η coherent threshold.*

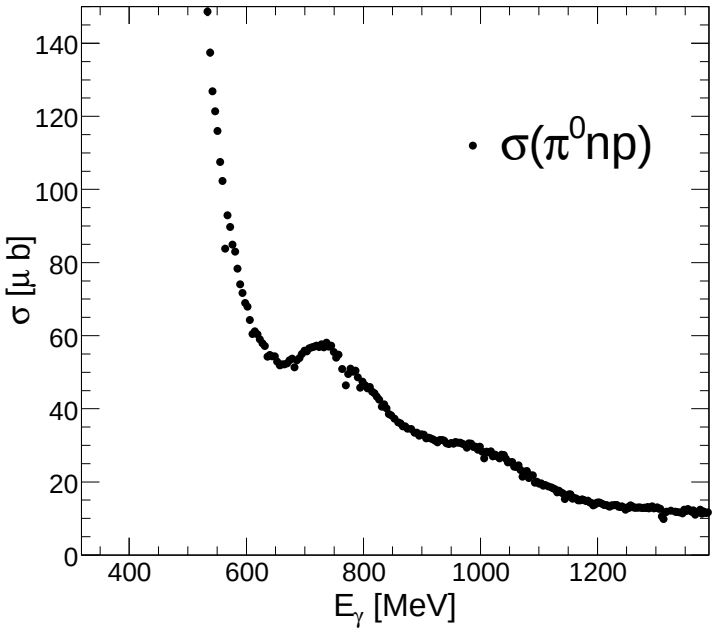

Figure 9.16: *Total cross section of the quasi-free inclusive π^0-photoproduction on the deuteron. Two bumps are visible around 700 MeV and 1 GeV which are respectively dominated by the $D_{13}(1520)$ and $F_{15}(1680)$ resonances*

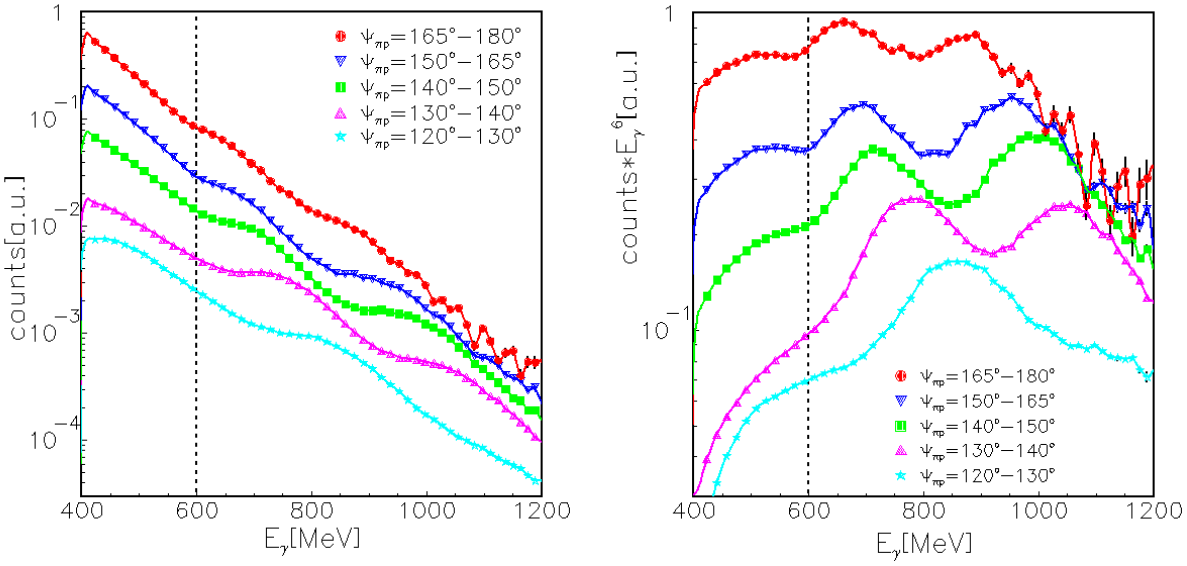

Figure 9.17: *Excitation function of π^0-proton pairs with different opening angle range in the γ-^{3}He center of mass. Left: Excitation function, Right: multiplied by E_γ^6 to remove the energy dependence.*

Fig 9.17 shows that the same structure is still visible when the excitation functions for different opening angles are scaled.
As we demonstrate it, the peak like structure shown in 9.15 is not coming from an η meson produced via an inelastic reaction. This means that for the case of ^{3}He , the π^0-proton channel is no longer a promising tool to observe the η bound state.

9.4 Conclusion and outlook

The experimental results for the η photoproduction off ^{3}He have been presented. The main goal of this thesis was to increase the statistic from the previous experiment performed by Pfeiffer et al. The large acceptance of the crystal ball combined with TAPS allows us to improve the number of detected events by an order of magnitude.
The strong rise of the excitation function at the coherent threshold hints to a strong final state interaction. A similar behavior was observed for the results form the hadron induced reaction dp + p $\rightarrow$ ^{3}He η. Also, the angular distributions show an isotropic distribution which is not expected from the form factor dependence in the threshold region. A similar measurement for ^7Li shows also a strong threshold enhancement but less pronounced than for ^{3}He . Theoretical calculations are not able to describe satisfactorily the coherent cross section around threshold. The models use values for the η N scattering length that result in a strong attraction of η and ^{3}He, but do not demand a bound state. More effort is needed on the theoretical side to clarify the existing discrepancies.
The excitation function for the π^0-proton production for large opening angles in the γ-^{3}He system was offering very promising possibilities to observe η mesic nuclei. The present experiment has shows that in the case of the ^{3}He the measurement of this channel is impossible. This is mostly due to residual background coming from the resonances. These resonances are lying in the coherent threshold region at large opening angle so the huge amount of quasi-free π^0production make the extraction of the interesting channel impossible.
The photo reaction of $\gamma A \rightarrow \eta\pi^0 A$ can be used to study the η d [19] and the η ^{4}He[19] interactions. This reaction is dominated by the excitation of the Δ^* (1700) D_{33}. Thus the amplitude from the proton and the neutron are adding up instead of suppressing each other in the η coherent reaction off deuteron and off ^{4}He. Furthermore, the η is emitted with a very low kinetic energy which is a necessary condition to study the FSI between η and A.

Chapter 10

Acknowledgements

Als erstes möchte ich mich bei Professor Bernd Krusche bedanken. Was ich jedem Doktorand nur wünschen kann, ist mit so einer geduldigen und zugänglichen Person arbeiten zu dürfen. Es war mir eine Ehre und eine grosse Freude Sie als Doktorvater zu haben. Ich bedanke mich ebenfalls bei Prof Metag, der immer grosses Interesse an meiner Arbeit zeigte und wichtige Beiträge bei deren Korrektur geleistet hat.
I would like to thank all the members of the A2 collaboration for the nice and efficient working atmosphere. I especially thank the target group of Mainz (Andreas Thomas, Mauri, Patri " mujer de principios") where I spent two years to prepare the L^3He target .
Je tiens à remercier toute la "French Team " du bureau 2.12 de première génération (Cedric, Fabien, Kristoff et Thierry) et tout ceux qui constituent le groupe aujourd'hui (Ika, Tiko, Marcus, Therese, Manu et Frau Witth). Une mention spéciale pour la petite Bene qui m'a fait profiter de ses nombreux conseils. Je remercie aussi Yasser ("Choukrane Khouyah") qui fut le meilleur pote de galères et un tres bon joueur de PES (d'ailleurs merci 'Cechm') et Domi pour ses qualités IT et sa bonne humeur. Je dédicace l'ensemble de ce travail au Dr Igal Jaegle, sans qui rien n'aurait été possible, je te souhaite tout ce qu'il y a de meilleur dans la vie qu'importe "OÚ ?" tu seras.
An ka remewcié tout moun ki té ka supowté pou mwen pé sa vwè bout' a chimin la. On special dédicace ba Cpt Steve, Amiral James, fabwice, Cynthia, Christel é Piè, é Nadima (fille de Crelle). An ke fin ave Pap' en Mwen épi Manman mwen. An sav ki jan sa té red ba zot lè zo té ka vwè mwen en zafè, zo té toujou avè mwen té ka lité, mèsi on pil. On big fos ba le frangin, sav an ké toujou la èvèw.
Chciałbym także złożyć podziękowanie całej rodzinie Rachtanów, a szczególnie

Pani Krystynie Rachtan za jej nieograniczoną tolerancję dla błędów, które popełniałem pisząc moją pracę doktorską po angielsku, a które cierpliwie poprawiała.Chciałbym zadedykować tę pracę mojej najdroższej Kasi. Dziękuję Ci za wsparcie w trudnych chwilach i cierpliwe znoszenie moich humorów, za to że byłaś, gdy Cię potrzebowałem i pokazywałaś mi moją drogę naszą drogę.

Appendix A

Asymmetry parameter α

The angular dependence may be summarized in terms of an asymmetry parameter α defined as :

$$\alpha = \frac{d}{d(cos\theta_\eta)} ln\left(\frac{d\sigma}{d\Omega}\right)\Big|_{cos\theta_\eta} = 0 \tag{A.1}$$

where: $\frac{d\sigma}{d\Omega}$ is defined as:

$$\frac{d\sigma}{d\Omega} = \frac{q}{k}(A_0 + A_1\cos\theta + A_2\cos^2\theta) \tag{A.2}$$

Then A.2 becomes:

$$ln\frac{d\sigma}{d\Omega} = ln\frac{q}{k} + ln(A_0 + A_1\cos\theta + A_2\cos^2\theta) \tag{A.3}$$

and A.1 is:

$$\begin{aligned}\frac{d}{d\cos\theta} &= \frac{1}{A_0 + A_1\cos\theta + A_2\cos^2\theta}\cdot(A_1 + 2\cos\theta) \\ &= \frac{A_1}{A_0}\end{aligned} \tag{A.4}$$

Appendix B

Calculation of the differential cross section from the ^{3}He form factor

One needs to estimate the angular distribution depending on the form factor of ^{3}He in order to plot the expected behavior of the differential cross section:
If we consider a photon energy $E_\gamma = 602$ MeV which is 2 MeV above the coherent threshold, the energy in the center of momentum is given by the formula:

$$\sqrt{s} = \sqrt{2E_\gamma \cdot m_{^3He} + m_{^3He}^2} = 3358.11 MeV \tag{B.1}$$

With $m_{^3He} = 2808.391$ MeV. The momentum p_η^* and the energy E_η^* of the η meson and the momentum $p_{^3He}^*$ and the energy $E_{^3He}^*$ of the target nucleus is calculated in the center of momentum as:

$$E_\eta^* = \frac{s - m_{^3He}^2 + m_\eta^2}{2\sqrt{s}} = 549.64 MeV \tag{B.2}$$

$$p_\eta^* = \sqrt{E_\eta^2 - m_\eta^2} = 51.7 MeV \tag{B.3}$$

$$E_{^3He}^* = \frac{s + m_{^3He}^2 - m_\eta^2}{2\sqrt{s}} = 2808.88 MeV \tag{B.4}$$

$$p_\eta^* = \sqrt{E_{^3He}^2 - m_{^3He}^2} = 51.7 MeV \tag{B.5}$$

$$\tag{B.6}$$

In order to make the transformation into the laboratory easier, one assumes the cases where the η meson is detected in the forward direction ($\Theta_\eta^* = 180°$, $\Theta_{^3He}^* = 0°$, $p_z^* = 51.7$ MeV) and the backward direction ($\Theta_\eta^* = 0°$, $\Theta_{^3He}^* = 180°$,

p_z^* = -51.7 MeV). For this two cases one has:

$$\beta_z = \frac{E_\gamma}{E_\gamma + m_{^3He}} = 0.177 \tag{B.7}$$

$$\gamma = \frac{E_\gamma + m_{^3He}}{\sqrt{s} = 1.0160} \tag{B.8}$$

$$\tag{B.9}$$

and $p_{z,lab}$ becomes (conversion: 197 MeV.fm):

$$p_{z,lab}(\Theta^*_{^3He} = 180°) = 452.6MeV = 2.29fm^{-1} p_{z,lab}(\Theta^*_{^3He} = 0°) \quad = 557.5MeV = 2.83fm^{-1} \tag{B.10}$$

For the extraction of the cross section, the form factors for the different momentum transfers play an important role. The momentum transfer q is equal to the difference of the momentum before and and after the reaction (^{3}He is at rest):

$$q = p_{z,lab,after} - p_{z,lab,before} = p_{z,lab,after} - 0 = p_{z,lab} \tag{B.11}$$

The form factor is shown in figure 1.10, the two values for $\Theta^*_\eta = 180°$, $\Theta^*_{^3He} = 0°$ are :

$$F(q, \Theta^*_{^3He} == 180°, \Theta^*_{^3He} = 0°) = F(q = 2.29fm^{-1}) = 0.073 \tag{B.12}$$

$$F(q, \Theta^*_{^3He} == 0°, \Theta^*_{^3He} = 180°) = F(q = 2.83fm^{-1}) = 0.018 \tag{B.13}$$

The cross section is proportional to $F^2(q)$. The dependence of the cross section for the η going in forward direction compared to the cross section in backward direction is proportional to the squared ratio of the form factor for these cases. So the cross section ratio behave like:

$$\frac{\frac{d\sigma}{d\Omega}(\Theta^*_\eta = 0°)}{\frac{d\sigma}{d\Omega}(\Theta^*_\eta == 180°)} = \frac{F^2(q, \Theta^*_\eta = 0°)}{F^2(q, \Theta^*_\eta = 180°)} = \frac{0.073^2}{0.018^2} = 16.4 \tag{B.14}$$

Appendix C

Calculation of the resonance position

We calculate the resonance nominal mass as function of the opening angle ($D_{13}(1520)$ and $F_{15}(1680)$). It was done for the photoreaction γ + p(d) $\rightarrow \pi^0$+ p(d) by taking into account the ^{3}He Fermi motion. The opening angle of π^0-Proton was calculated in the center of mass of the system γ^3He . Fig C.1 and fig C.2 shows the dependence of the nominal mass as function of the opening angle in the lab system.

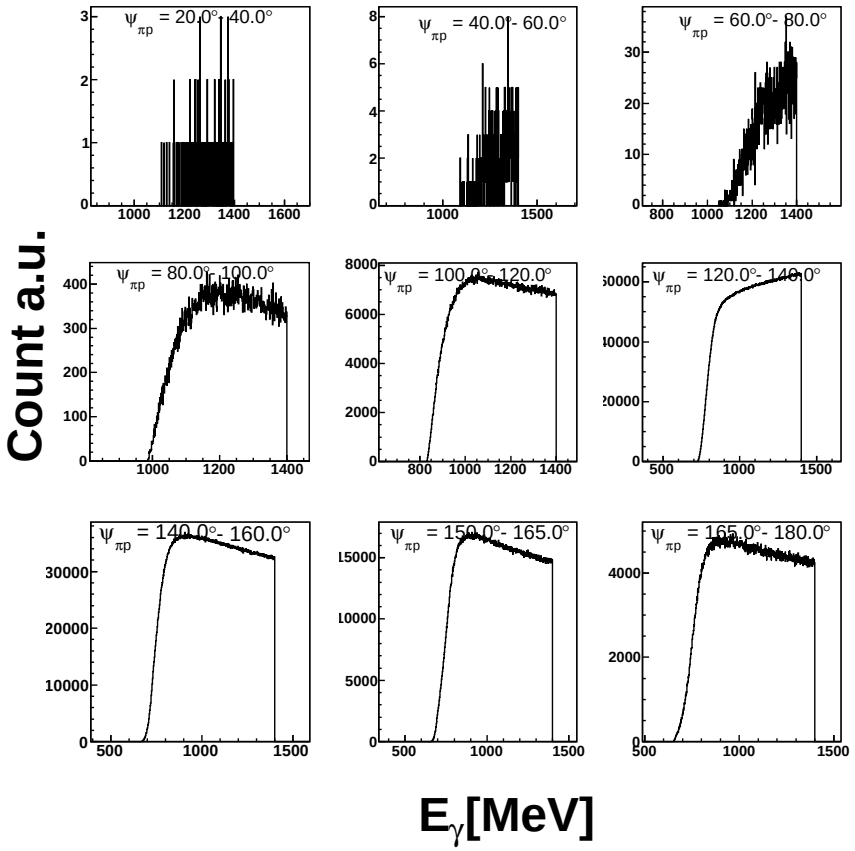

Figure C.1: *Count rate of the simulated π^0-p production in the γ-^{3}He center of mass considering the D_{13} resonance. The position of the resonance is corresponding to the value of the first energy bin.*

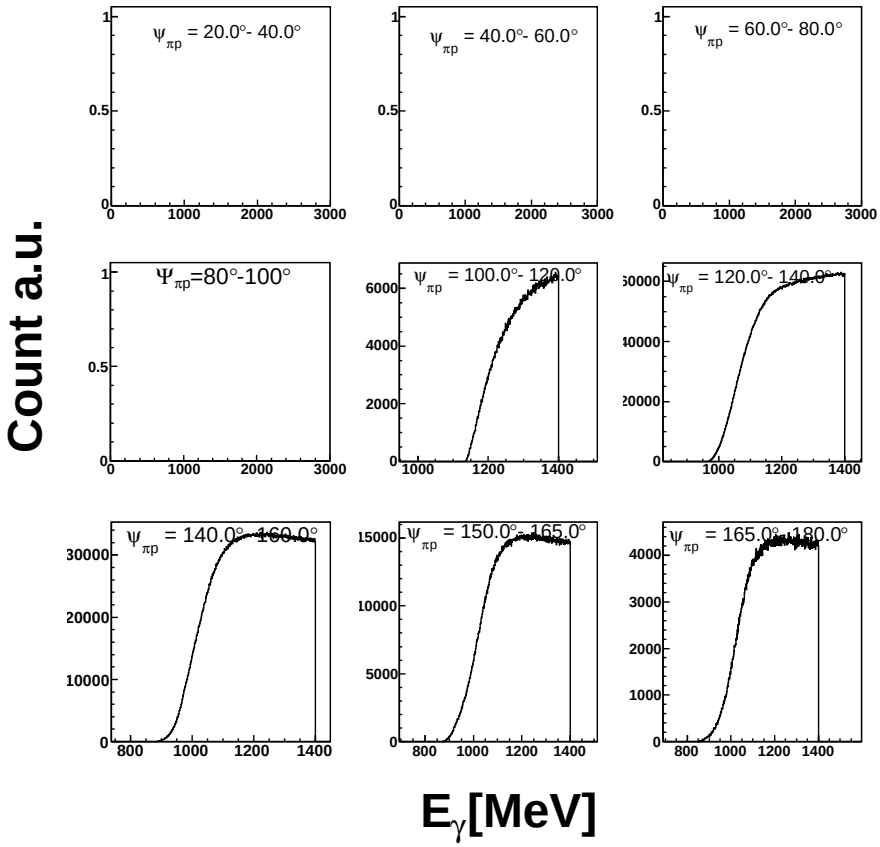

Figure C.2: *Count rate of π^0-p production in the γ-^{3}He center of mass for different opening angle ranges considering the F_{15} resonance.*

Appendix D

χ^2-test

The χ^2-test is based on the test of the $\gamma\gamma$ pair's mass (equation D.2). For each combination, the χ^2 was calculated. The best combination corresponds to the lowest χ^2.

$$\chi^2 = \sum i = 1 n_{\gamma\gamma}(\frac{m^{th}_{\gamma\gamma} - m^{exp}_{\gamma\gamma}}{\Delta m^{exp}_{\gamma\gamma,i}}) \tag{D.1}$$

where: $m^{th}_{\gamma\gamma}$ corresponds to the π^0-meson mass, $m^{exp}_{\gamma\gamma} = \sqrt{2E_1E_2 \cdot (1 - \cos\psi_{12})}$. Once the best combination is selected, the $\gamma\gamma$ pair mass is constrained to its theoretical value.
Example: $\eta \rightarrow \pi^0\pi^0\pi^0$, the equation D.2 becomes:

$$\chi^2 = (\frac{m^{th}_{\pi^0} - m^{exp}_{\pi^0,1}}{\Delta m^{exp}_{\pi^0,1}})^2 + (\frac{m^{th}_{\pi^0} - m^{exp}_{\pi^0,2}}{\Delta m^{exp}_{\pi^0,2}})^2 + (\frac{m^{th}_{\pi^0} - m^{exp}_{\pi^0,3}}{\Delta m^{exp}_{\pi^0,3}})^2 \tag{D.2}$$

Appendix E

Tables

This appendix summarizes the values of the cross sections obtained in chapter 9 and the tagger calibration file. For all the histograms presented in the work, ascii files with the values of the points are (will be) available at http://jazz.physik.unibas.ch/ pheron/XXX. .

E.1 Inclusive cross section for ^{3}He (γ,η)X

The table lists the inclusive cross section for the reaction ^{3}He ($\gamma.\eta$)X. The errors quoted are statistical only.

E_γ $[MeV]$	$\sigma[\mu b]$ Number
899.29	27.5047±0.147179
895.395	27.3399±0.145918
891.442	27.4217±0.141048
887.482	28.2434±0.139843
883.515	27.9898±0.126886
879.542	28.2032±0.164038
875.561	28.8958±0.145537
871.575	28.6539±0.141865
867.582	29.5202±0.167388
863.582	29.7293±0.167901
859.576	30.0342±0.147399
855.511	30.4482±0.149808
851.546	30.6853±0.15025
847.522	30.5116±0.149423
843.491	30.3923±0.147962
839.455	30.8572±0.173684
835.413	31.9354±0.171251
831.365	31.1848±0.144957
827.311	31.191±0.14379
823.252	31.6853±0.148653
819.187	31.3526±0.147089
815.116	31.1294±0.144049
810.993	31.5422±0.143514
806.96	30.5605±0.146767
802.873	30.6563±0.134119
798.782	30.2111±0.141885
794.685	30.4631±0.138782
790.583	30.2329±0.138476
786.476	30.2811±0.135711
782.364	29.0226±0.132045
778.247	91865.3±613.237
774.126	27.892±0.130845
770	27.4614±0.128481
765.812	26.9028±0.129747
761.735	26.026±0.127368
757.595	24.8612±0.121877
753.451	24.2845±0.1215
749.302	23.1336±0.11752

E_γ $[MeV]$	$\sigma[\mu b]$ Number
745.15	21.7851±0.113799
740.993	20.9651±0.116093
736.832	19.4824±0.113475
732.667	18.3639±0.128036
728.498	17.2609±0.10393
724.325	15.7861±0.104531
720.149	15.2557±0.0953389
715.917	7.73749±0.0775631
711.785	9.67852±0.0804482
707.597	11.777±0.0795652
703.406	10.6061±0.0750596
699.211	9.48281±0.0708632
695.017	7.43179±0.0628371
690.817	7.63777±0.0652056
686.613	7.06526±0.0594931
682.407	6.34571±0.0602416
678.197	5.68012±0.055698
673.986	5.01511±0.0514142
669.771	4.40024±0.0509088
665.492	3.96998±0.046857
661.335	3.37124±0.0441726
657.113	2.94933±0.0457987
652.89	2.56006±0.0378324
648.664	2.18099±0.0344241
644.436	1.73339±0.0353094
640.205	1.34711±0.0308324
635.973	1.29089±0.0283069
631.738	1.00055±0.025444
627.502	0.702119±0.0226696
623.263	0.49185±0.0197848
619.023	0.361856±0.0196191
614.717	0.313733±0.0192953
610.54	0.206588±0.0167713
606.295	0.121244±0.0155485
602.048	0.10415±0.0152933
597.801	−0.0589699±0.0126952
593.552	−0.0477211±0.0127532
585.05	−0.0474269±0.0131652

Table E.1: Inclusive cross section for $\eta \to 2\gamma$

E_γ $[MeV]$	$\sigma[\mu b]$ Number
899.29	25.3536±0.298284
895.395	25.8362±0.29892
891.442	25.7917±0.300237
887.482	26.2098±0.300554
883.515	26.5615±0.291656
879.542	27.7262±0.290805
875.561	27.7859±0.264993
871.575	27.2826±0.337796
867.582	27.6045±0.297534
863.582	27.9873±0.292909
859.576	28.781±0.344989
855.511	29.6168±0.349444
851.546	29.3194±0.30339
847.522	29.6828±0.307861
843.491	29.5838±0.306785
839.455	29.9608±0.307611
835.413	30.0764±0.305511
831.365	30.25±0.356674
827.311	30.4659±0.346724
823.252	30.1265±0.295065
819.187	29.9376±0.291529
815.116	30.316±0.300738
810.993	30.479±0.299733
806.96	29.734±0.290776
802.873	29.5171±0.286605
798.782	29.7214±0.298574
794.685	29.738±0.272367
790.583	29.3334±0.288113
786.476	28.792±0.277945
782.364	29.473±0.28154
778.247	29.0041±0.273414
774.126	27.7463±0.265621
770	84845.9±1221.33
765.812	26.4571±0.261987
761.735	25.6691±0.255306
757.595	25.151±0.257775
753.451	24.5145±0.253915
749.302	23.4292±0.242933
745.15	22.4971±0.240078

E_γ $[MeV]$	$\sigma[\mu b]$ Number
740.993	21.5113±0.232565
736.832	20.5365±0.226647
732.667	19.7818±0.231276
728.498	18.2005±0.224812
724.325	17.3746±0.255173
720.149	16.3236±0.206997
715.917	14.984±0.208415
711.785	13.7445±0.185189
707.597	7.16227±0.150753
703.406	9.2914±0.160179
699.211	10.6947±0.154772
695.017	9.79169±0.147018
690.817	8.45322±0.136166
686.613	6.53976±0.119331
682.407	6.6546±0.123407
678.197	6.37731±0.114447
673.986	5.58796±0.114193
669.771	4.69331±0.101992
665.492	4.29632±0.095508
661.335	3.71613±0.0934782
657.113	3.07183±0.0820599
652.89	2.6894±0.0779585
648.664	2.45868±0.0820563
644.436	1.9484±0.064242
640.205	1.83476±0.0607659
635.973	1.63318±0.064666
631.738	1.15846±0.0525636
627.502	0.928946±0.044021
623.263	0.715263±0.0381596
619.023	0.589548±0.0347435
614.717	0.432083±0.0288482
610.54	0.28275±0.0251189
606.295	0.332613±0.0276066
602.048	0.0681596±0.0123847
597.801	0.0767418±0.0129939
593.552	0.0714874±0.0126034
589.302	0.0366766±0.00944655
585.05	0.0940139±0.0139976
580.797	0.0704317±0.0123441

Table E.2: Inclusive cross section for $\eta \to 6\gamma$

Channel Number	E_γ $[MeV]$	ΔE_γ $[MeV]$
1	1401.354	1.925
2	1399.426	2.006
3	1397.418	2.086
4	1395.329	2.168
5	1393.159	2.251
6	1390.905	2.339
7	1388.561	2.428
8	1386.129	2.516
9	1383.612	2.602
10	1381.012	2.685
11	1378.332	2.764
12	1375.576	2.840
13	1372.747	2.910
14	1369.853	2.975
15	1366.898	3.033
16	1363.890	3.085
17	1360.835	3.128
18	1357.743	3.164
19	1354.621	3.189
20	1351.481	3.204
21	1348.329	3.205
22	1345.179	3.197
23	1342.041	3.178
24	1338.924	3.150
25	1335.840	3.114
26	1332.796	3.071
27	1329.798	3.021
28	1326.850	2.970
29	1323.954	2.919
30	1321.110	2.871
31	1318.314	2.828
32	1315.555	2.787
33	1312.853	2.796
34	1310.143	2.846
35	1307.441	2.884
36	1304.735	2.908
37	1302.011	2.920
38	1299.265	2.939
39	1296.467	2.892
40	1293.734	2.844
41	1290.953	2.869
42	1288.162	2.898
43	1285.360	2.924
44	1282.548	2.953
45	1279.725	2.980
46	1276.892	3.008
47	1274.047	3.035
48	1271.192	3.063
49	1268.288	3.016
50	1265.449	2.967
51	1262.560	2.995
52	1259.660	3.022
53	1256.750	3.049
54	1253.827	3.077
55	1250.894	3.106
56	1247.949	3.133

Table E.3: Tagger energy calibration: Tagger channel number, energy and corresponding energy error. All energies in MeV.

Channel Number	E_γ $[MeV]$	ΔE_γ $[MeV]$
57	1244.962	3.098
58	1242.026	3.061
59	1239.048	3.088
60	1236.057	3.116
61	1233.056	3.143
62	1230.043	3.171
63	1227.018	3.199
64	1223.982	3.228
65	1220.934	3.255
66	1217.875	3.284
67	1214.804	3.311
68	1211.683	3.262
69	1208.630	3.209
70	1205.525	3.236
71	1202.408	3.265
72	1199.280	3.292
73	1196.140	3.321
74	1192.989	3.349
75	1189.827	3.377
76	1186.653	3.405
77	1183.434	3.366
78	1180.272	3.324
79	1177.064	3.353
80	1173.845	3.380
81	1170.614	3.409
82	1167.372	3.437
83	1164.119	3.465
84	1160.855	3.494
85	1157.579	3.522
86	1154.256	3.479
87	1150.995	3.434
88	1147.686	3.462
89	1144.365	3.490
90	1141.035	3.519
91	1137.693	3.546
92	1134.340	3.575
93	1130.976	3.604
94	1127.601	3.632
95	1124.183	3.596
96	1120.819	3.559
97	1117.412	3.586
98	1113.994	3.614
99	1110.566	3.643

Channel Number	E_γ $[MeV]$	ΔE_γ $[MeV]$
102	1100.216	3.728
103	1096.746	3.757
104	1093.224	3.706
105	1089.773	3.654
106	1086.271	3.682
107	1082.760	3.710
108	1079.237	3.738
109	1075.704	3.766
110	1072.162	3.794
111	1068.609	3.823
112	1065.046	3.851
113	1061.473	3.880
114	1057.855	3.837
115	1054.299	3.792
116	1050.698	3.820
117	1047.086	3.849
118	1043.464	3.876
119	1039.833	3.905
120	1036.192	3.933
121	1032.542	3.962
122	1028.883	3.991
123	1025.215	4.019
124	1021.493	3.960
125	1017.850	3.898
126	1014.153	3.925
127	1010.447	3.955
128	1006.733	3.982
129	1003.010	4.010
130	999.278	4.038
131	995.536	4.067
132	991.787	4.095
133	988.027	4.123
134	984.214	4.059
135	980.485	3.994
136	976.701	4.021
137	972.908	4.049
138	969.107	4.076
139	965.298	4.105
140	961.481	4.132
141	957.654	4.160
142	953.821	4.188
143	949.979	4.216
144	946.129	4.245

Channel Number	E_γ $[MeV]$	ΔE_γ $[MeV]$
147	934.534	4.132
148	930.653	4.159
149	926.765	4.187
150	922.869	4.214
151	918.965	4.242
152	915.055	4.270
153	911.138	4.297
154	907.213	4.325
155	903.281	4.353
156	899.290	4.278
157	895.395	4.202
158	891.442	4.231
159	887.482	4.256
160	883.515	4.284
161	879.542	4.311
162	875.561	4.339
163	871.575	4.365
164	867.582	4.392
165	863.582	4.419
166	859.576	4.447
167	855.511	4.369
168	851.546	4.286
169	847.522	4.313
170	843.491	4.341
171	839.455	4.366
172	835.413	4.393
173	831.365	4.420
174	827.311	4.445
175	823.252	4.474
176	819.187	4.500
177	815.116	4.526
178	810.993	4.459
179	806.960	4.388
180	802.873	4.415
181	798.782	4.441
182	794.685	4.467
183	790.583	4.493
184	786.476	4.519
185	782.364	4.546
186	778.247	4.571
187	774.126	4.598
188	770.000	4.624
189	765.812	4.535

Channel Number	E_γ $[MeV]$	ΔE_γ $[MeV]$
192	753.451	4.496
193	749.302	4.520
194	745.150	4.547
195	740.993	4.572
196	736.832	4.597
197	732.667	4.623
198	728.498	4.648
199	724.325	4.675
200	720.149	4.700
201	715.917	4.622
202	711.785	4.543
203	707.597	4.567
204	703.406	4.592
205	699.211	4.618
206	695.017	4.644
207	690.817	4.668
208	686.613	4.694
209	682.407	4.718
210	678.197	4.742
211	673.986	4.768
212	669.771	4.793
213	665.492	4.693
214	661.335	4.591
215	657.113	4.615
216	652.890	4.639
217	648.664	4.665
218	644.436	4.688
219	640.205	4.711
220	635.973	4.736
221	631.738	4.761
222	627.502	4.785
223	623.263	4.810
224	619.023	4.834
225	614.717	4.729
226	610.540	4.621
227	606.295	4.644
228	602.048	4.668
229	597.801	4.691
230	593.552	4.715
231	589.302	4.738
232	585.050	4.761
233	580.797	4.785
234	576.543	4.809

Channel Number	E_γ $[MeV]$	ΔE_γ $[MeV]$
237	563.718	4.764
238	559.518	4.670
239	555.259	4.693
240	551.000	4.716
241	546.740	4.739
242	542.480	4.761
243	538.219	4.784
244	533.957	4.807
245	529.695	4.830
246	525.433	4.852
247	521.170	4.874
248	516.907	4.898
249	512.584	4.801
250	508.381	4.704
251	504.117	4.726
252	499.854	4.747
253	495.590	4.770
254	491.327	4.791
255	487.063	4.814
256	482.801	4.835
257	478.538	4.858
258	474.275	4.879
259	470.014	4.901
260	465.752	4.922
261	461.429	4.822
262	457.230	4.720
263	452.970	4.741
264	448.711	4.762
265	444.452	4.783
266	440.193	4.806
267	435.936	4.825
268	431.679	4.846
269	427.423	4.868
270	423.169	4.888
271	418.916	4.911
272	414.663	4.930
273	410.358	4.846
274	406.160	4.763
275	401.912	4.783
276	397.664	4.802
277	393.417	4.823
278	389.172	4.844
279	384.928	4.865

Channel Number	E_γ $[MeV]$	ΔE_γ $[MeV]$
282	372.205	4.924
283	367.967	4.945
284	363.730	4.965
285	359.430	4.856
286	355.262	4.746
287	351.030	4.766
288	346.801	4.785
289	342.574	4.805
290	338.348	4.824
291	334.124	4.844
292	329.901	4.863
293	325.681	4.883
294	321.463	4.901
295	317.246	4.922
296	313.033	4.940
297	308.767	4.849
298	304.612	4.757
299	300.404	4.777
300	296.199	4.795
301	291.996	4.814
302	287.796	4.833
303	283.598	4.852
304	279.403	4.870
305	275.209	4.887
306	271.018	4.908
307	266.830	4.924
308	262.644	4.945
309	258.405	4.849
310	254.280	4.755
311	250.103	4.773
312	245.928	4.791
313	241.756	4.810
314	237.587	4.827
315	233.420	4.844
316	229.255	4.863
317	225.095	4.880
318	220.937	4.897
319	216.782	4.916
320	212.629	4.932
321	208.480	4.950
322	204.276	4.853
323	200.191	4.755
324	196.051	4.772

Channel Number	E_γ $[MeV]$	ΔE_γ $[MeV]$	Channel Number	E_γ $[MeV]$	ΔE_γ $[MeV]$
327	183.650	4.824	340	130.255	4.805
328	179.523	4.841	341	126.172	4.821
329	175.398	4.857	342	122.092	4.836
330	171.278	4.875	343	118.016	4.852
331	167.160	4.891	344	113.944	4.869
332	163.046	4.908	345	109.875	4.885
333	158.935	4.924	346	105.810	4.901
334	154.827	4.942	347	101.749	4.916
335	150.664	4.839	348	97.631	4.812
336	146.622	4.740	349	93.637	4.708
337	142.525	4.756	350	89.586	4.724
338	138.432	4.772	351	85.540	4.740
339	134.341	4.787	352	81.497	4.753

Table E.7: Tagger energy calibration continued from table E.6: Tagger channel number, energy and corresponding energy error. All energies in MeV.

Bibliography

[1] *Proceedings of the Excited Baryons Conference*. RPA, August 1988.

[2] V.V. Anisovich. Wave function. *Nucl. Phys.*, A544(747), 1992.

[3] J.R.M Annand. Data analysis within an acquroot framework. *Universiy of Glasgow*, 2005.

[4] V. A. Baskov, J. P. Bocquet, V. Kouznetsov, A. Lleres, A. I. L'vov, L. N. Pavlyuchenko, V. V. Polyanski, D. Rebrevend, and G. A. Sokol. Possibility to study eta-mesic nuclei and photoproduction of slow eta-mesons at the graal facility. 2003.

[5] B.Boillat. *The Magnetic Dipole Moment of the ÎŤ+(1232) Resonance*. PhD thesis, Basel Physik institut, 2008.

[6] R. S. Bhalerao and L. C. Liu. Off-shell model for threshold pionic η production on a nucleon and for ηn scattering. *Phys. Rev. Lett.*, 54(9):865–868, Mar 1985.

[7] G. F. Chew, M. L. Goldberger, F. E. Low, and Y. Nambu. Relativistic dispersion relation approach to photomeson production. *Phys. Rev.*, 106(6):1345–1355, Jun 1957.

[8] R. E. Chrien, S. Bart, P. Pile, R. Sutter, N. Tsoupas, H. O. Funsten, J. M. Finn, C. Lyndon, V. Punjabi, C. F. Perdrisat, B. J. Lieb, T. Kishimoto, L. C. Liu, R. Estep, B. Dropesky, C. E. Stronach, and R. L. Stearns. Search for bound states of the η meson in light nuclei. *Phys. Rev. Lett.*, 60(25):2595–2598, Jun 1988.

[9] C.Lattes et al. Processes involving charged mesons. *nature*, 1947.

[10] R. Codling. PhD thesis, University of Glasgow, 2008.

[11] Manuel Dieterle. Photoproduction of π^0-mesons off quasi-free protons and neutronsmanui. Master's thesis, Universitat Basel, 2010.

[12] E.Downie. *The Magnetic Dipole Moment of the Δ (1232) Resonance.* PhD thesis, Glasgow physic institut, 2008.

[13] A. Fix and H. Arenhövel. problem with separable interactions$\eta - 3n$. *Phys. Rev. C*, 66(2):024002, Aug 2002.

[14] Stefan Friedrich. Teilchenidentifikation mittels cËĞ erenkov- und szintillationsdetektoren. Master's thesis, Universitat Giessen, 2008.

[15] A. Gabler. Response of taps to monochromatic photons with enrgies between 45 and 790 mev. *NIM*, A346, 1994.

[16] V. Hejny. *Photoproduktion von η-Mesonen an Helium 4.* PhD thesis, Universitat Giessen, 1998.

[17] M. Horras. The walkcorrection in a nuclear physical experiment. Master's thesis, Universitat Basel, 2006.

[18] Igal jaegle jaegle jaegle jaegle. *production of the deuteron or the search for missing resonances$\pi_0\pi_0, \eta and \eta'$.* PhD thesis.

[19] J.D. Johnson et al. Search for an η in pion double charge exchange on ^{18}o. *Physical Review*, June 1993.

[20] George R. Kalbfleisch, Luis W. Alvarez, Angela Barbaro-Galtieri, Orin I. Dahl, Philippe Eberhard, William E. Humphrey, James S. Lindsey, Deane W. Merrill, Joseph J. Murray, Alan Rittenberg, Ronald R. Ross, Janice B. Shafer, Frank T. Shively, Daniel M. Siegel, Gerald A. Smith, and Robert D. Tripp. Observation of a nonstrange meson of mass 959 mev. *Phys. Rev. Lett.*, 12(18):527–530, May 1964.

[21] S. S. Kamalov, L. Tiator, and C. Bennhold. Pion interaction with the trinucleon up to the eta production threshold. *Phys. Rev. C*, 47(3):941–956, Mar 1993.

[22] D. Krambrich. *Aufbau des Crystal Ball-Detektorsystems und Untersuchung des Helizitatasymmetrie in $\gamma p \to n\pi^+\pi^0$.* PhD thesis, Universitat Mainz, 2007.

[23] M. Lacombe. Paris approximation'. *Phys. Lett.*, B101(139), 1981.

[24] Lakeshore. ruthrerium oxide tech spec. Technical report, LakeShore, http://www.lakeshore.com/temp/sen/rrtdts.html, 2007.

[25] L. C. Liu and Q. Haider. Signature for the existence of eta-mesic nucleus. *Phys. Rev. C*, 34(5):1845–1854, Nov 1986.

[26] Yasser Maghrbi. *Photoproduction of mesons off Li7.* PhD thesis, Institut Fur Physik, Basel, 2010.

[27] B. Mayer, A. Boudard, B. Fabbro, M. Garçon, C. Kerboul, J. Poitou, F. Wellers, W. W. Jacobs, J. Saudinos, E. Tomasi-Gustafsson, J. P. Mouly, R. S. Kessler, B. M. K. Nefkens, B. Tippens, A. van der Schaaf, R. Abegg, W. T. H. van Oers, W. Briscoe, A. Petrov, and A. Moalem. Reactions pd$\rightarrow$ ^{3}he η and pd$\rightarrow$ ^{3}he $\pi^+\pi^-$ near the η threshold. *Phys. Rev. C*, 53(5):2068–2074, May 1996.

[28] T. Mersmann et al. Precision study of the eta-3He system using the d+p->3He+eta reaction. *Phys. Rev. Lett.*, 98:242301, 2007.

[29] A. Pevsner et al. EVIDENCE FOR A THREE PION RESONANCE NEAR 550-MEV. *Phys. Rev. Lett.*, 7:421–423, 1961.

[30] M. Pfeiffer, J. Ahrens, J. R. M. Annand, R. Beck, G. Caselotti, S. Cherepnya, K. Föhl, L. S. Fog, D. Hornidge, S. Janssen, V. Kashevarov, R. Kondratiev, M. Kotulla, B. Krusche, J. C. McGeorge, I. J. D. MacGregor, K. Mengel, J. G. Messchendorp, V. Metag, R. Novotny, M. Rost, S. Sack, R. Sanderson, S. Schadmand, A. Thomas, and D. P. Watts. Photoproduction of η-mesic *he*3. *Phys. Rev. Lett.*, 92(25):252001, Jun 2004.

[31] Particle physics Booklet. *Particle Data Group.* http://pdg.lbl.gov, 2009.

[32] S. A. Rakityansky, S. A. Sofianos, W. Sandhas, and V. B. Belyaev. Threshold scattering of the eta meson off light nuclei. *Phys. Lett.*, B359:33–38, 1995.

[33] Shoichi Sakata. Connection between the meson decay and the beta-decay. *Phys. Rev.*, 58(6):576, Sep 1940.

[34] Sven Schuman. *Magnetic moments of excited baryons.* PhD thesis, Mainz Physik Institut, 2008.

[35] Sven Schuman et al. Radiative pi0 photoproduction on protons in the delta+(1232) region. *EPJA*, 2010.

[36] N. V. Shevchenko, V. B. Belyaev, S. A. Rakityansky, S. A. Sofianos, and W. Sandhas. Coherent photoproduction of eta mesons on three-nucleon systems. *Nucl. Phys.*, A714:277–290, 2003.

[37] A. Sibirtsev, J. Haidenbauer, J. A. Niskanen, and Ulf-G. Meissner. Bounds on the bound η- h3 system. *Phys. Rev. C*, 70(4):047001, Oct 2004.

[38] Ingo Sick. *Private communication.* PhD thesis.

[39] L. R. Suelzle, M. R. Yearian, and Hall Crannell. Elastic electron scattering from $li6$ and $li7$. *Phys. Rev.*, 162(4):992, Oct 1967.

[40] Andreas Thomas, Francis Pheron, and Rudolph Kondratiev. Private communication. Technical report, Universitat Mainz, 2008.

[41] Tamotsu Ueda. I=0, jp=1− quasibound state in the ηnn-πnn coupled system. *Phys. Rev. Lett.*, 66(3):297–300, Jan 1991.

[42] J. Weiss. xclusive measurement of quasi-free η-photoproduction from deuterium. *The European Physical Journal A - Hadrons and Nuclei*, 2003.

[43] Colin Wilkin. Near-threshold production of η mesons. *Phys. Rev. C*, 47(3):R938–R940, Mar 1993.

[44] Colin Wilkin et al. Is there an eta-3He quasi–bound state ? *Phys. Lett.*, B654:92–96, 2007.

[45] Lilian Witthauer. -photoproduction off ηhe^3. Master's thesis, Universitat Basel, 2009.

Francis PHERON

Personal Details

Date of birth	**20th October 1980**	Address	**54 Rue de Huningue**
Place of birth	**Ivry-Sur-Seine, France**		**68300, Saint-Louis**
Nationality	**French**	Phone number	**(0033) 3 89 69 8129 (home)**
		E-mail	francis.pheron@unibas.ch

Formation/Professional experience

Since September 2005 — **PhD Student in particle physics (experimental),**
Physics Institute of Basel University, supervisor Prof Bernd Krusche:

- **Former assistant of nuclear physics** for a power plant engineer
- Analysis of data file created by an experimental set-up
- **Monte-Carlo simulation** coded for efficiency calculation
- Coding analysis software (C++) based on statistics and mathematical model
- Working on improving theoretical models included in PHD thesis

2007-2009 — **Master in project management,**
University of Haute-Alsace, Mulhouse

2004-2005 — **Master in theoretical physics,**
Ecole des Mines de Nantes (Grandes Ecoles)

- Training period in SuBaTech (Nantes): **Monte-Carlo simulation** for a Liquid Xenon TEP prototype

2000-2004 — **Licence in Applied Physics**,
University of the Antilles and Guyane (French West Indies)

1999-2000 — **Scientific Baccalauréat (Maths, Physics)** with distinction. Baccalauréat is the French equivalent to A level.

Skills

Management — Accounting, Human Resources, **Financial Mathematics**, Project Management, Interested in Penny Stock market and search for gain optimisation, Finance Analysis, Economy, **KONDOR+**

Mathematics — **Stochastic processes**, Probability theory, **Statistics**, Multivariate analysis, Monte-Carlo calculation, Numeric analysis, Particle Physics, **Grid computing**

Computer science — Computer Science, **Languages (C,C++, FORTRAN, Shell, Visual Basic)**, Worksheets (Excel + VBA), Database management system (Access, MySQL), Reporting tool (MS Project), LINUX, UNIX, Windows (all versions)

Languages

French Native, General **English** and English for a scientific purpose Fluent, **Spanish** Fair knowledge, **German** Fair knowledge, **Polish** Fair knowledge (Spoken)

Interests

Art: Urban music, Caribbean literature. **Sports:** Teams Sports